ADA062502

(18) (19) AMRL-TR-78-7

LEVEL II

(2)

(6)

REFINEMENT AND VALIDATION OF A THREE-DIMENSIONAL HEAD-SPINE MODEL.

DDC FILE COPY

(11) T. BELYTSCHKO
S. PRIVITZER
UNIVERSITY OF ILLINOIS AT CHICAGO CIRCLE
CHICAGO, ILLINOIS 60680

DDC
DEC 19 1978

AUG 78 (12) 163p.

(9) Final rept. 1 Jan 76 - 31 Dec 77,

Approved for public release; distribution unlimited.

(15) F33615-76-C-0570 (14) 7231 (7) 15

AEROSPACE MEDICAL RESEARCH LABORATORY
AEROSPACE MEDICAL DIVISION
AIR FORCE SYSTEMS COMMAND
WRIGHT-PATTERSON AIR FORCE BASE, OHIO 45433

78 12 11 002

NOTICES

When US Government drawings, specifications, or other data are used for any purpose other than a definitely related Government procurement operation, the Government thereby incurs no responsibility nor any obligation whatsoever, and the fact that the Government may have formulated, furnished, or in any way supplied the said drawings, specifications, or other data, is not to be regarded by implication or otherwise, as in any manner licensing the holder or any other person or corporation, or conveying any rights or permission to manufacture, use, or sell any patented invention that may in any way be related thereto.

Please do not request copies of this report from Aerospace Medical Research Laboratory. Additional copies may be purchased from:

National Technical Information Service
5285 Port Royal Road
Springfield, Virginia 22161

Federal Government agencies and their contractors registered with Defense Documentation Center should direct requests for copies of this report to:

Defense Documentation Center
Cameron Station
Alexandria, Virginia 22314

TECHNICAL REVIEW AND APPROVAL

AMRL-TR-78-7

This report has been reviewed by the Information Office (OI) and is releasable to the National Technical Information Service (NTIS). At NTIS, it will be available to the general public, including foreign nations.

This technical report has been reviewed and is approved for publication.

FOR THE COMMANDER

HENNING E. VON GIERKE
Director
Biodynamics and Bioengineering Division
Aerospace Medical Research Laboratory

AIR FORCE-56/80/3 October 1978 — 200

SECURITY CLASSIFICATION OF THIS PAGE (When Data Entered)

REPORT DOCUMENTATION PAGE

READ INSTRUCTIONS BEFORE COMPLETING FORM

1. REPORT NUMBER: AMRL-TR-78-7

2. GOVT ACCESSION NO.

3. RECIPIENT'S CATALOG NUMBER

4. TITLE (and Subtitle): REFINEMENT AND VALIDATION OF A THREE-DIMENSIONAL HEAD-SPINE MODEL

5. TYPE OF REPORT & PERIOD COVERED: Final Report 1/1/76 to 12/31/77

6. PERFORMING ORG. REPORT NUMBER

7. AUTHOR(s): T. Belytschko, R. Privitzer

8. CONTRACT OR GRANT NUMBER(s): F33615-76-C-0506

9. PERFORMING ORGANIZATION NAME AND ADDRESS: Department of Materials Engineering, University of Illinois at Chicago Circle, Chicago, IL 60680

10. PROGRAM ELEMENT, PROJECT, TASK AREA & WORK UNIT NUMBERS: 62202F, 7231-15-08

11. CONTROLLING OFFICE NAME AND ADDRESS: Aerospace Medical Research Laboratory, Aerospace Medical Division, Air Force Systems Command, Wright-Patterson Air Force Base, Ohio 45433

12. REPORT DATE: August 1978

13. NUMBER OF PAGES: 163

14. MONITORING AGENCY NAME & ADDRESS (if different from Controlling Office)

15. SECURITY CLASS. (of this report): Unclassified

15a. DECLASSIFICATION/DOWNGRADING SCHEDULE

16. DISTRIBUTION STATEMENT (of this Report): Approved for public release; distribution unlimited

17. DISTRIBUTION STATEMENT (of the abstract entered in Block 20, if different from Report)

18. SUPPLEMENTARY NOTES

19. KEY WORDS (Continue on reverse side if necessary and identify by block number)

Biomechanics
Spine
Head
Impact
Pilot ejection

20. ABSTRACT (Continue on reverse side if necessary and identify by block number)

A three dimensional, discrete model of human spine, torso and head has been refined and validated by comparison with available experimental results. The model consists of a system of rigid bodies, representing the head, vertebrae, and ribs, interconnected by deformable elements, which represent the intervertebral discs, ligaments, and other connective tissues. Four models of varying orders of complexity have been developed, ranging from a complex model with 252 degrees of freedom to a very simplified model with 32 degrees

DD FORM 1 JAN 73 1473 EDITION OF 1 NOV 65 IS OBSOLETE S/N 0102-014-6601

SECURITY CLASSIFICATION OF THIS PAGE (When Data Entered)

78 12 11 005

(cont'd)

G sub z

of freedom. The simplified model is able to closely reproduce many of the response characteristics of the more complex models in G_z loadings, and, because of its simplicity and short running time, may be well suited for design use.

Experimental results for human subjects suitable for validation of models are primarily available in the form of impedance curves for vertical harmonic excitation. So techniques were developed which efficiently obtain impedance curves for the model. Comparisons of the impedance curves of the models with experimentally developed curves show good agreement, both in the magnitudes and locations of peaks. Furthermore, by varying the components of the model it was shown that the primary peaks in the impedance curve in the 5 to 7 Hz range result from a combination of buttock-seat resonance, the flexural response of the spine and visceral resonance.

Analogous head-spine models were developed for the chimpanzee, baboon, and rhesus monkey. The objective of this development was to provide a scaling methodology for dynamic response and injury data among these non-human primates and man. Impedance curves are presented for these models and show significant differences in character from that of the human spine models.

Model studies are presented for ejection loading and for pre-ejection alignment by an inertial reel. The influence of various parameters, such as head position and the restraint system properties, have been studied. It has been found that although the effects of these parameters on axial forces is sustained by the spine are quite small, they have significant effects on the moments sustained by the spine.

For the purpose of facilitating the interpretation of the output of the model, an injury potential criterion has been developed. This injury criterion is based on the stresses in the cortical bone of the vertebral body that result from the combined effects of axial force and moment. By using a statistical distribution about the mean breaking strength, it has been possible to develop a postprocessing algorithm which predicts the likelihood of vertebral body failure at different levels of the spine.

PREFACE

The research in this final report was performed under Air Force Contract F33615-76-C-0506 awarded to the University of Illinois at Chicago Circle for the period January 1, 1976 to December 31, 1977. The Air Force program monitor was Mr. Ints Kaleps of the Mathematics and Analysis Branch, Biodynamics and Bioengineering Division of the Aerospace Medical Research Laboratory, Aerospace Medical Division of the Air Force Systems Command at Wright Patterson Air Force Base, Ohio.

Best Available Copy

TABLE OF CONTENTS

	Page
Chapter I Introduction	9
Chapter II Spine Models	13
1. Isolated Ligamentous Spine	14
2. Isolated Ligamentous Spine with Viscera	21
3. Ligamentous Spine with Ribs and Hydrodynamic Viscera	25
4. Simplified Spine Model	28
Chapter III Impedance	36
1. Rationale and Overview	36
2. Mathematical Preliminaries	37
3. Summary of Impedance Literature	41
4. Impedance Results	47
Chapter IV Injury Potential Model	59
1. Injury Potential Function for Cylindrical Vertebral Body Model	59
2. Compressive Strength of Vertebrae	63
3. Elastic Moduli of the Vertebral Cortex and the Trabecular Bone	65
4. Vertebral Geometric Properties	65
5. Failure Criteria for the Injury Potential Function	66
Chapter V Primate Head-Spine Model	70
1. Chimpanzee	79
2. Baboon	87
3. Rhesus Monkey	92

TABLE OF CONTENTS (Cont'd.)

	Page
Chapter VI Simulations of Pre-ejection Pilot Alignment	97
1. Motivation and Method	97
2. Computer Modeling of Belt and Shoulder	97
3. Pre-ejection Pilot Alignment Models	102
4. Pre-ejection Pilot Alignment Studies	105
5. Discussion of Pre-ejection Alignment Studies	126
Chapter VII Ejection Simulations	130
1. Introduction and Objectives	130
2. Isolated Ligamentous Spine Model	130
3. Ligamentous Spine with Ribs and Hydrodynamic Visceral Representation	140
4. Comparison of Ejection Response of SSM, ILSV and CSM	151
APPENDIX A: Impedance Prigram Option	155
References	157

LIST OF FIGURES

Figure		Page
2.1	Isolated ligamentous spine (ILS); frontal plane view	15
2.2	ILS; sagittal plane view	16
2.3	Lumbar region torso cross-section	22
2.4	Isolated ligamentous spine with viscera; sagittal plane view	26
2.5	Complex spine model (CSM); frontal plane view	29
2.6	CSM; sagittal plane view	30
2.7	Simplified spine model (SSM); sagittal plane view	33
3.1	Experimentally measured impedance curves	42
3.2	Influence of body posture on impedance	42
3.3	Abdominal wall displacement versus excitation frequency	44
3.4	Comparison of experimentally, analytically and numerically determined impedances	45
3.5	Comparison of SSM without buttocks with experimentally determined impedance	49
3.6	Impedances of SSM sybsystems	50
3.7	Comparison of SSM with buttocks with experimentally determined impedance	52
3.8	Comparison of ILSV without buttocks with experimentally determined impedance	54
3.9	Comparison of ILSV with buttocks with experimentally determined impedance	56
3.10	Comparison of SSM and ILSV impedances without buttocks	57
3.11	Comparison of SSM and ILSV impedances with buttocks	58
4.1	Idealization of a vertebral body as a cylindrical shell	60
5.1	Chimpanzee spine model	71
5.2	Geometric idealization of chimp anatomy	73
5.3	Chimpanzee torso geometry	75

LIST OF FIGURES (Cont'd.)

Figure		Page
5.4	Chimp ejection simulation force time histories	85
5.5	Impedance of chimp model with viscera	86
5.6	Baboon spine model	88
5.7	Impedance of baboon spine model	91
5.8	Rhesus monkey spine model	93
5.9	Impedance of rhesus monkey spine model	96
6.1	Typical inertia reel unit and harness configuration	98
6.2	Typical contact point configuration	99
6.3	Frontal plane view of shoulder rigid body model	103
6.4	PAM2; Pre-ejection pilot alignment model with T1 2" forward	106
6.5	PAM4; Pre-ejection pilot alignment model with T1 4" forward	107
6.6	PAM4-4; sagittal plane view	108
6.7	PAM4-4; Frontal plane view	109
6.8	PAM6; Pre-ejection pilot alignment model with T1 6" forward	110
6.9	Study 1: Response of PAM2	111
6.10	Study 2: Response of PAM4	112
6.11	Study 2: Sagittal plane response of PAM4-4	115
6.12	Study 2: Frontal plane response of PAM4-4	116
6.13	Study 3: Response of PAM2, reel 2.2 cm below standard height	117
6.14	Study 3: Response of PAM2, reel 7.2 cm below standard height	118
6.15	Study 4: Response of PAM2	120
6.16	Belt force time history for studies 5 and 6	121
6.17	Study 5: Response of PAM4	122
6.18	Initial pilot configuration for AMRL retraction test run No. 93	124
6.19	Study 6: Response of PAM6	125

LIST OF FIGURES (Cont'd.)

Figure		Page
6.20	Study 6: Injury Potential Function for PAM6	127
7.1	Response of ILS without secondary column and restraint system	133
7.2	Response of ILS with secondary column - without restraint system	134
7.3	0 - 80 msec ejection response of ILS with restraint system	137
7.4	120 - 320 msec ejection response of ILS with restraint system	138
7.5	CSM ejection response	142
7.6	CSM ejection response, reel at initial level of T4	145
7.7	CSM ejection response, head/helmet 4" forward	147
7.8	Axial force response; CSM head/helmet 4" forward	148
7.9	Moment response; CSM head/helmet 4" forward	149

LIST OF TABLES

Table		Page
2.1	Isolated ligamentous spine (ILS) geometric data	17
2.2	ILS stiffness data	18
2.3	ILS inertial data	19
2.4	Isolated ligamentous spine with viscera (ILSV) inertial data	23
2.5	ILSV viscera stiffnesses	27
2.6	Complex spine model (CSM) inertial data	31
2.7	CSM rib cage stiffness data	32
2.8	Simplified spine model (SSM) inertial data	34
2.9	SSM stiffness data	35
4.1	Breaking loads of vertebrae T8 through L5	64
4.2	Vertebral failure criteria	67
5.1	Weight ratios for idealized chimp anatomy	74
5.2	Chimp inertial data	77
5.3	Chimp disc geometric data	80
5.4	Chimp stiffness data	81
5.5	Natural frequencies of human and chimp spine models	83
5.6	Baboon inertial data	89
5.7	Baboon stiffness data	90
5.8	Rhesus monkey inertial data	94
5.9	Rhesus monkey stiffness data	95
6.1	Shoulder rigid body contact point coordinates and beam stiffnesses	104
6.2	Peak force response magnitudes for studies 1 to 4	114
6.3	Peak force response magnitudes for study 5	123

LIST OF TABLES (Cont'd.)

Table		Page
7.1	Peak force response for ejections of ILS without restraint system	132
7.2	Peak force response for ejection of ILS with secondary column and restraint system	136
7.3	Peak force response for ejection of CSM	147
7.4	Peak force response for CSM, reel at initial level of T4	144
7.5	Peak force response for CSM, head/helmet 4" forward	146
7.6	Peak force response comparison for SSM, ILSV and CSM	153
7.7	Peak visceral pressure response comparison for SSM, ILSV and CSM	154

CHAPTER I

INTRODUCTION

In the design of the cockpit, an important constraint is the feasibility of a safe ejection from the aircraft. Thus, in the consideration of new designs or design modifications, their effect on the safety of ejection must be evaluated. For example, the expected posture of the pilot, pre-ejection alignment, and the angle of ejection all influence the forces sustained by the spine. Therefore the designer requires information as to which combination of these parameters will minimize the possibility of injury. Moreover, it is useful to be able to study particularly detrimental combinations of parameters, so that the ejection system and cockpit environment can be designed to minimize injuries even under extreme circumstances.

Experimental work on ejection has consisted largely of laboratory tests conducted on human volunteers and animals. These tests are expensive, require considerable preparation, and provide only limited information as to the possibility of injury. Furthermore, such tests are not often possible within the time framework of the design process. Thus the design of ejection devices has always depended heavily on the use of analytical models. The most well known of these is the Dynamic Response Index Model (DRI), which is essentially a one degree of freedom lumped mass, spring model of the head-spine-torso. It has been extensively correlated with injury data and provides a useful criterion for evaluating the safety of a crewman exposed to axial acceleration.

For situations where specifications other than the axial response must be considered, simple models of the DRI type become less attractive, because each parameter, such as curvature of the spine, forward tilt, or asymmetric head mass, would have to be correlated with injury statistics. For these applications, general purpose simulation models with the capability of treating a wide variety of environ-

ments appear more promising.

Belytschko, et al., (1976, AMRL-TR-76-10) have developed three dimensional models of the head-neck-spine which treat the individual anatomical elements, such as vertebrae, intervertebral discs, ligaments and ribs. Because the geometry and physical properties are modeled, specific features of the pilot's anatomy and his equipment can be treated. Moreover, the models' behavior under forces in any direction and of any intensity can be studied, so that various environments can be evaluated.

As a consequence of its generality, two aspects of the model need attention: itscompleteness leads to considerable computational requirements, and it requires validation by comparison with experimental results.

In order to reduce the computational requirements, the model has been modularized so that various components can be simplified. Four models have evolved and are described in Chapter II. The first three are from AMRL-TR-76-10, although some data has been modified as the result of validation studies. The fourth model was developed completely in this study. It is a simplified version of the more general model of the spine, yet it duplicates most aspects of the more complex models under vertical excitation, and thus proves ideal for design use.

The raw output of these models are force, moment, displacement, velocity and acceleration time histories at the various anatomical elements. For the purpose of facilitating the interpretation of this output, an injury criterion has been developed, and is described in Chapter IV. This injury criterion is based on the stresses in the cortical bone of the vertebral body. By using a statistical distribution about the mean breaking strength, it has been possible to develop a post-processor package that gives the likelihood of failure at the levels of the spine for each simulation.

The validation of this model is being approached in two ways. First, the

impedance of the model to vertical excitation at the pelvis has been compared to the experimental measurements on human subjects. To obtain the model impedance, a Fast Fourier Transform technique has been developed which enables the impedance of any linearized model to be found from a single simulation. This procedure is described in Chapter III and comparisons of the model impedance with the experimental results are presented. By adjusting the damping of the models in AMRL-TR-76-10, it has been possible to duplicate experimental impedance curves very closely. Furthermore, it has been shown that the major peak in the impedance curve at approximately 5 Hz arises from a combination of three resonances: the seat-buttocks, the flexural response of the spine, and the visceral resonance.

The second approach which has been taken to validate the modeling procedure consists of studying similar models of non-human primates. Since experimental results, particularly in high acceleration environments, can more readily be obtained for animal subjects, this will enable the basic modeling procedures to be evaluated. In addition, the development of similar models for non-human primates will hopefully shed some light on the problems of scaling. These models are described in Chapter V. It is of interest to note that even these preliminary models indicate some of the sources of difficulties in scaling between primates; for example, the lowest frequency of the chimpanzee model is dominated more by the head-neck mode than that of the human body because of the larger relative mass of the chimpanzee head.

In the course of this work, the problem of ejection has continuously been studied with the currently available models. The purpose of these studies has been to obtain an understanding of what factors play an important role in the response of the model and an assessment of the validity of the model. In addition, concern has arisen about the influence of the behavior of the spine during pre-ejection alignment by the inertial reel. Several studies have been made of this

process with the model and are described in Chapter VI. These studies include the effects of head position, the restraint system, and harness positions. In Chapter VII, ejection simulations are reported. These include results from models of different levels of complexity, and it is shown that the simplified version of the spine model is quite representative of the response in an ejection environment.

CHAPTER II

SPINE MODELS

In this Chapter the geometrical, stiffness and inertial data of the spine models are summarized. Four models will be presented:

1. the isolated, ligamentous spine and head (ILS);
2. a two load-path model consisting of the isolated ligamentous spine, the viscera, and head (ILSV);
3. a complex spine model, which includes the spine, rib cage, viscera and head (CSM);
4. a simplified spine model which uses a minimal number of elements and masses to represent the spine, viscera, and head (SSM).

The first three models have previously been described by Belytschko, et al., (1976), but the viscera in these models have been modified extensively on the basis of impedance studies which are described later.

The fourth model, SSM, is a new model which is aimed at providing a simple design tool. This model has only 8 nodes, compared to 27 nodes for ILSV and 42 nodes for CSM, respectively. Running time for an 100 msec simulation on an IBM 370/158 is about 10 sec, which is of the order of 1/40 of the computer time for ILSV and about 1/100 of the computer time for CSM.

The geometries of the models are defined relative to a global coordinate system; its origin is 4 cm directly above the pelvic mass center. The positive x axis is oriented sideways (to the left), the y axis is positive towards the back, and the z axis is positive vertically upward (towards the head). The x-z, y-z, and x-y planes correspond to the frontal plane, the sagittal plane, and the horizontal plane respectively. Many of the procedures used to determine the data were discussed in detail by Belytschko, et al., (1976); we will here confine ourselves to alterations of the data.

II.1 Isolated Ligamentous Spine

The isolated ligamentous spine model consists of the head, the cervical and thoracolumbar spines, and the pelvis. Figures 2.1 and 2.2 depict the frontal plane and sagittal plane views respectively. The crosses in Fig. 2.2 represent primary nodes, which coincide with the mass centers of the rigid bodies. They are generally located outside the vertebrae because they represent the mass centers of entire horizontal torso segments. The vertebrae are considered rigidly embedded in their respective torso segments. This representation was first conceived by Orne and Liu (1970).

The geometry of each vertebra is determined by the position of 13 points, or secondary nodes, representing the centers of the inferior and superior end plates; the spinous process tip; the left and right transverse process tips; the left and right/inferior - superior articular facet points; and the left and right/inferior - superior ligamenta flava points. Adjacent vertebrae are interconnected through the secondary nodes by deformable elements representing the connective tissues; ligaments and the intervertebral disc. Spring elements with resistance only in tension are used to represent the ligaments. Although data defining the articular facet planes has been developed, in the thoracolumbar spine the facet joints are represented by spring elements.

In the cervical spine, each articular facet plane is represented by three points and the joints are modeled with hydrodynamic elements. The intervertebral discs are modeled as short beams. These elements are described in detail by Belytschko, et al., (1976). Tables 2.1, 2.2 and 2.3 list the geometries, stiffness and inertial data for the isolated ligamentous spine. The inertial data is based on Liu and Wickstrom (1973), the stiffness data primarily on Schultz, et al., (1973), except that the lumbar disc axial stiffnesses are increased to account for

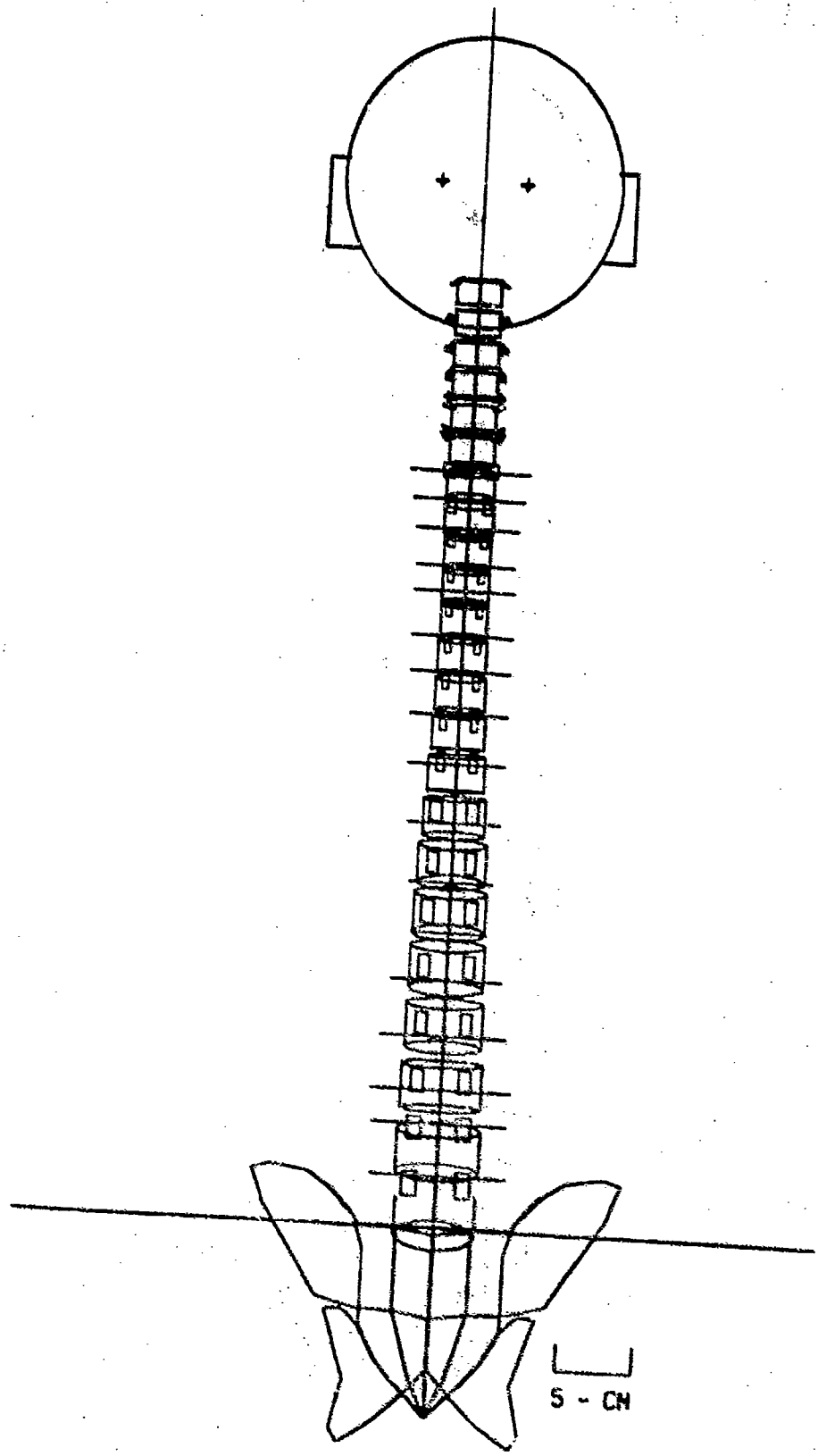

Figure 2.1. Isolated ligamentous spine model (ILS); frontal plane view.

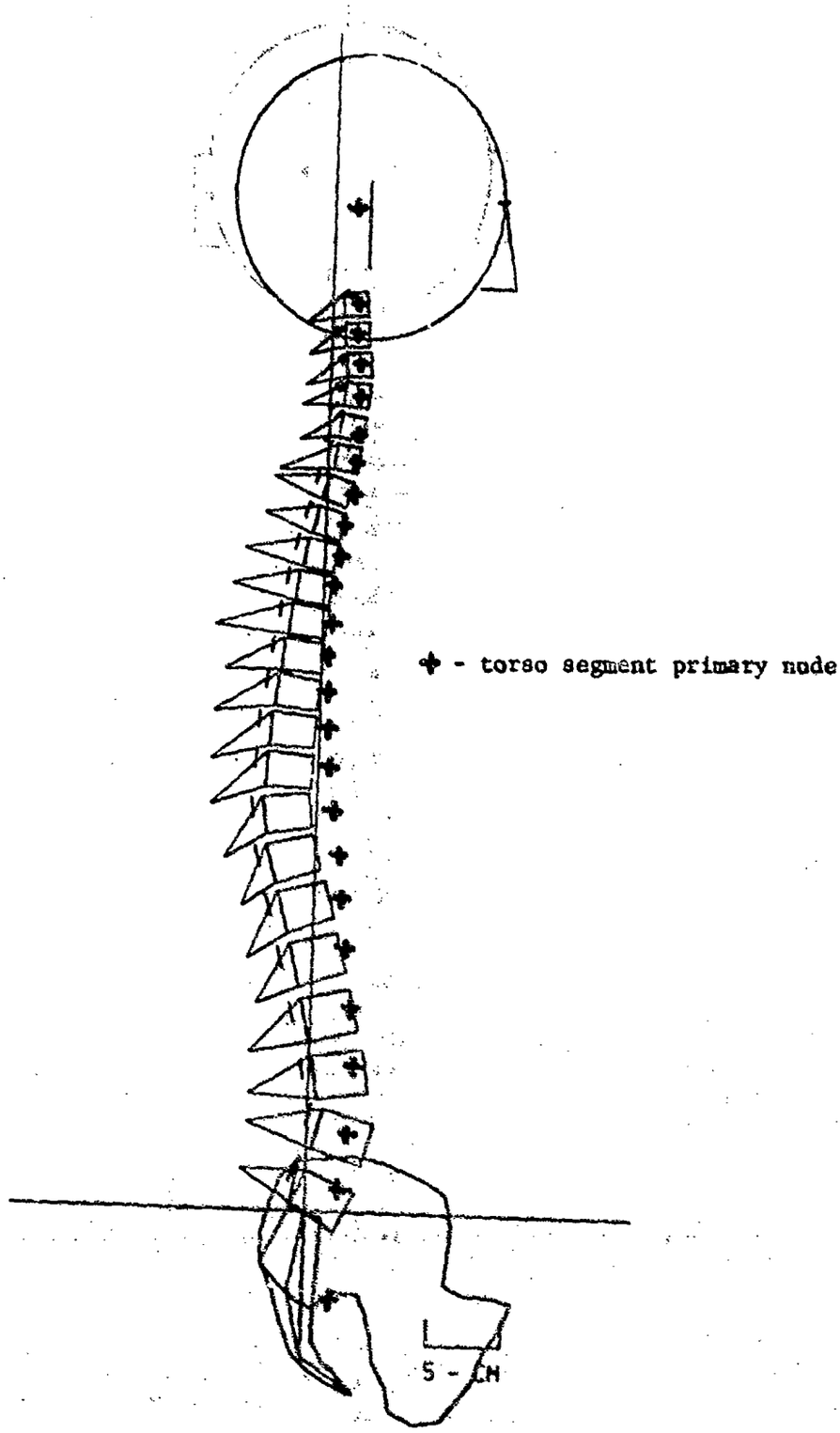

Figure 2.2. Isolated ligamentous spine model (ILS); sagittal plane view.

Table 2.1 Isolated ligamentous spine (ILS) geometric data as reported by Belytschko, et al., (1976).

Vertebral Level	Coordinates of Inferior End Plate Center		Vertebral Body Height	Intervertebral Disc Height*
	y (cm)	z (cm)	(cm)	(cm)
L5	1.800	2.020	2.392	1.859
L4	1.100	5.700	2.636	1.354
L3	1.000	9.550	2.751	1.223
L2	1.331	13.450	2.792	1.173
L1	2.142	17.150	2.726	0.996
T12	3.003	20.590	2.567	0.822
T11	3.882	23.680	2.433	0.645
T10	4.594	26.500	2.298	0.477
T9	4.849	29.240	2.146	0.460
T8	4.638	31.830	2.073	0.459
T7	4.580	34.300	2.019	0.404
T6	4.250	36.610	1.990	0.314
T5	3.990	38.850	1.957	0.266
T4	3.690	41.000	1.902	0.214
T3	3.350	43.150	1.850	0.274
T2	2.920	45.260	1.790	0.306
T1	2.410	47.440	1.648	0.448
C7	1.909	49.420	1.612	0.394
C6	1.760	51.448	1.516	0.434
C5	1.460	53.516	1.515	0.576
C4	1.290	55.439	1.513	0.417
C3	1.484	57.332	1.511	0.398
C2	1.636	59.239	1.500	0.408

* Indicates disc below vertebral level.

Table 2.2 Isolated ligamentous spine (ILS) Stiffness Data from Belytschko, et al., (1976).

Disc Level	Axial Stiffness Dyne/cm x 10^9	Torsional Stiffness Dyne-cm x 10^9	Bending Stiffness Dyne-cm x 10^9 Sagittal Plane	Bending Stiffness Dyne-cm x 10^9 Frontal Plane	Shear Deformation Parameter Φ
S-L5	1.47	0.90	0.70	1.57	7
L5-L4	1.87	1.10	0.80	1.81	9
L4-L3	2.00	1.20	0.90	2.19	9
L3-L2	2.00	1.20	0.90	2.16	13
L2-L1	2.13	1.20	0.90	2.20	14
L1-T12	1.80	1.00	0.90	2.27	16
T12-T11	1.50	0.80	1.00	2.34	30
T11-T10	1.50	0.70	1.20	2.44	41
T10-T9	1.50	0.70	1.10	1.93	72
T9-T8	1.50	0.60	1.10	1.76	78
T8-T7	1.50	0.60	1.00	1.59	66
T7-T6	1.80	0.60	1.00	1.62	82
T6-T5	1.90	0.60	1.00	1.68	177
T5-T4	2.10	0.60	1.00	1.81	158
T4-T3	1.50	0.40	0.60	1.22	126
T3-T2	1.20	0.30	0.40	1.04	48
T2-T1	0.70	0.20	0.20	0.63	34
T1-C7	1.10	0.18	0.20	0.62	45
C7-C6	2.84	0.11	0.11	0.25	45
C6-C5	1.01	0.07	0.06	0.10	45
C5-C4	0.60	0.04	0.04	0.06	45
C4-C3	0.67	0.05	0.04	0.05	45
C3-C2	0.70	0.05	0.04	0.05	45
C2-C1	0.60	0.04	0.04	0.10	45
Neck[1]	0.14	0.52	0.69	0.69	2

All ligament and facet axial stiffness 1.5 x 10^7 dyne/cm.

[1] Single neck element which can be substituted for the cervical spine.

Table 2.3. Isolated ligamentous spine (ILS) inertial data, from Belytschko, et al., (1976)

Vertebral Level	Mass m Grams x 10^3	$I_{\bar{x}\bar{x}}$ Gram-cm^2 x 10^4	$I_{\bar{y}\bar{y}}$ Gram-cm^2 x 10^5	$I_{\bar{z}\bar{z}}$ Gram-cm^2 x 10^5
Pelvis	16.200	128.000	20.000	19.300
L5	2.240	8.185	1.795	2.832
L4	2.187	8.083	1.704	2.291
L3	2.152	8.264	1.682	2.280
L2	2.012	8.354	1.695	2.291
L1	1.960	8.061	1.569	2.212
T12	1.676	7.022	1.309	1.919
T11	1.603	7.056	1.230	1.941
T10	1.352	6.028	1.129	1.648
T9	1.417	6.164	1.230	1.716
T8	1.326	5.543	1.208	1.670
T7	1.308	5.347	1.219	1.659
T6	1.193	4.425	1.162	1.546
T5	1.175	3.838	1.151	1.490
T4	1.064	3.138	1.060	1.354
T3	1.160	2.878	1.174	1.422
T2	1.074	2.077	1.029	1.230
T1	1.359	0.745	0.518	1.716
Head	5.612	44.786	4.044	3.385

the body-weight preload as described by Belytschko, et al., (1976).

In many studies reported herein the cervical region of the isolated ligamentous spine has been replaced by a single beam element, the stiffness of which is given in Table 2.2. The isolated ligamentous spine with the cervical region represented by a single beam element is the spine model which will be referred to as the ILS.

The ILS model allows for only one path of force transmission along the torso, namely the spine. Some investigators (e.g. Weiss and Mohr (1967)) have reported the observation of a longitudinal wave through the abdomen during experiments in which subjects seated in chairs were dropped onto yielding as well as non-yielding bases. Because the spine is several orders of magnitude stiffer than the viscera, it is the primary path of force transmission from the seat to the upper torso and head. However, the viscera transmits some of the force to the mid and upper torso through the diaphragm and ribs. It is these observations which led to the development of the two visceral models which will be discussed shortly.

Another shortcoming of ILS is the low flexural stiffness of the spine model. Lucas and Bressler (1961) determined frontal plane buckling loads of 2×10^6 to 10×10^6 dynes for an isolated ligamentous spine constrained against sagittal plane motion. The sagittal and frontal plane bending stiffnesses are of the same order, so the sagittal plane curvature would tend to lower the sagittal plane buckling loads. Since the spine model stiffnesses are based on the material constants of the intervertebral discs, it will also buckle under these loads. The ejection environment produces internal forces several orders of magnitude higher than the buckling loads. To increase the stability of the spine when subjected to these accelerations it is necessary to increase the bending stiffness of the model. This is accomplished by incorporating representations of the rib

cage and viscera into the spine model.

The effects of the viscera and the rib cage are approximated by a second column of beam elements interconnecting the primary nodes from the pelvis to T1. The properties of these beam elements were chosen so that they offer resistance only in cases of large relative rotation between the ends of an element by using a cubic moment-curvature relation. As will be seen subsequently, this secondary column improved the flexural response of the spine, but deformation in the lumbar region remained quite severe.

II.2 Isolated Ligamentous Spine with Viscera

The model of the isolated ligamentous spine with a visceral representation will be referred to as the ILSV model. In ILSV, vertebral levels T11-S1 are separated into visceral and spinal masses. The subdivision of the torso cross-sections is based on Eycleshymer and Schoemaker (1970). A typical section and the areas ascribed to the viscera and spine are shown in Fig. 2.3. The spinal and visceral translational and rotational masses at each vertebral level were computed from these areas using a uniform density of 1 gm/cm^3, and are given in Table 2.4. The total masses compare well with the data of Liu and Wickstrom (1973).

It was assumed that the only mode of force transmission through the viscera is axial. Hence it was only necessary to determine the axial elastic and viscous constants for each element interconnecting the visceral masses. An approximate fundamental frequency was computed for the viscera using the results of Coermann, et al., (1960), who observed a peak in abdominal wall displacements when the driving frequency was between 3 and 4 Hz. Assuming that displacements of the viscera are coupled to the abdominal wall displacements, with peaks occurring at the same frequencies, we can determine the fundamental frequency of the viscera. For a damping ratio less than 0.707, the frequency ratio which defines the maximum

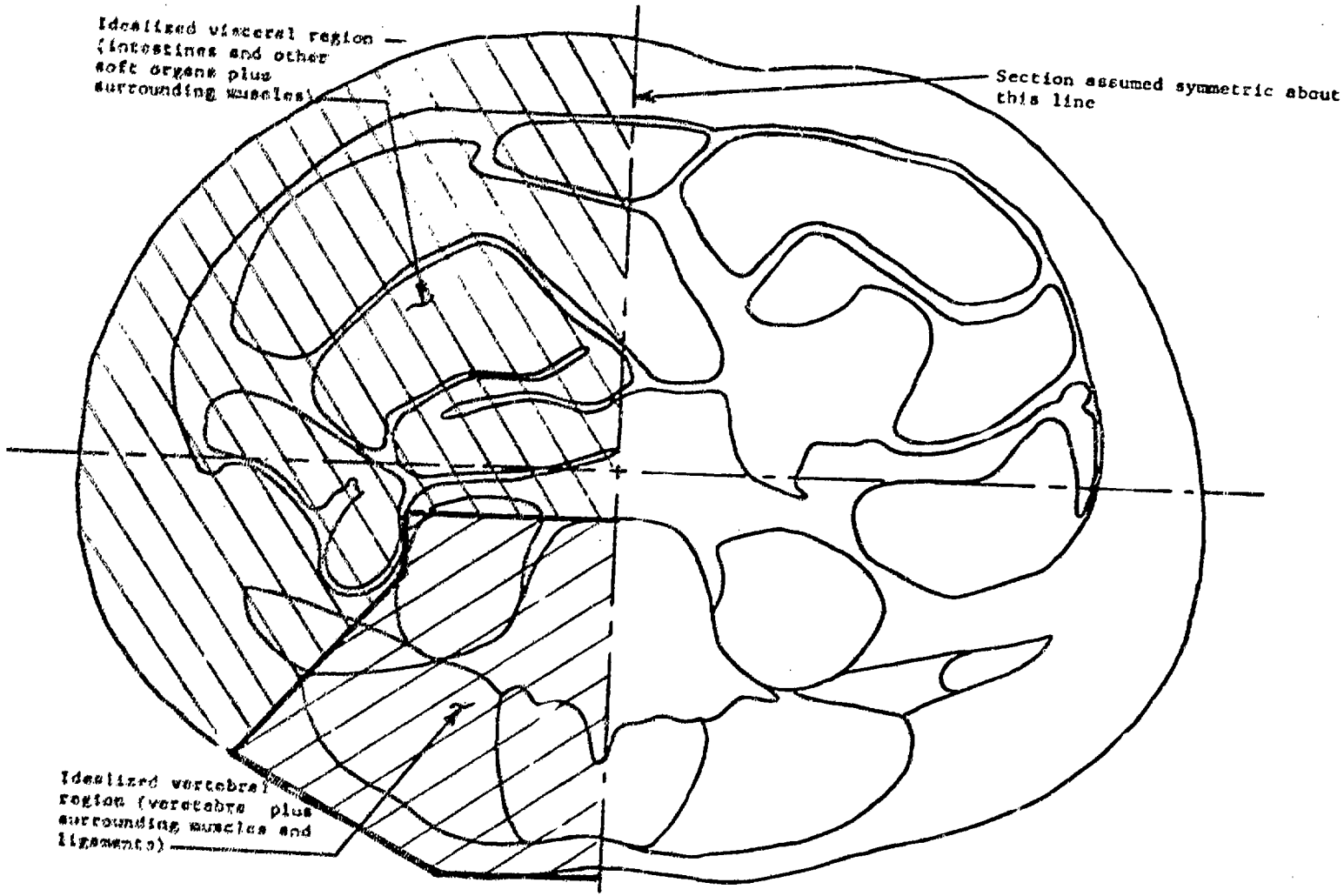

Figure 2.3. Typical lumbar region torso cross-section from Eycleshymer and Schoemaker and its subdivision into vertebral and visceral regions.

Table 2.4. Isolated Ligamentous spine with viscera (ILSV); inertial data for vertebral levels S1-T11.

Vertebral Level	Translational mass m grams x 10^2	Rotational inertia grams-cm^2 x 10^4 I_{xx}	I_{yy}	I_{zz}
Vertebral Inertial Data L5-T11				
L5	4.659	0.438	0.537	0.826
L4	5.621	0.417	0.962	1.228
L3	4.325	0.273	0.665	0.861
L2	3.420	0.183	0.673	0.795
L1	2.842	0.138	0.502	0.593
T12	3.329	0.135	0.319	0.349
T11	3.184	0.122	0.292	0.334
Visceral Inertial Data S1-T11				
S1	17.080	1.000	1.000	1.000
L5	17.740	5.897	17.410	21.140
L4	16.250	4.851	16.080	18.870
L3	17.200	4.417	16.160	18.370
L2	16.700	5.367	16.280	19.310
L1	16.760	5.556	15.190	19.160
T12	13.410	4.758	12.770	16.710
T11	12.820	4.898	12.010	17.040

point of the displacement versus excitation frequency curve is

$$r = \frac{\omega/2\pi}{\beta/2\pi} = \sqrt{1-2\varphi^2} \tag{2.1}$$

where

$\beta/2\pi$ = fundamental natural frequency (Hz)

$\omega/2\pi$ = excitation frequency (Hz)

φ = visceral damping ratio.

From the results of Weiss and Mohr (1967), an approximate value of 0.5 was determined for the visceral damping ratio. Using a value of 3.5 Hz for $\omega/2\pi$, Eq. (2.1) results in $\beta/2\pi$ approximately equal to 5 Hz.

If we treat the viscera - torso wall system as a one-dimensional rod and assume that the viscera are essentially fixed at the pelvis and the diaphragm, the fundamental natural frequency is given by

$$\beta/2\pi = \frac{c}{2L} \tag{2.2}$$

where L = length of visceral "stack"

c = longitudinal wave speed through viscera.

The longitudinal wave speed is given by

$$c = \sqrt{\frac{B}{\rho}} \tag{2.3}$$

where B = effective bulk modulus of viscera - torso wall system

ρ = visceral density = 1 gm/cm^3.

Combining Eqs. (2.2) and (2.3) we have

$$B = (L\beta/\pi)^2 \tag{2.4}$$

With L equal to 31.64 cm (the distance from the pelvis to T10) and $\beta = 10\pi$, Eq. (2.4) yields a value of 1×10^5 dynes/cm^2 for the effective bulk modulus of the viscera - abdominal wall system.

Once we have determined B, the stiffness of a visceral element is given by

$$k = \frac{AB}{L} \tag{2.5}$$

where A is the average cross-sectional area of the element.

The ILSV model is shown in Fig. 2.4. At vertebral level L5 to T11, the visceral and vertebral mass are interconnected by horizontal spring elements representing the interaction between the spine and the viscera, and vertical connecting elements with linear axial stiffness and cubic bending stiffness were used to connect adjacent visceral levels. Since there is no data for the viscera-spine interaction, the stiffnesses of these elements were taken as equal for all levels and identified by matching whole body impedance as described in Chapter III.

Table 2.4 gives the mass data for the pelvis through T10 of the ILSV. Table 2.5 lists the stiffnesses of the visceral elements. The masses for the remainder of the model and the stiffnesses of the intervertebral discs are given in Tables 2.2 and 2.3.

II.3 Ligamentous Spine with Ribs and Hydrodynamic Viscera

The complex spine model, which will be referred to as the CSM, includes a detailed representation of the rib cage, consisting of rib pairs 1 - 10 and the sternum. Each rib and the sternum are modeled as a rigid body. The ribs interact with vertebrae T1-T10 through the costovertebral and costotransverse joints, which are modeled as spring and beam elements respectively. Rib pairs 1 - 7 are connected to the sternum through the costo-sternal joints which are modeled as beam elements. Rib pairs 8 - 10 are connected to the adjacent ribs by spring elements representing the behavior of the interchondral cartilage. The actions of the intercostal tissues are also represented by spring elements.

The geometries and deformation characteristics of the rib cage, as reported by Belytschko, et al., (1976), were based on the measurements of Schultz, et al., (1974),

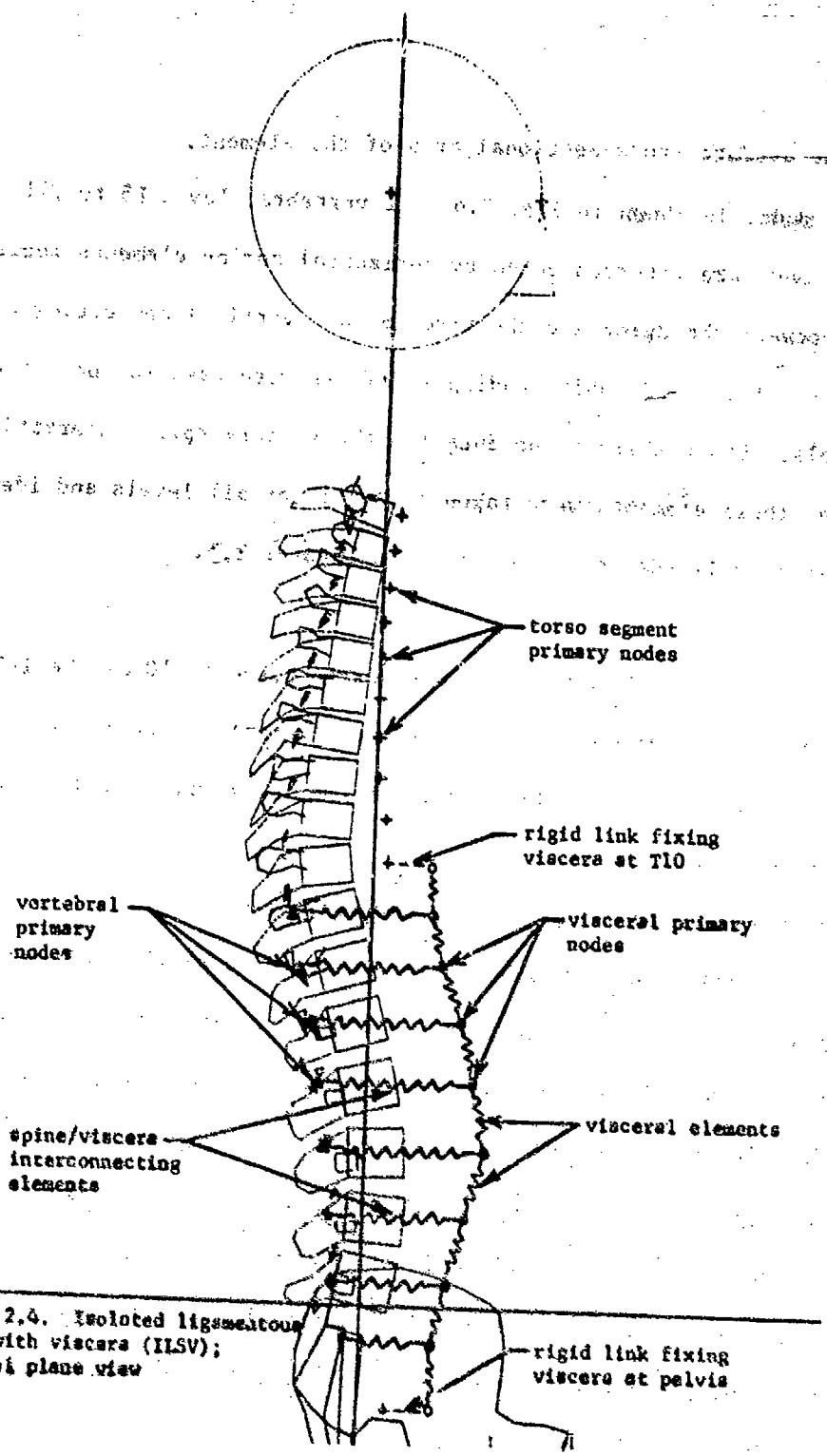

Figure 2.4. Isolated ligamentous spine with viscera (ILSV); sagittal plane view

Table 2.5. Isolated ligamentous spine with viscera (ILSV); viscera stiffnesses.

Visceral Element	Area (cm^2)	Length (cm)	Stiffness (dyne/cm x 10^7)
Pelvis-S1	191.56	3.59	0.92
S1-L5	268.77	3.60	1.29
L5-L4	370.80	3.83	1.68
L4-L3	371.35	3.93	1.64
L3-L2	425.65	3.87	1.91
L2-L1	468.90	3.65	2.24
L1-T12	472.10	3.37	2.42
T12-T11	459.20	3.03	2.62
T11-T10	459.20	2.79	2.86

All viscera-spine interconnecting element stiffnesses = 1.0 x 10^6 dyne/cm

and the work of Andriacchi, et al., (1974), respectively.

The abdominal viscera are modeled by hydrodynamic elements stacked in series between the pelvis and rib pair 10. An effective bulk modulus of 1×10^5 dynes/cm^2 was used for the viscera. Figures 2.5 and 2.6 depict the frontal and sagittal plane views of the ligamentous spine with ribs and hydrodynamic viscera. Tables 2.6 and 2.7 present the inertial and stiffness data as reported by Belytschko, et al., (1976). The stiffnesses of the spine elements are identical to that given in Table 2.2.

II.4 Simplified Spine Model

Although the ILSV is the model of primary interest for the impedance study in Chapter III, it is felt that even this model is computationally too time consuming to serve as a design tool. Therefore an equivalent simplified model of the ILSV was constructed. This simplified spine model (Fig. 2.7), will here be referred to as SSM. In this model, the thoracolumbar spine is modeled with three beam elements, T1 - T10, T10 - L3, and L3 - S1. The longitudinal actions of the viscera are modeled with four sping elements and 3 masses between the pelvis and T10. The interaction between the viscera and the spine is modeled with a spring element at each visceral mass. As with the ILSV, the viscera/spine interaction spring stiffnesses were adjusted by the impedance studies.

Tables 2.8 and 2.9 list the SSM mass and stiffness data. The SSM translational mass data was computed by summing the appropriate ILSV translational masses. The SSM rotational mass data was computed using the parallel axes theorem. The SSM stiffness data was determined from series combinations of the corresponding ILSV elements.

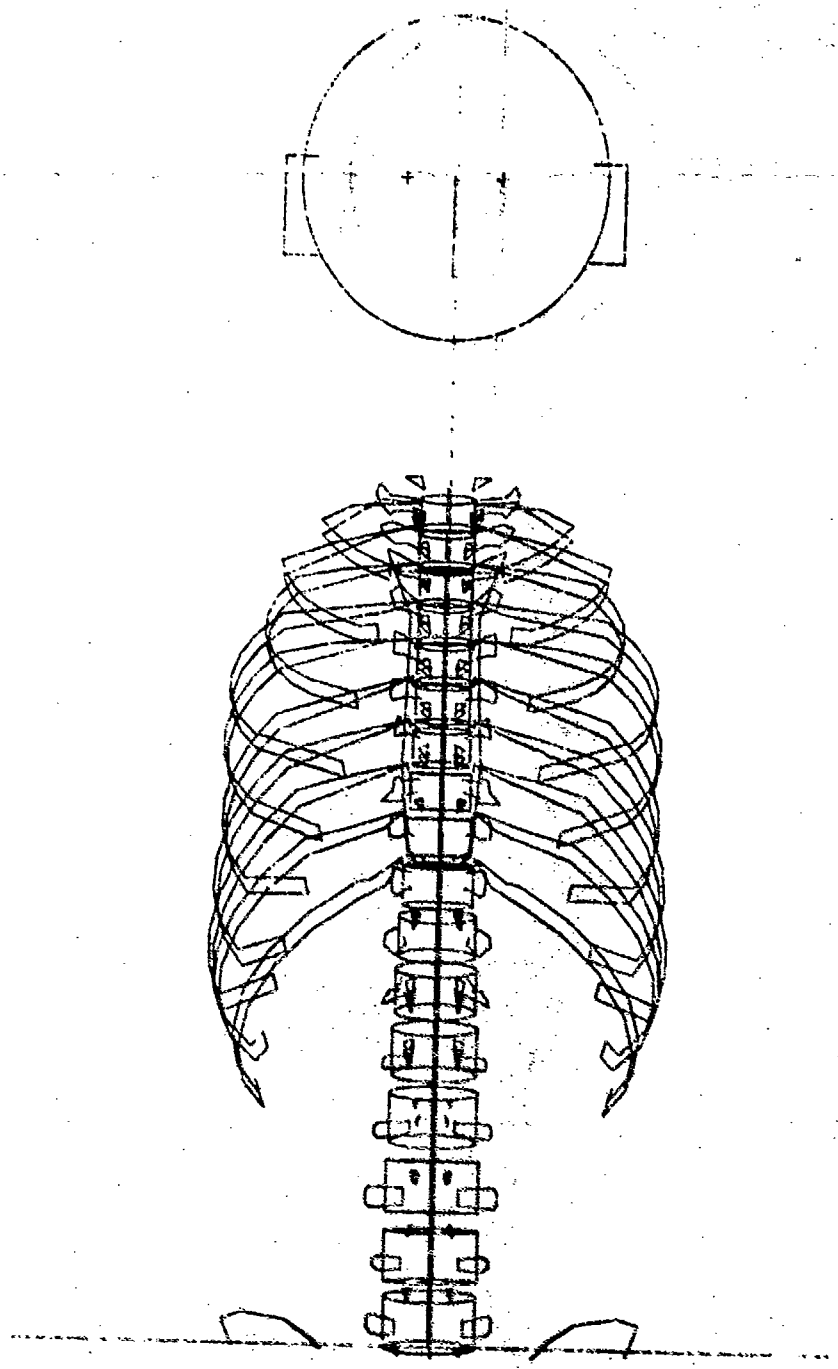

Figure 2.5. Complex spine model (CSM); Frontal plane view.

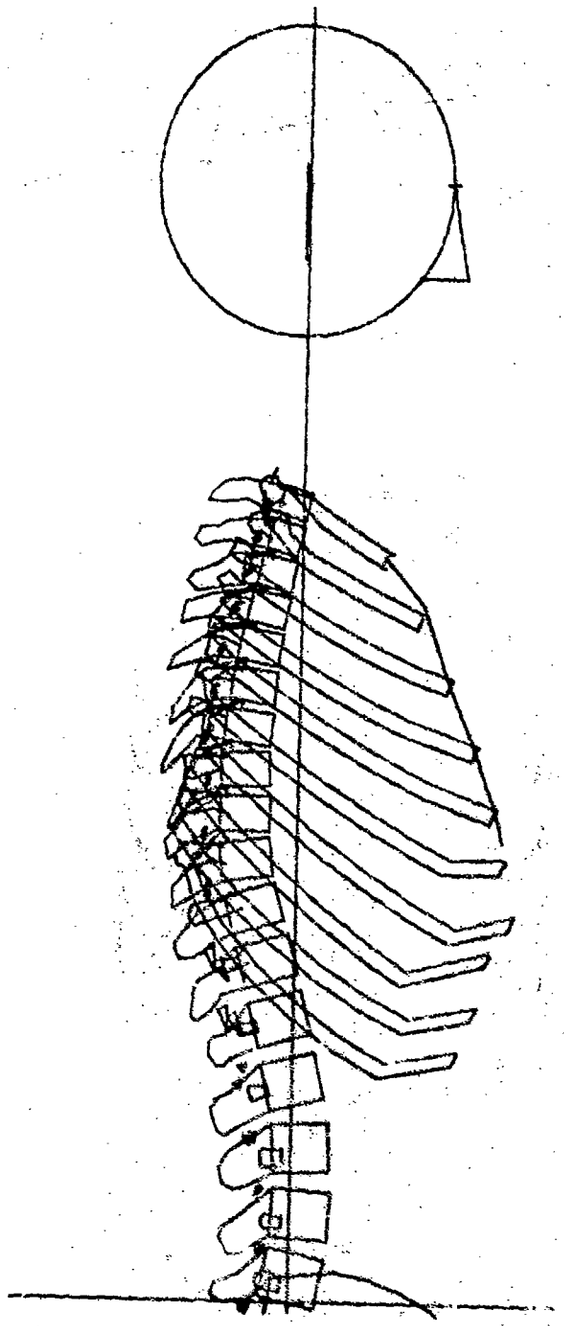

Figure 2.6. CSM; Sagittal plane view.

Table 2.6. Complex Spine Model (CSM) inertial data, Belytschko, et al., (1976)

Vertebral level	Mass in Grams x 10^8	I_{xx} Gram-cm^2 x 10^4	I_{yy} Gram-cm^2 x 10^5	I_{zz} Gram-cm x 10^5
Pelvis	16.200	128.000	20.000	19.300
L5	1.500	2.783	1.795	2.382
L4	1.500	2.748	1.704	2.291
L3	1.500	2.809	1.682	2.280
L2	1.500	2.840	1.695	2.291
L1	1.500	2.740	1.569	2.212
T12	1.556	7.002	1.309	1.919
T11	1.453	7.056	1.230	1.941
T10	1.202	6.028	1.129	1.648
T9	1.267	6.164	1.230	1.716
T8	1.176	5.543	1.208	1.670
T7	1.158	5.347	1.219	1.659
T6	1.043	4.425	1.162	1.546
T5	1.025	3.383	1.151	1.490
T4	0.964	3.138	1.060	1.354
T3	1.010	2.878	1.174	1.422
T2	0.974	2.007	1.029	1.230
T1	1.209	0.745	0.518	1.716
C7-C2	1.000	0.700	0.500	1.500
Head	5.612	44.786	4.044	3.385
Ribs T1 to T10	0.074	0.373	0.074	0.074
Lower Viscera	1.500	10.700	0.550	1.000
Upper Viscera	1.500	10.700	0.550	1.000

Table 2.7 Stiffness data for deformable elements in CSM rib cage, Belytschko, et al., (1976)

Joint Name	Connecting Motion Segment	Motion Segment Level	Axial Stiffness dyne/cm x 10^7	Torsional Stiffness dyne-cm x 10^8	Bending Stiffness dyne-cm x 10^7
Costo-Vertebral	Rib-vertebrae	T1-T10	5.0	0.35	7.5
Costo-Transverse Process	Rib-vertebrae	T1-T10	5.0		
Intercostal	Rib-rib	T6-T10	5.0	1.0	2.5
Interchondral Cartilages	Rib-rib	T1-T10	2.0		
Costo-Sternal	Rib-sternum	T1-T2	5.0	1.0	7.0
		T3-T5	5.0	1.0	2.5
		T6-T7	5.0	1.0	1.5

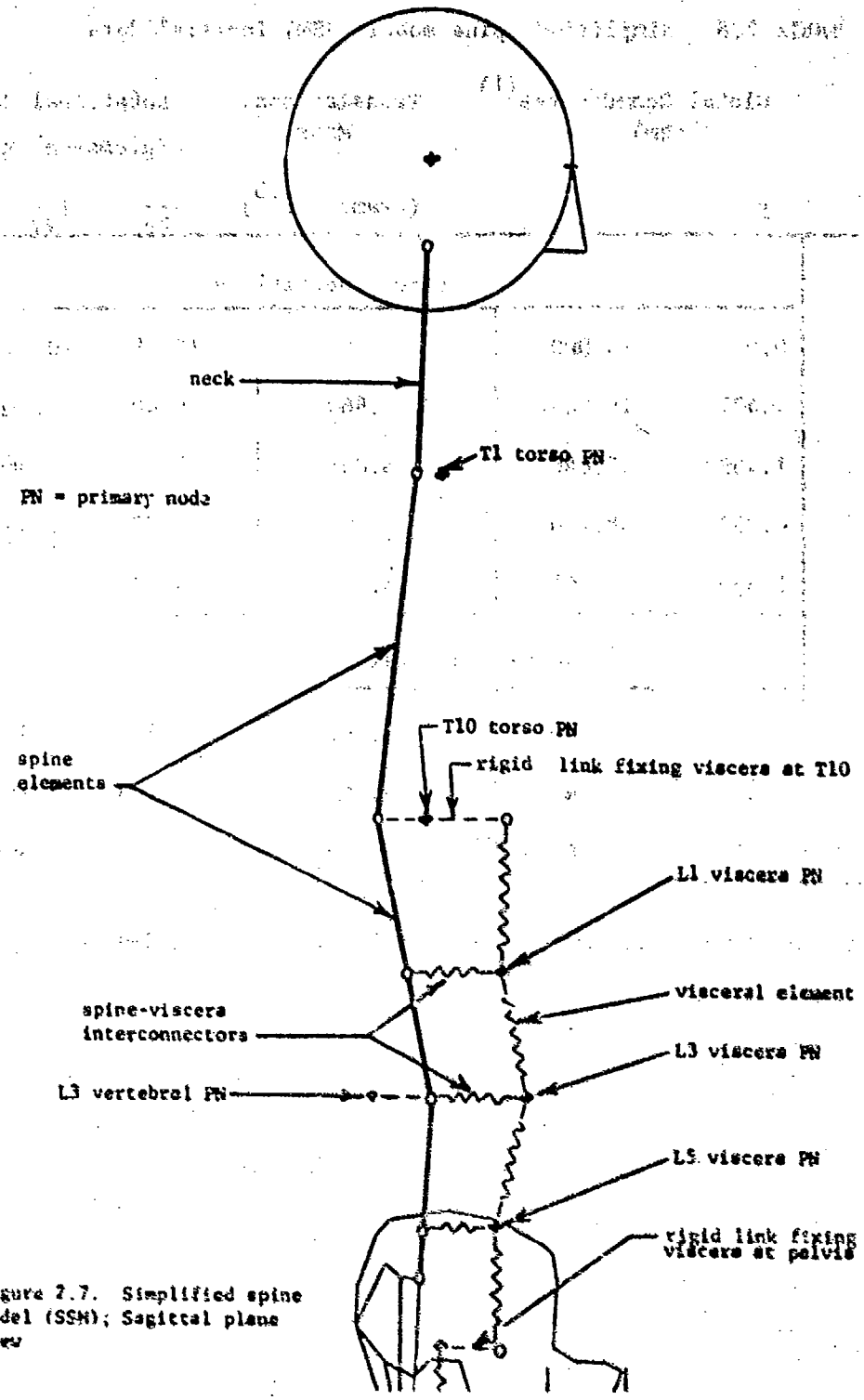

Figure 2.7. Simplified spine model (SSM); Sagittal plane view

Table 2.8. Simplified spine model (SSM) inertial data

Level	Global Coordinates[1] (cm) y	z	Translational Mass (grams x 10^3)	Rotational Masses (grams-cm^2 x 10^5) I_{xx}	I_{yy}	I_{zz}
	Spine Inertial Data					
Pelvis	0.0	-4.000	14.880	13.08	20.29	19.38
L3	4.497	10.940	1.660	0.40	0.58	0.28
T10	1.469	27.640	6.846	5.328	8.560	8.307
T1	0.857	48.240	5.591	2.773	6.438	7.212
Head	1.660	66.800	5.612	4.479	4.044	3.385
	Visceral Inertial Data					
L5	-3.407	3.190	4.295	1.272	2.985	3.158
L3	-5.321	10.940	3.368	1.203	3.484	3.746
L1	-3.515	18.460	5.134	2.576	5.598	6.257

[1] Global coordinates of mass centers. All global x coordinates = 0.0

Table 2.9. Simplified spine model (SSM) stiffness data

Element	Axial Stiffness dyne/cm x 10^7	Torsional Stiffness dyne/cm x 10^8	Bending Stiffness dyne/cm x 10^8
Neck	14.40	5.17	6.89
T1-T10	15.40	0.49	0.67
T10-L3	34.70	1.87	2.15
L3-S1	56.80	3.50	3.43
T10-L1 V[1]	0.88		
L1-L3 V	1.03		
L3-L5 V	0.83		
L5-Pelvis V	0.54		

[1] V = viscera

All viscera-spine interconnecting element stiffnesses = 1.00 x 10^7 dyne/cm

CHAPTER III

IMPEDANCE

III.1 Rationale and Overview

Driving point impedance can be broadly defined as the ratio of the force at the driving point to the velocity of the driving point. More specifically, impedance is the complex ratio of the transforms of the force and velocity. The quantity of interest to us is the impedance magnitude or the modulus of impedance, which is a function of the excitation frequency. An impedance[1] plot for a linear system gives insight into the frequency content of the system, and the effect of the damping, stiffness and mass associated with different elements of the system.

If a model is to duplicate the dynamic behavior of a physical system, it must duplicate the impedance of that system. In particular, any model of the human body must have the same impedance characteristics as that measured for the human body if any validity is to be ascribed to it.

It is interesting that in spite of the fact that extensive impedance measurements have been made of the human body and in fact constitute the largest available set of experimental data for dynamic response, the impedance of models such as those of Orne and Liu (1970), and Prasad and King (1974) were not compared to experimental results.

One reason for this is that the determination of the impedance through direct integration is a laborious process, since the model has to be excited harmonically until steady state response is obtained at each frequency that the impedance is desired. In this investigation, a Fast Fourier Transform technique was developed

---

[1] We will use impedance to mean modulus of impedance for convenience.

through which the impedance over a frequency range of interest can be determined from one time history, so that a single run suffices to establish the impedance curve.

The mathematical background of this method and some basics of the concept of impedance are developed in the next Section. We then review the experimental literature on impedance of human subjects. The final two Sections give our results for the impedance of the SSM and ILSV models described previously. The models described in Belytschko, et al., (1976) did not match the experimental impedance satisfactorily, so the alterations necessary to match experimental impedance are described in these sections. In addition, these impedance studies were used to identify the stiffnesses and damping constants of the elements interconnecting the viscera and vertebrae.

III.2 Mathematical Preliminaries

A transfer function for a linear system is the ratio of the transforms of an input variable and an output variable. Hence, impedance is a transfer function. The systems we are considering are stable, that is, they are systems whose natural responses decay with time. The excitations we are considering are such that they can be represented by exponentials whose frequencies lie along the imaginary axis. In this case, the impedance is defined by

$$Z(\omega) = \frac{F(\omega)}{V(\omega)} \tag{3.1}$$

where an uppercase letter indicates the Fourier transform defined by

$$F(\omega) = \int_0^\infty f(t)\, e^{-j\omega t}\, dt \tag{3.2}$$

$$f(t) = \frac{1}{2\pi} \int_{-\infty}^{\infty} F(\omega)\, e^{j\omega t}\, d\omega . \tag{3.3}$$

As an example consider a simple damped oscillator excited by a unit step velocity at its support. The equation of motion for this system is

$$m\ddot{x}_2 + c\dot{x}_2 + kx_2 = c\dot{x}_1 + kx_1 \quad , \tag{3.4}$$

which, since $\dot{x}_1 = 1$ and $x_1 = t$ can be written as

$$m\ddot{x}_2 + c\dot{x}_2 + kx_2 = c + kt \quad . \tag{3.5}$$

The solution to (3.5) is

$$x_2 = -\frac{e^{-\mu\beta t}}{\beta_d} \sin \beta_d t + t \tag{3.6}$$

where

μ = damping ratio = $\frac{c}{2\sqrt{km}}$

β = natural circular frequency = $\sqrt{k/m}$

β_d = damped natural circular frequency

$= \beta\sqrt{1 - \mu^2}$

The force transmitted to the support is given by

$$f(t) = k(x_2 - x_1) + c(\dot{x}_2 - \dot{x}_1) = -m\ddot{x}_2 \tag{3.7}$$

or, using the solution for the step velocity input given by Eq. (3.6),

$$f(t) = -\frac{m\beta e^{-\mu\beta t}}{\sqrt{1-\mu^2}} \left\{(1-2\mu^2) \sin \beta_d t + 2\mu\sqrt{1-\mu^2} \cos \beta_d t\right\} \quad . \tag{3.8}$$

The transforms required in Eqs. (3.1) are

$$F(\omega) = \int_0^\infty f(t)\, e^{-j\omega t}\, dt$$

$$= \frac{m\beta(\beta + 2\mu j\omega)}{(j\omega)^2 + 2\mu\beta j\omega + \beta^2} \tag{3.9}$$

and

$$V(\omega) = \int_0^\infty \dot{x}_1(t)\, e^{-j\omega t}\, dt$$

$$= \frac{1}{j\omega} \quad . \tag{3.10}$$

The impedance of this system is then given by the magnitude of the ratio of Eqs. (3.9) and (3.10),

$$Z(\omega) = \frac{m\beta\omega\sqrt{\beta^2 + (2\mu\omega)^2}}{\sqrt{(\beta^2 - \omega^2)^2 + (2\mu\omega\beta)^2}} \quad . \tag{3.11}$$

If we define the frequency ratio $r = \omega/\beta$, Eq. (3.11) can be written as

$$Z(r) = \frac{m\omega\sqrt{1+(2\mu r)^2}}{\sqrt{(1-r^2)^2 + (2\mu r)^2}} \tag{3.12}$$

For negligible damping ($\mu \approx 0$), $Z(r) \to \infty$ at $r = 1$, or $\omega = \beta$, that is, the impedance becomes infinite for the undamped system when the driving frequency is equal to the natural frequency. For increasingly larger μ, the maximum of (3.12) occurs further and further to the right of $r = 1$ and the maximum impedance decreases.

As the number of degrees of freedom, and hence complexity, of a mechanical system increases, it becomes increasingly difficult to obtain analytical expressions for the response and hence the impedance of the system. A time history response obtained by a transient analysis of the system is therefore used to obtain the impedance. The transient response is in the form of discrete values at equal time intervals. If the multidegree of freedom system being considered is linear and stable, and if the excitation is expressible in terms of exponential components

of the form $e^{j\omega_n t}$, where ω_n now represents a discrete spectrum of frequencies, the response can be transformed by means of the discrete Fourier transform (DFT) via its computer based algorithm, the Fast Fourier Transform (FFT) (Brigham (1974), Holmes (1976)).

The DFT form of the Fourier transform pair in Eqs. (3.2) and (3.3) is

$$F(\omega_n) = \sum_{k=0}^{N-1} f(k\Delta t)\, e^{-j\omega_n t_k} \tag{3.13}$$

$$f(k\Delta t) = \frac{1}{N}\sum_{n=0}^{N-1} F(\omega_n)\, e^{j\omega_n t_k} \tag{3.14}$$

where Δt is the sampling interval, i.e. the time step used in the transient analysis, N the number of steps, and ω_n the nth frequency, which is given by

$$\omega_n = \frac{2\pi n}{N\Delta t} \tag{3.15}$$

The impedance of a model is obtained by prescribing a unit step velocity at the driving point, which in the simulations reported here is either the seat or the pelvis. The force time history at the driving point, f(t), and its discrete Fourier transform are then obtained. The transform of the velocity time history is given by Eq. (3.10), and the ratio of the magnitudes of the two transforms, Eq. (3.1), gives the driving point impedance that is used here; phase angles were not determined.

A drawback of this approach is that a numerical solution of a system with a unit step velocity applied directly to a mass (e.g. the pelvis) does not take into account the mass at which the velocity is applied because the acceleration of the mass, which is a unit impulse analytically, is zero for the discrete system except at the time zero, where it is not computed. In other words, the acceleration time history associated with a unit step velocity is an impulse function, and this impulse will not appear in the numerical results. Hence the internal force at the mass will not reflect the presence of the mass.

However, it should be noted that when the system is driven through the mass, the mass is essentially in parallel to the rest of the system. It is therefore possible to compute the impedance of the entire system by obtaining the impedance of the system without the mass as described above, and then adding to this the impedance of the mass.

This difficulty occurs only when the driving point is the pelvic mass. However when the seat is the driving point, the seat-buttocks stiffness dominates the impedance. Since it is experimentally almost impossible to drive a human being at the pelvis, the impedance curves which do not include the seat are physically unrealizable, but they are indicative of the frequency character of the spine itself.

In Appendix A, the DFT method used here and the programming details are described.

III.3 Summary of Impedance Literature

In this section we will review the literature on experimentally determined impedances of human subjects. The papers of major interest are those of Coermann, et al., (1959-1960) and Vogt, et al., (1968). Coermann determined the impedance of sitting and standing subjects by shake table induced longitudinal vibrations through a frequency range of 1 to 20 Hz. Figure 3.1 shows the median impedance of five sitting subjects reported by Coermann. Also shown is an impedance curve for a one degree of freedom system, Eq. 3.12, with Coermann's values for the mass, stiffness, and fraction of critical damping. Figure 3.2 shows the effects of variation in body postures as determined experimentally by Coermann. The impedance of the abdominal viscera was also studied by Coermann by placing the subject in a supine position on a shake table and subjecting him to longitudinal harmonic vibrations through a frequency range of 1 to 15 Hz. Motion of the skeleton was suppressed by using metal brackets at the head, shoulders and feet, to clamp the subject to the table.

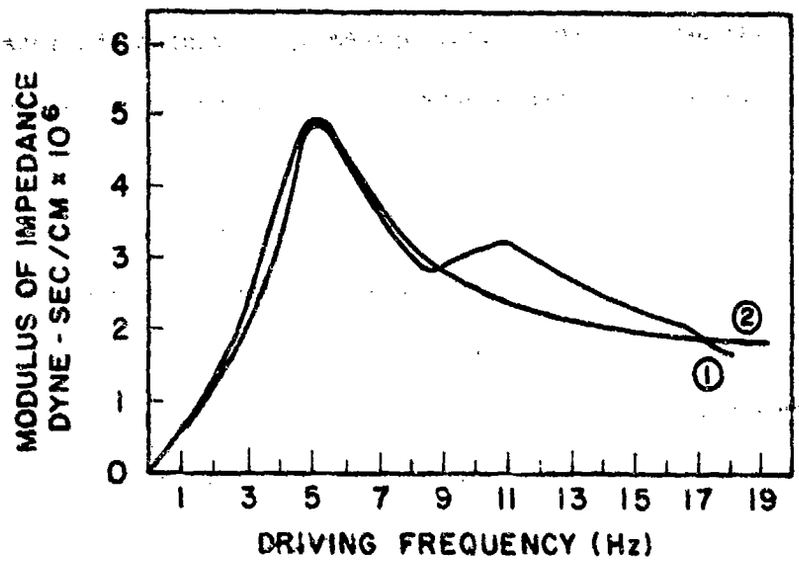

Figure 3.1. Comparison of the median of the experimentally measured impedances of 5 sitting subjects (longitudinal vibrations) to a single degree-of-freedom system with m = 84000 grams, $\beta = 10\pi$ and $\mu = 0.312$. (Coermann, et al., (1960)); (1) experimental; (2) computed.

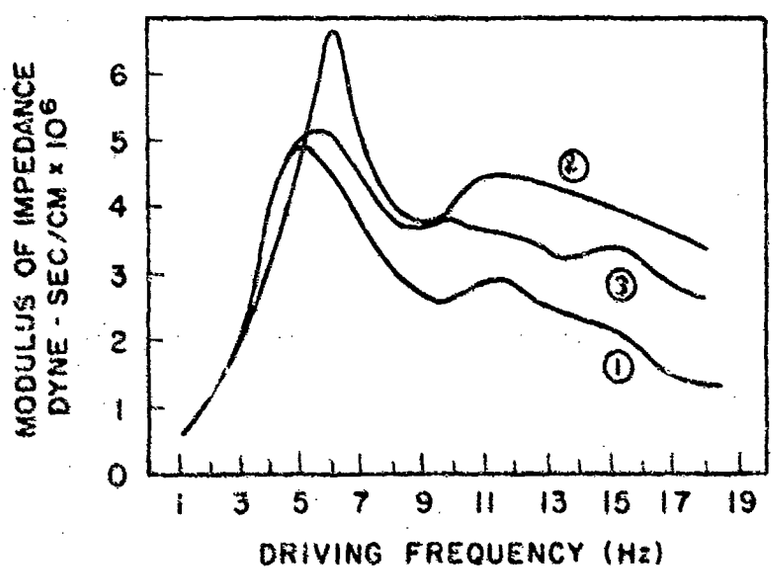

Figure 3.2. Influence of body posture on the mechanical impedance of a human subject; (1) sitting relaxed; (2) sitting erect; (3) standing erect. (Coermann, et al., (1960)).

Figure 3.3 shows the variation of abdominal wall displacement with excitation frequency as measured by Coermann, et al. A resonance in the abdominal wall displacement was detected between 3 and 4 Hz, so this would indicate an impedance peak at between 4 and 5 Hz. Restricting the mobility of the abdomen resulted in a shift of the abdominal wall displacement peak to between 6 and 7 Hz.

Vogt, et al., (1968) measured the impedance of ten male subjects. The subjects were seated and loosely restrained. Figure 3.4 shows the average impedance of these subjects. An important characteristic of the above experimental impedances is the peak which occurs around 5 Hz. A second peak, which is generally considerably smaller than the first, occurs around 14 Hz. These peaks in the impedance curve indicate the excitation frequencies at which the maximum energy is transferred to the body. Coermann suggests that the 5 Hz peak is caused by resonant motion of the upper torso in connection with the bending elasticity of the pelvis and spine, and that the 14 Hz peak is probably attributable to another elasticity of the pelvis.

Vykukal (1968), exposed 4 subjects in a semi-supine position to a vertical acceleration of ± 0.4 G in a frequency range from 2½ to 20 Hz, combined with a linear acceleration of 1, 2½, and 4 G. The mechanical impedance of each subject was recorded. He observed that for the higher linear accelerations, the stiffness increased, the damping decreased, and the overall impedance increased. The resonances at higher frequencies became more predominant in magnitude because of increased coupling of the body systems when subjected to a high G environment. Unfortunately, neither the direction of the harmonic oscillation vector nor the direction of the linear acceleration vector with respect to the subject's longitudinal axis were specified.

Woods (1967), reported transmissibilities for longitudinal and lateral vibrations of three subjects in the frequency range of 1 to 10 Hz. Results are also reported for the effect of random vertical and lateral vibrations. All of the transmissibility

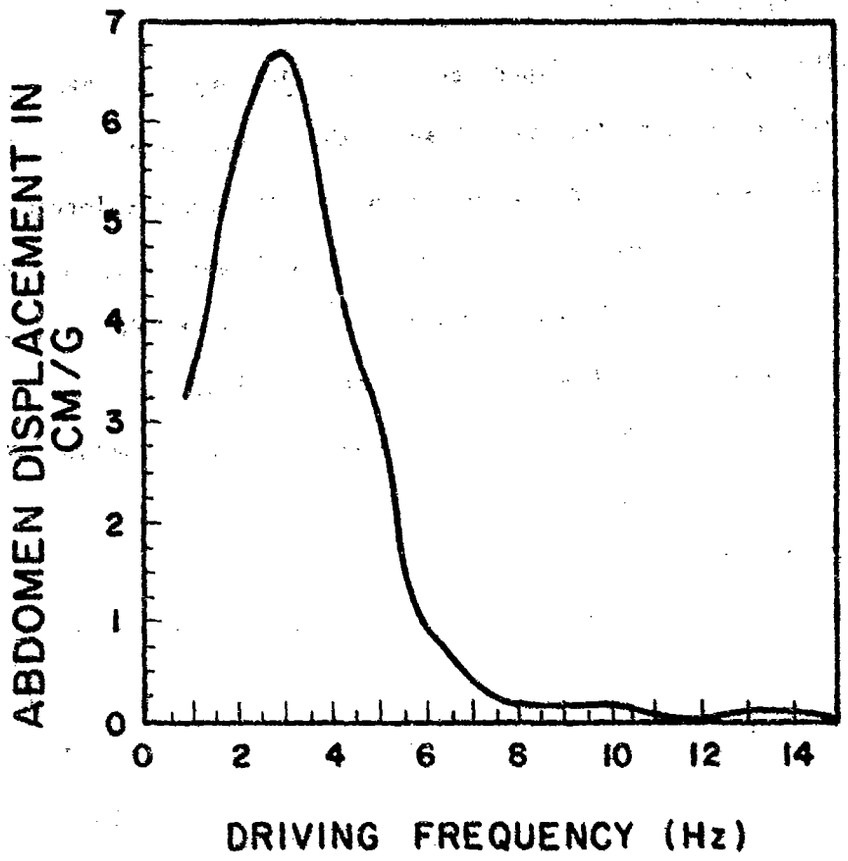

Figure 3.3. Abdominal wall displacement versus excitation frequency for a human subject in the supine position exposed to longitudinal vibrations. (Coermann, et al., (1960)).

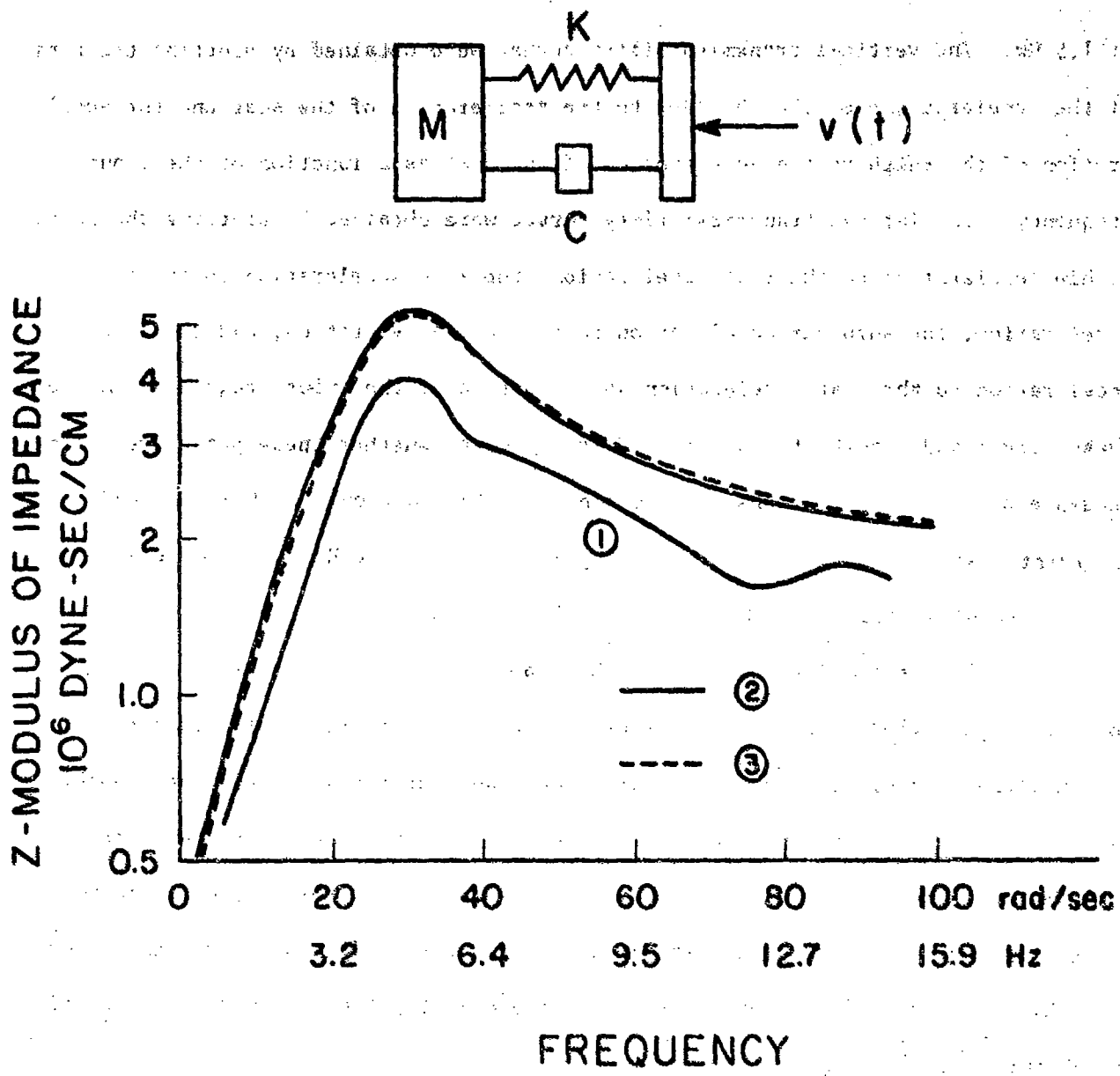

Figure 3.4 Comparison of experimentally, analytically and numerically determined impedance curves; (1) experimentally determined impedance curve of Vogt, et al., (2) analytically computed impedance curve for single degree of freedom system; (3) numerically determined impedance curve for single degree of freedom system.

curve for the sinusoidal, longitudinal oscillations had a peak between 4 to 6 Hz. A peak in the transmissibility for the sinusoidal, lateral oscillations occured at 1.5 Hz. The vertical transmissibility curves were obtained by plotting the ratio of the accelerations of the shoulder to the acceleration of the seat and the acceleration of the thigh to the acceleration of the seat as a function of the input frequency. The lateral transmissibility curves were obtained by plotting the ratios of hip acceleration to the seat acceleration, the knee acceleration to the seat acceleration, the shoulder acceleration to the seat acceleration, and the head acceleration to the seat acceleration as a function of the input frequency. All of these curves had a peak at 1.5 Hz. It is not clear whether these peaks are a consequence of human body response or the subjects' interaction with the seat and restraint system. However, the reported peak in the 4 to 6 Hz range correlates well with the results reported in Coermann, et al. and Vogt, et al.

It is also worthwhile to consider the impedance characteristics of previous models. Payne (1972) developed a four degree of freedom model of a seated man. It consisted of rigid masses representing the head, upper torso, abdominal viscera and pelvis, interconnected by springs and dampers. A spring and a damper were included to represent the elastic and viscous properties at the buttocks. Impedance curves for this model exhibit a peak at 9 Hz and a severe dip in the impedance curve at 12 Hz but no second resonance point, so they do not agree well with Vogt, et al. or Coermann, et al.

The impedance of the model in AMRL-TR-76-10 was not given, but modal analyses were performed. These modal analyses showed that the ligamented spine, with head and pelvis but no separate elements for the viscera and buttocks, and with only axial motion allowed, yielded a lowest natural frequency of 17 Hz. The mode shape associated with this frequency is approximately that of a free-free rod. This result indicates that the 5 Hz peak in the impedance curve reported experimentally

represents a resonance of either the viscera, the buttocks, or the bending response of the spine. The relatively low mass of the viscera would tend to rule it out as the sole source of this peak. It will be shown subsequently that the first peak in the impedance curve depends strongly on the stiffness of the buttocks and seat. It will also be shown that if the possibility of parametric excitation of the flexural spine modes is considered, a 5 to 7 Hz peak is present in the impedance curve even without the representation of the buttocks, but its magnitude is smaller than that found experimentally. Thus, the first resonance peak observed experimentally appears to arise from several components of the human body: the viscera, the seat-buttocks, and the bending response of the spine.

III.4 Impedance Results

Impedance curves were obtained for two of the models, the simplified spine model, SSM, and the isolated ligamentous spine with viscera, ILSV. These impedance studies were used to obtain the stiffnesses and damping constants for the elements interconnecting the spine and viscera. The stiffnesses were first determined in the SSM model by parametric studies.

The damping of these elements was then chosen so that the lowest "lateral visceral mode" (i.e. motion of the viscera laterally relative to the spine) was damped by the same amount as the lowest axial visceral mode. Based on the stiffnesses of the SSM viscera/spine interconnecting elements, initial values for the ILSV interconnecting elements were chosen. Only minor adjustments were necessary to match the experimental impedance.

Prior to applying the FFT impedance determination method to the spine models, it was applied to a one degree of freedom model using the mass, damping and frequency values used by Coermann, et al. (1960) for his one degree of freedom model of a 185 lb man. The numerical results are shown in Fig. 3.4 along with the analytical results of Eq. (3.11). The duration of the numerical simulation of the step

response here was 1.02 sec, which involved 256 time steps of 4 milliseconds. As can be seen, the results compare very well.

We will now give some of the results for the SSM model. The parametric studies used to determine the spine-viscera connection elements are not reported; the major emphasis in the following studies is the origin of the various resonances and the influence of certain parameters, such as seat-buttocks stiffness, on the impedance.

Figure 3.5 compares the impedance curves for the SSM without buttocks to the averaged experimentally obtained curve of Vogt, et al. The latter were obtained by vertical shaking of loosely restrained seated subjects, so the buttocks must be evidenced in the observed impedance. The pelvic mass here is 1.62×10^4 grams (36 lbs), but the total mass of 5.56×10^4 grams (123 lbs) does not include the upper or lower leg mass. The average mass of Vogt's subjects was 6.94×10^4 grams (153 lbs) (without the lower legs and feet, which are not included because the footrest of the experiment was not harmonically excited).

The impedance of the spine without buttocks, as shown in Fig. 3.5, exhibits peaks at approximately 5.70 Hz and 12.70 Hz respectively, both with and without the pelvic mass. In order to more clearly determine which subsystems are causing these peaks, the impedances of the spine and the viscera are given in Fig. 3.6. The axial response of the spine alone has one peak at 10.50 Hz, while the visceral column has a peak at approximately 5.37 Hz. These agree with the lowest frequencies, obtained from an axial modal analysis of the spinal column and visceral column with both ends fixed. The impedance of the spine and viscera combined, though dominated by the peak at approximately 10.74 Hz (again the first fixed-free spine axial mode) also exhibits the presence of the viscera with the "beginnings of a peak" at approximately 5.70 Hz. This curve is dominated by the spine peak because there is considerably more mass associated with the spine (e.g head, arms, etc.) than with the viscera. Nevertheless, the visceral contribution to the impedance curve is

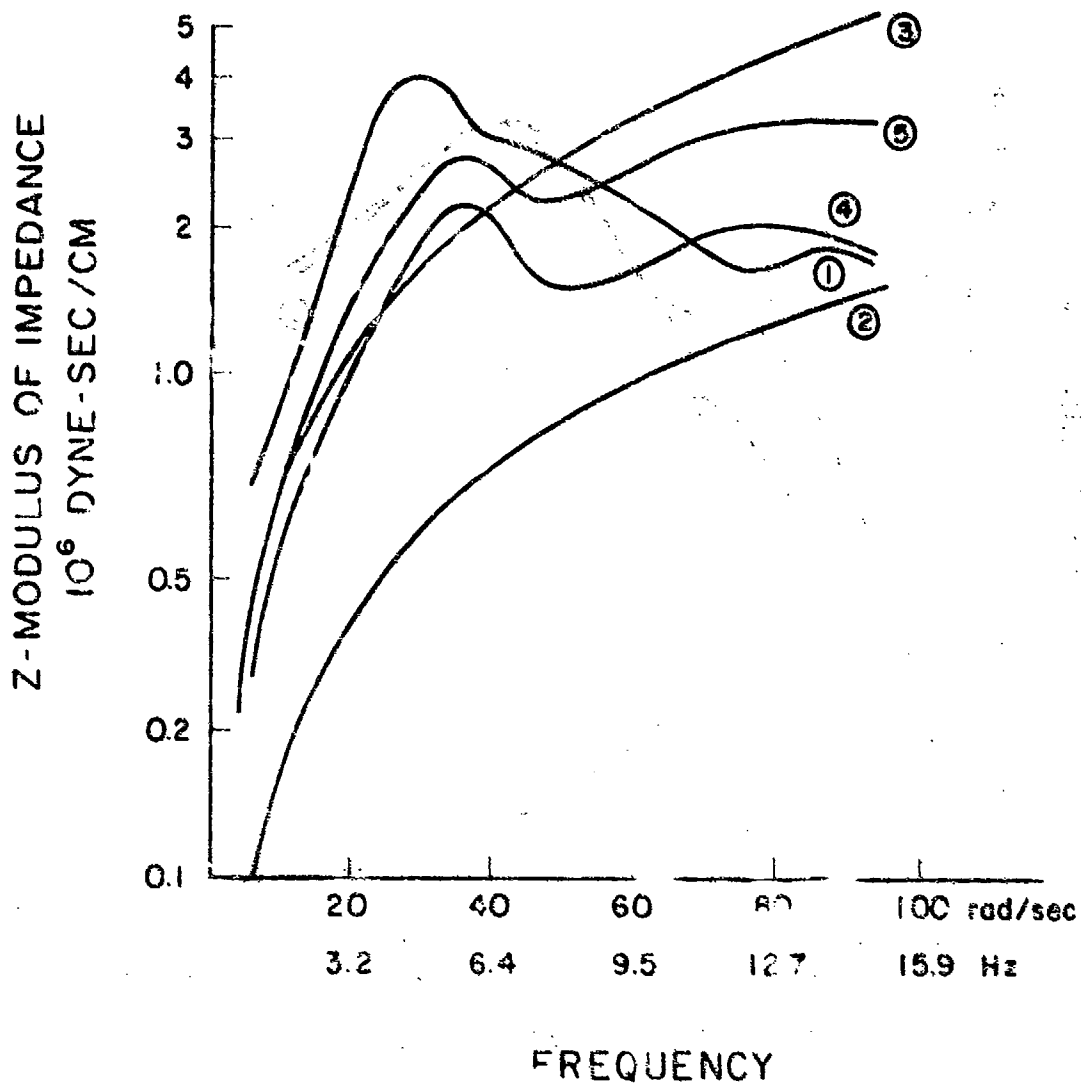

Figure 3.5. Impedance curves for the SSM without buttocks; (1) experimental curve of Vogt, et al.,; (2) SSM pelvic mass impedance; (3) SSM total mass impedance; (4) impedance of SSM without pelvic mass; (5) impedance of SSM with pelvic mass.

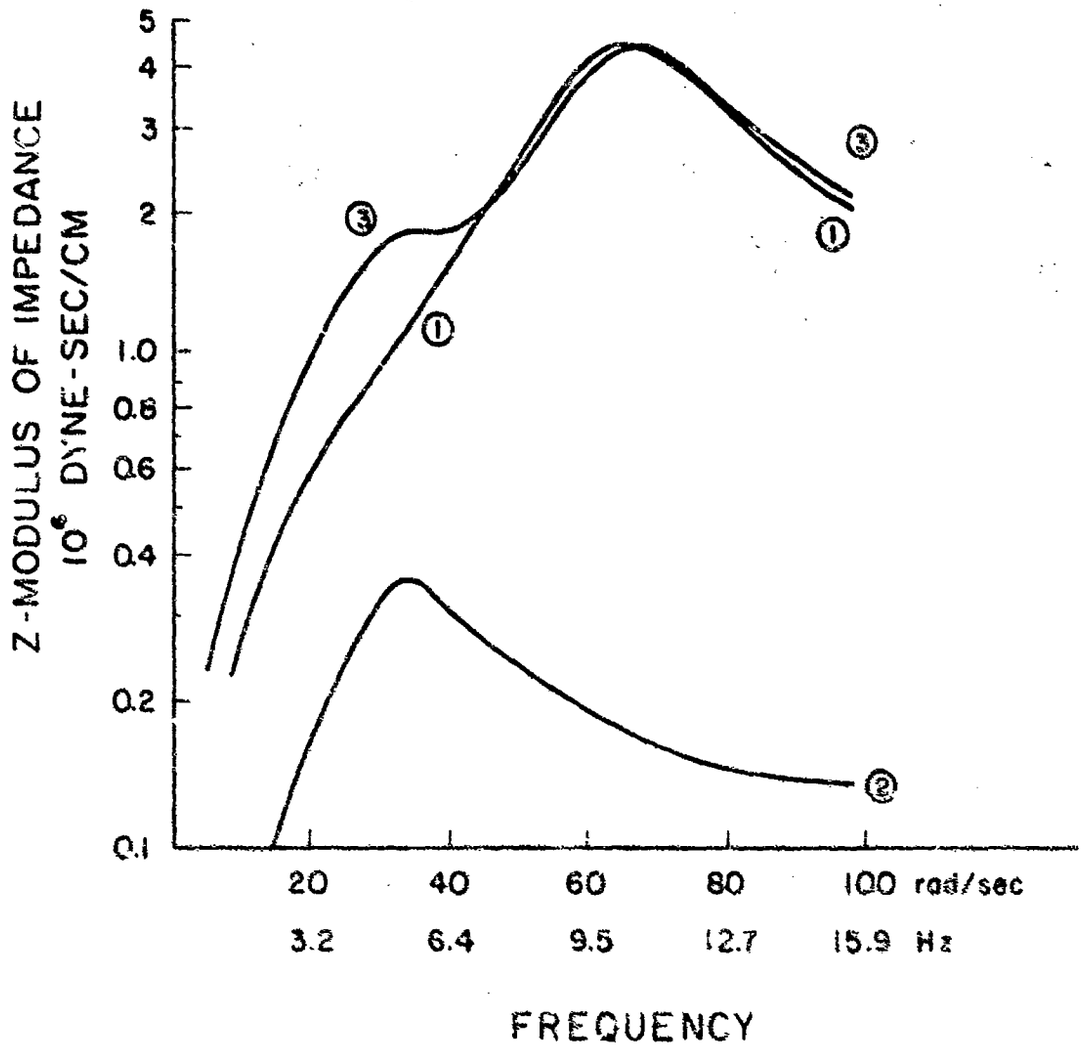

Figure 3.6. Impedances of SSM subsystems; (1) spine; (2) viscera; (3) spine and viscera. Curves (1), (2) and (3) restricted to axial motion only.

evident.

It is of interest to note that upon dropping the restriction of axial motion, we obtain the curves Fig. 3.5, which have a peak at 12.70 Hz. In the modal analysis results of SSM, the lowest visceral mode and the third spine bending mode (in which most of the energy is transmitted to the lumbar region) were at 5.35 Hz. The discrete internal force time history results for the spine element between S1 and L3 were in fact dominated by this frequency. This indicates that the third bending mode has been parametrically excited. A variation of the bending damping or visceral damping had its greatest effect in the region of the 5.70 Hz peak. These results indicate that SSM has a 5.70 Hz impedance peak due to the first visceral mode, and parametric excitation of the third bending mode, even in the absence of a seat-buttocks representation.

In determining the effects of the buttocks, the buttocks were modeled by a spring and damper between the pelvis centroid and the seat. Payne (1972) gives a value of 6.55×10^7 dynes/cm (374 lb/in) for the buttocks' stiffness. Buttocks stiffnesses of 6.55×10^7 and 1.31×10^8 dynes/cm were used here and half of the upper leg mass was added to the pelvic mass to yield a total SSM mass of 6.88×10^4 grams (152 lbs), because in the experiment the upper leg mass was vibrated along with the upper body.

Figure 3.7 shows the impedance of SSM with these two values of buttocks stiffness. Both curves exhibit a peak at 4.30 Hz and a much smaller peak at 9.30 Hz, with a slight shift to the right for the stiffer buttocks model. Modal analysis shows that the first axial mode of the buttocks-spine series combination occurs at 4.10 Hz and consists essentially of rigid body motion of the spine relative to the seat. The 9.30 Hz peak appears to correspond to a 9.10 Hz mode which consists primarily of the second visceral mode.

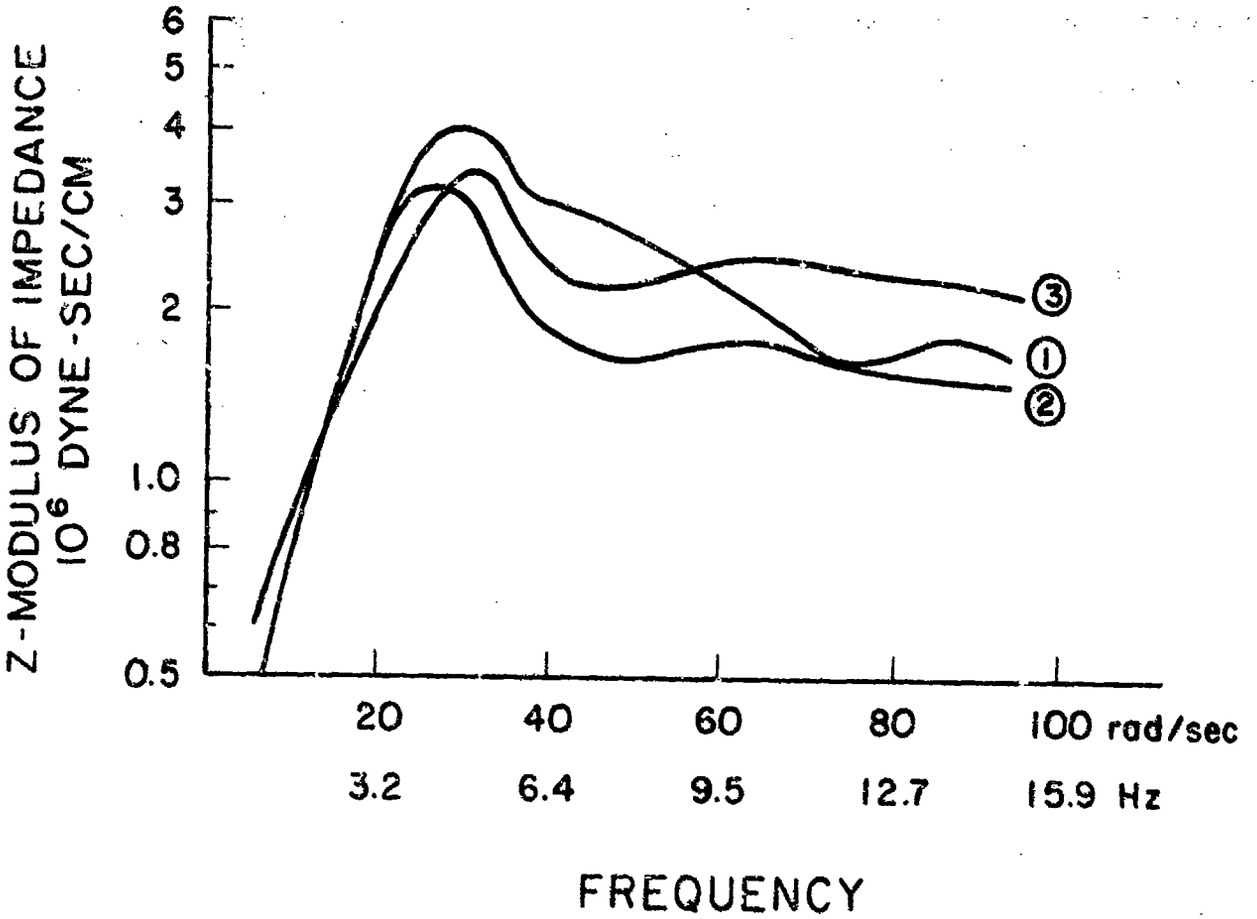

Figure 3.7. Impedance of SSM with buttocks: (1) experimental curve of Vogt, et al., (2) and (3) SSM with buttocks stiffnesses of 6.55×10^7 and 1.31×10^8 dyne/cm respectively.

From these results it becomes apparent that an impedance curve obtained by driving the buttocks is dominated by the steatopygic mode. This agrees with the findings of Payne and Band, (1969), who comment that the variability in impedance measurements of seated human subjects is very likely due to variations in buttock size, muscle tension, and tonus. It follows from this that impedance measurements of this type do not result in accurate information as to resonances of the subsystems. However, it is interesting to observe that the shift in impedance peaks due to a twofold change in buttocks stiffness is not severe.

Although not apparent in his results, Vogt, et al., (1968), reported that in most cases, a peak around 10 Hz is also evident. As discussed above, the impedance curve for the SSM with the buttocks exhibits a small peak around 10 Hz. However it cannot be established whether the peak in Vogt, et al is caused by the same mechanism which causes the 10 Hz peak in the SSM curves. Their impedance also exhibits a small peak at 14 Hz. This peak does not show up in the SSM curves.

It is clear from these results that the SSM model duplicates experimentally determined impedances very well. It not only replicates the peak magnitudes and the locations of these peaks, but it gives considerable insight into the resonance mechanisms.

We will now consider the impedance studies of the more complex model, ILSV, isolated ligamentous spine with viscera, which was described in Section II.2. Figure 3.8 shows the impedance curves for the ILSV without buttocks. For comparison, the experimental curve of Vogt, et al., (1968) is also shown. The pelvic mass, as for the SSM, is 1.62×10^4 grams (36 lbs), the total mass is 4.98×10^4 grams (110 lbs). The total mass does not include the upper or lower leg mass, nor the arm mass, which were included in the SSM. The impedances of the ILSV without and with the pelvic mass are given.

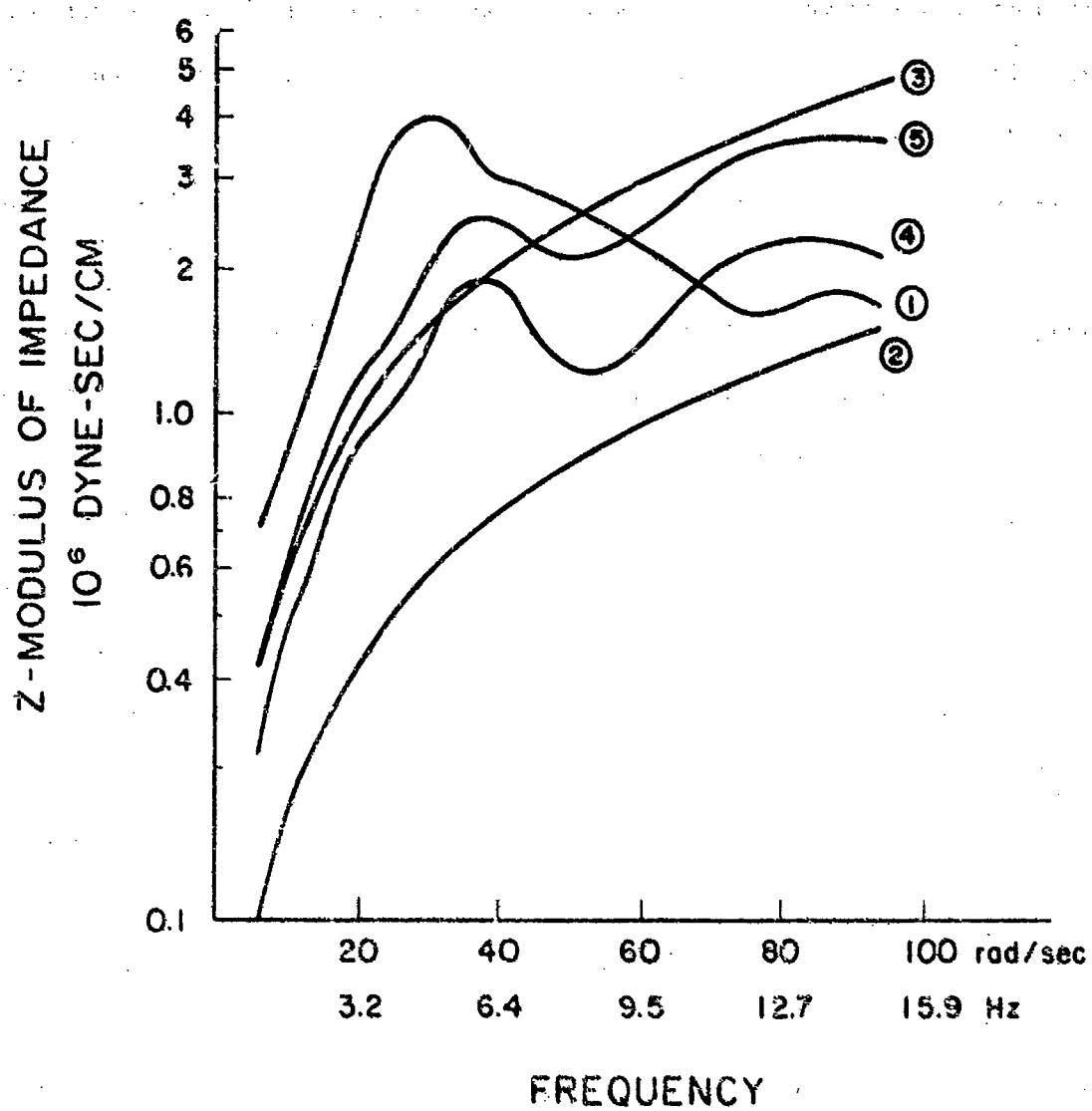

Figure 3.8. Impedance curves for the isolated ligamentous spine with viscera (ILSV) without buttocks: (1) experimental curve of Vogt, et al.; (2) ILSV pelvic mass impedance; (3) ILSV total mass impedance; (4) ILSV impedance without pelvic mass; (5) ILSV impedance including pelvic mass.

The impedance exhibits peaks at approximately 6.0 and 13.5 Hz, which agrees well with the corresponding SSM peaks at approximately 5.7 and 12.7 Hz. The 13.5 Hz peak corresponds to the first spine axial mode, 13.17 Hz, obtained in an ILSV modal analysis with the pelvis fixed. The 6.0 Hz peak results from a combination of the first visceral mode and what appears to be a bending mode. The visceral frequency is 5.5 Hz, and there are three bending modes in the 5-6 Hz region.

The impedance results for the ILSV with buttocks are shown in Fig. 3.9. The same buttocks stiffness as in the SSM, 6.55×10^7 dynes/cm, (374 lb/in) was used. Half of the upper leg mass was added to the pelvic mass to yield a total ILSV mass of 6.26×10^4 grams (138 lbs). The impedance of ILSV is given with buttock damping ratios of 0.3 and 0.15, respectively. The 4.8 Hz peak corresponds to the steatopygic mode (4.4 Hz) and as in the SSM, this mode dominates the impedance curve. A small peak is also observed at approximately 10.0 Hz, which appears to be associated with the second visceral mode.

Figures 3.10 and 3.11 compare the SSM and ILSV impedance curves without and with buttocks, respectively. Of primary interest is the similarity of the SSM and ILSV curves. This indicates that SSM and ILSV would respond almost identically for dynamic input with a frequency content of 16 Hz or less.

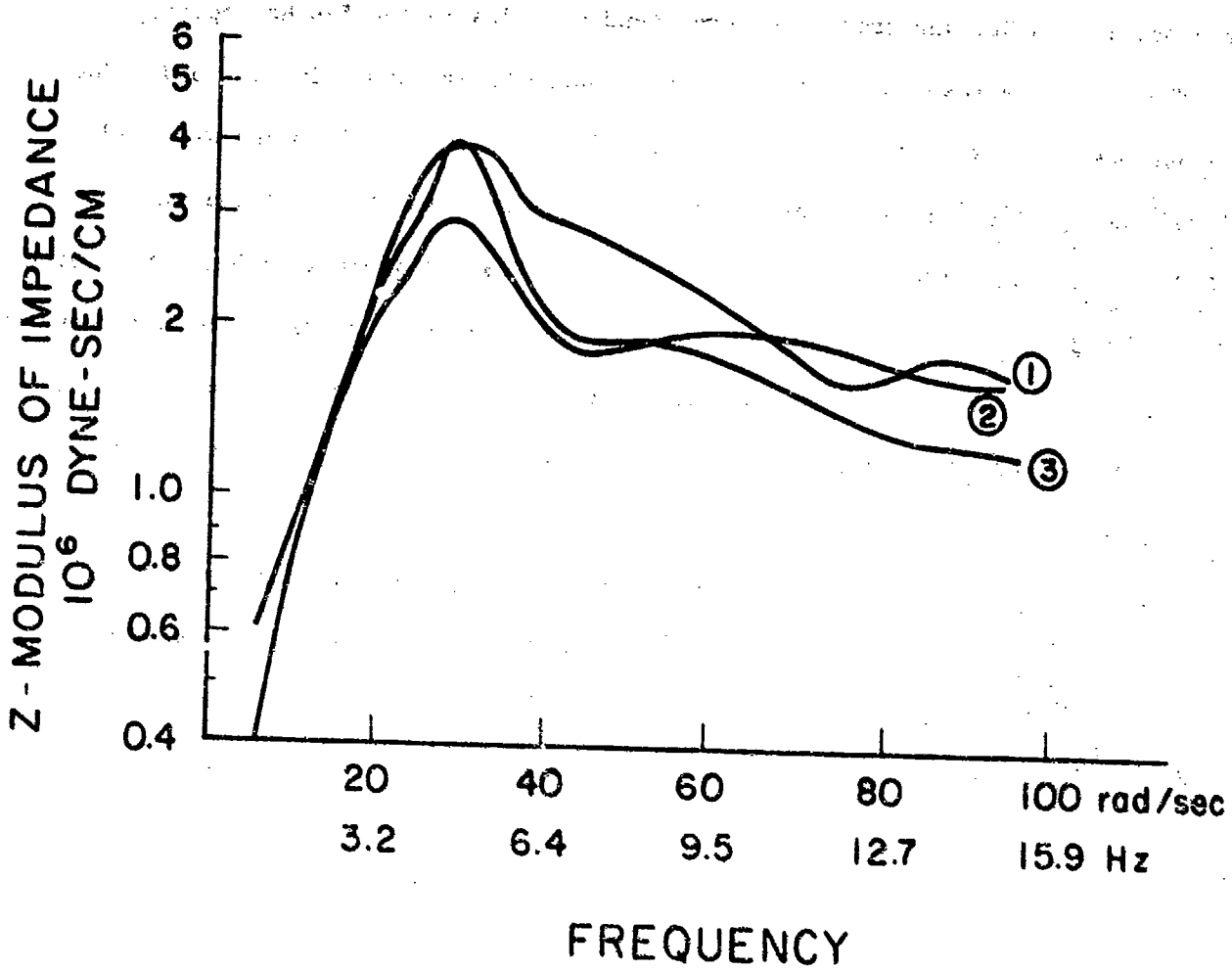

Figure 3.9. Impedance curves for isolated ligamentous spine with viscera (ILSV) with buttocks: (1) experimental curve of Vogt, et al., (2) and (3) are ILSV impedances with buttocks damping ratios of 0.3 and 0.15, respectively.

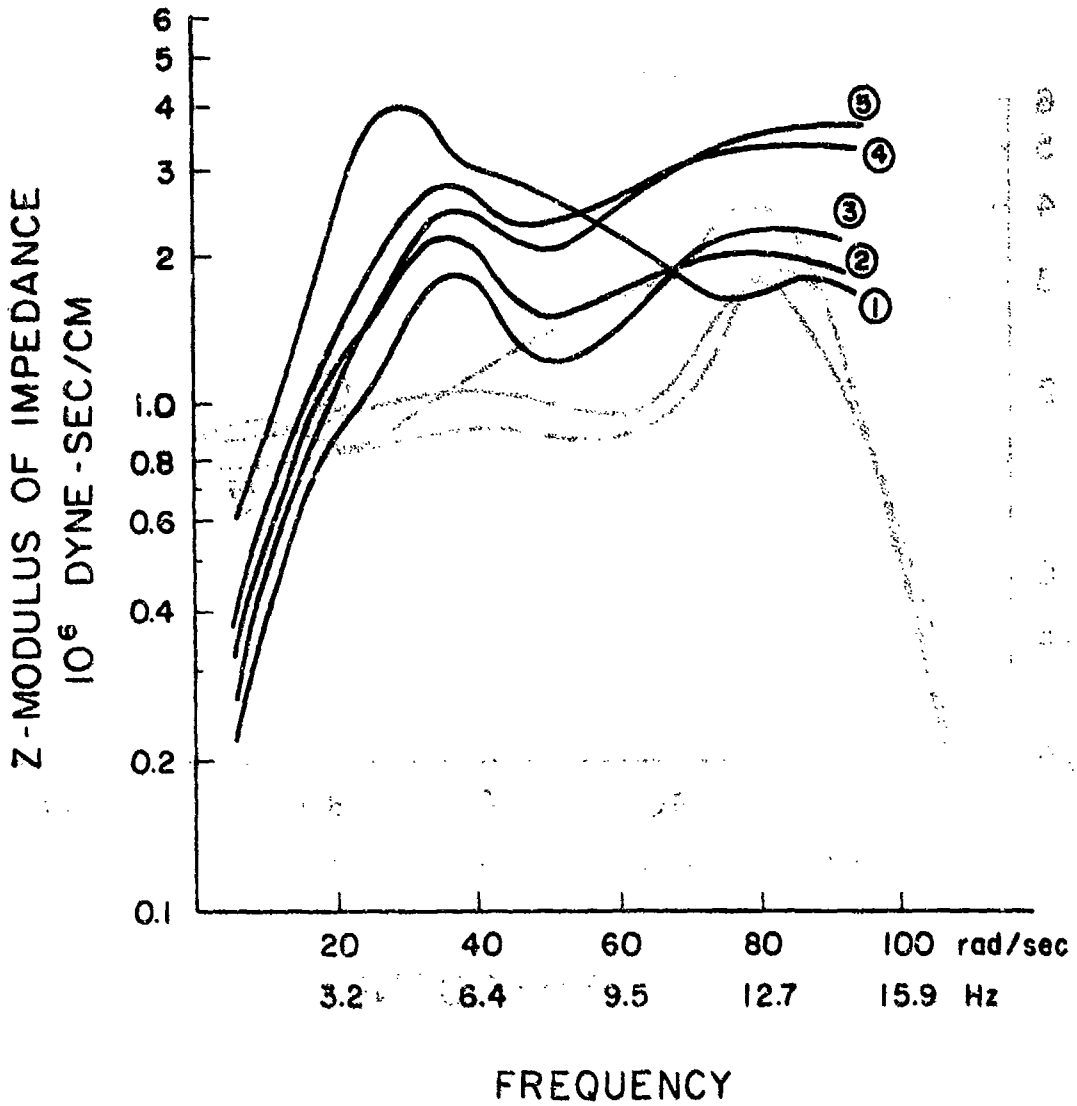

Figure 3.10. Comparison of impedance curves for SSM and ILSV without buttocks: (1) experimental curve of Vogt, et al.; (2) and (3) SSM and ILSV without pelvic masses respectively; (4) and (5) SSM and ILSV with pelvic masses respectively.

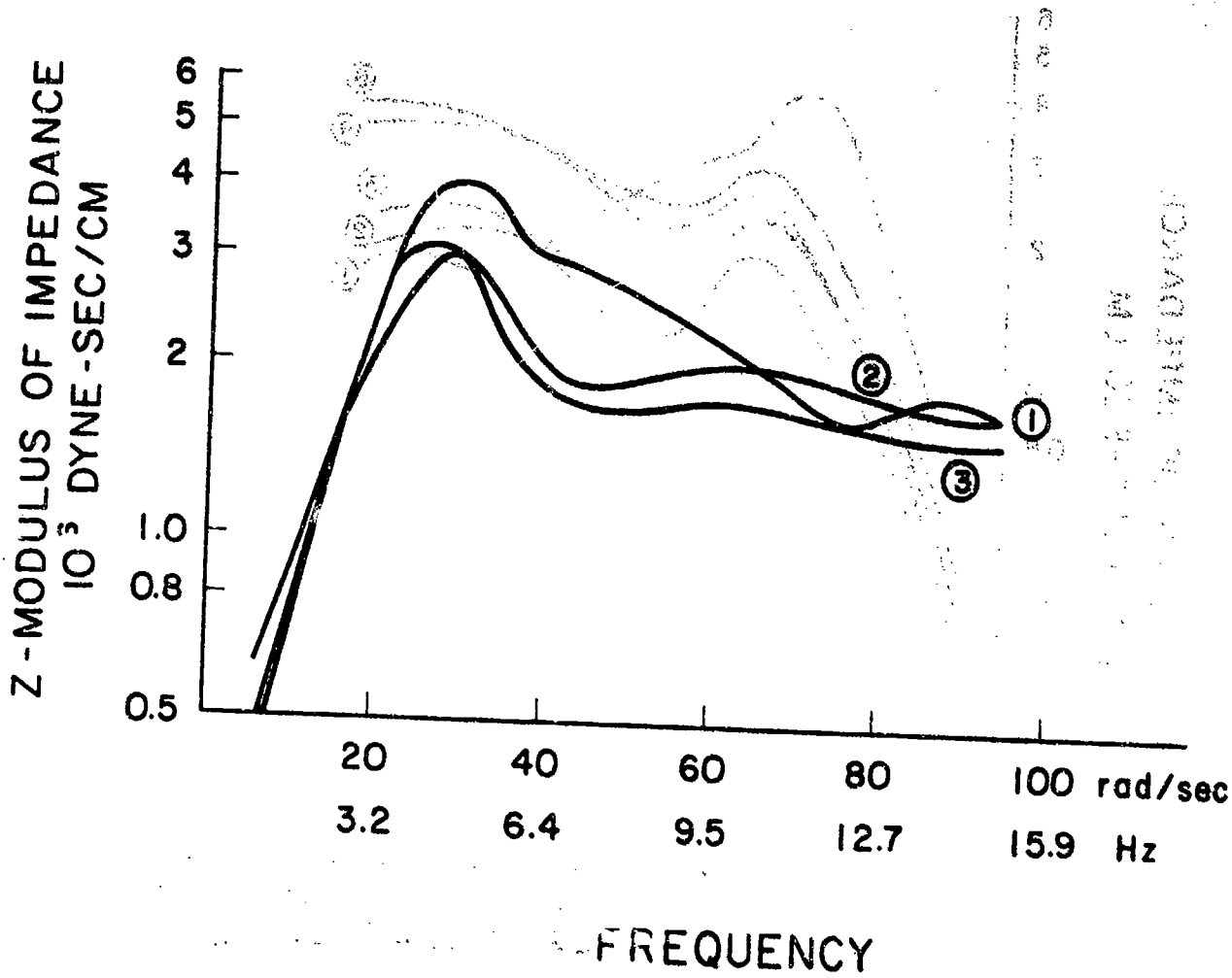

Figure 3.11. Comparison of impedance curves for SSM and ILSV with buttocks: (1) experimental curve of Vogt, et al.; (2) impedance of SSM with buttocks; (3) impedance of ILSV with buttocks.

CHAPTER IV

INJURY POTENTIAL MODEL

IV.1 Injury Potential Function for Cylindrical Vertebral Body Model

A simulation with the spine head model yields as part of the results, the normal force N, and bending moment, M, time histories at each vertebral level. In this Chapter, the evaluation of injury potential as a function of N and M will be considered. We will call this function the Injury Potential Function.

Mathematically, we can express our task as the determination of f, where

$$IPF_j = f(|M_j|, |N_j|, A1_j, A2_j) \tag{4.1}$$

in which IPF_j = injury potential function

$|M_j|$, $|N_j|$ = bending moment and normal force magnitudes when IPF_j is maximum in vertebral body j

$A1_j$, $A2_j$ = parameters representing the failure criteria of vertebral body j.

Belytschko, et al., (1976) discussed an approach for the preliminary evaluation of injury potential. They idealized the vertebral body as a cylindrical shell of radius r_o and height h (see Fig. 4.1). The shell consisted of cortical or compact bone with an interior (vertebral core) of trabecular or soft bone of radius r_i.

For pure axial compression, the stresses in the cortical shell and vertebral core are related by

$$\sigma_i = \sigma_o E_i / E_o \tag{4.2}$$

and equilibrium requires that

$$\sigma_i = (N - \sigma_o A_o)/A_i \tag{4.3}$$

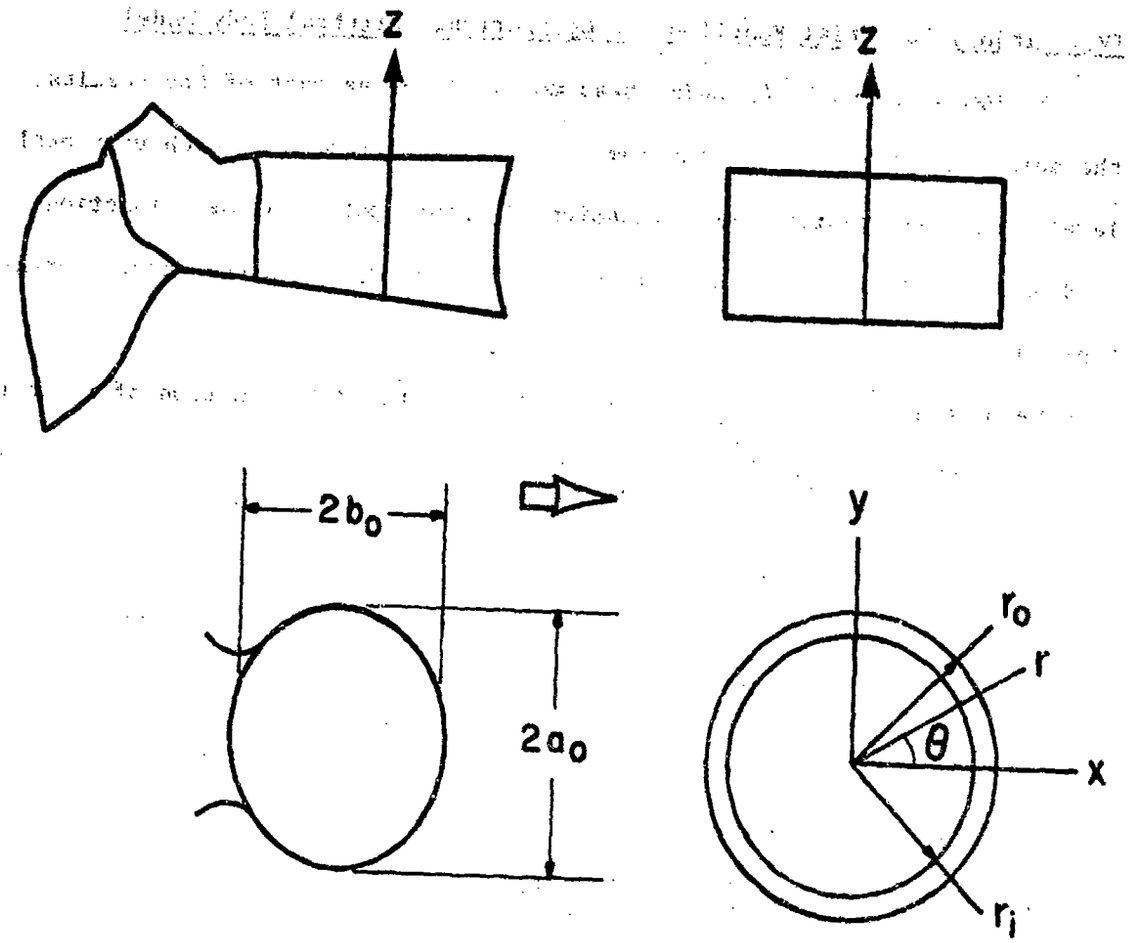

Figure 4.1. Idealization of a vertebral body as a cylindrical shell.

where

σ_i, σ_o = stress in trabecular and cortical bone, respectively

E_i, E_o = Young's modulus in trabecular and cortical bone, respectively

N = applied axial force

A_o = area of cortical shell = $\pi(r_o^2 - r_i^2)$

A_i = area of vertebral core = πr_i^2 .

Eqs. (4.2) and (4.3) yield an expression for the stress in the cortical shell,

$$\sigma_o = \frac{E_o N}{\pi[E_i r_i^2 + E_o(r_o^2 - r_i^2)]} . \tag{4.4}$$

From a compression test, we can obtain an axial force, N_{max}, which is the maximum axial force that can be sustained by a vertebra. The corresponding stress, as given by Eq. (4.4), is then the maximum safe stress for the cortical bone.

Once σ_o^{max} has been determined, we can use it to obtain M_{max}, the moment which would produce a stress σ_o^{max} in the cortical shell. The flexure formula from simple beam theory results in the relationship

$$\sigma_o = \frac{4Mr_o E_o}{\pi[E_i r_i^4 + E_o(r_o^4 - r_i^4)]} , \tag{4.5}$$

from which

$$M_{max} = \frac{\pi[E_i r_i^4 + E_o(r_o^4 - r_i^4)]\,\sigma_o^{max}}{4r_o E_o} . \tag{4.6}$$

For combined bending and axial loading, σ_o^{max} is given by the superposition of Eqs. (4.4) and (4.5),

$$\sigma_o = \frac{E_o N}{\pi[E_i r_i^2 + E_o(r_o^2 - r_i^2)]} + \frac{4Mr_o E_o}{\pi[E_i r_i^4 + E_o(r_o^4 - r_i^4)]} \tag{4.7}$$

so N and M satisfy the relationship

$$\frac{N}{N_{max}} + \frac{M}{M_{max}} = 1 \ . \tag{4.8}$$

The above formulation lends itself directly to an injury potential criterion,

$$IPF = \frac{|M_j|}{A1_j} + \frac{|N_j|}{A2_j} < 1 \tag{4.9}$$

where $|M_j|$ and $|N_j|$ are as defined in Eq. (4.1), and

j = vertebral level

$A1_j$ = maximum bending moment in pure bending

$A2_j$ = maximum compression force in pure compression.

Eq. (4.9) was developed by considering the stresses in the vertebral body's cortical shell. No direct attention was given to the stresses in the vertebral core. The elastic modulus of the vertebral core is several orders of magnitude lower than that of the cortical shell. Hence, the stresses will be several orders of magnitude larger in the cortical shell even under pure axial loading. When we consider bending stresses also, this disparity becomes even greater. It is this large difference in cortical shell and vertebral core stresses, particularly under the combined action of bending and axial loading, which justifies the use of the cortical shell stress as the basis for the injury potential criteria.

Eq. (4.9) is essentially the same relationship used by Belytschko, et al., (1976) in their preliminary evaluation of injury potential. However, rather than determining the maximum of IPF_j for the entire time history, they used the individual maximums of $|M_j|$ and $|N_j|$ to determine IPF_j. This leads to larger values of IPF_j.

Before the injury potential function, Eq. (4.9), can be put to use, it is necessary to obtain values for the vertebral material properties and geometries.

IV.2 Compressive Strength of Vertebrae

Payne (1972) examined the work of Geerts (1946) in which the breaking loads of vertebrae T8 through L5 were determined for subjects varying in age from 19 to 46. These are reproduced in Table 4.1. Also included in Table 4.1 are three values of breaking strengths (T8, T12, L2, L1) determined by Crocker and Higgins (1966). The average lumbar vertebral breaking load of the vertebrae listed in this table is 9.28×10^8 dynes (2090 lbs.). Brown, et al., (1957) reported an ultimate compressive load varying from 4.45×10^8 to 5.80×10^8 dynes (1000 to 1300 lbs.) for 5 lumbar vertebrae taken from three measurements. Perey (1957) reports an average value of 5.88×10^8 dynes (1320 lbs.) for the lumbar vertebral breaking load. Payne, however, comments that Perey's failure to "true-up" his vertebrae to insure for uniform transmission of the load from the testing apparatus to the specimen resulted in induced stresses higher than for pure uniform compression, thus resulting in a lower apparent breaking load.

Rockoff, et al., (1969) determined the maximum non-destructive compressive strengths (elastic limit) of 50 lumbar vertebrae from the spines of 32 fresh cadavers. The subjects included both males and females and spanned an approximate age range of 20 to 80 years. Rockoff reports that all of the specimens from subjects of age less than 40 years had strengths greater than 800 psi (5.52×10^7 dyne/cm^2) while essentially all of the specimens greater than 40 years had strengths less than 800 psi. If we assume this is the average strength of the specimens and assume a lumbar vertebral body cross-sectional area of 16.51 cm^2 (from Payne), we obtain an average elastic limit load of 9.11×10^8 dynes (2050 lbs). Rockoff also considers the relative elastic limit strength contribution of the vertebral cortex and the trabecular bone, and the variation of the elastic limit with the ash content or physical density

Table 4.1. Breaking loads of vertebrae T8 through L5 as determined by Geertz, and Crocker and Higgins, reported by Payne

Age (Years) Geertz	Breaking Load in Dynes x 10^8									
	T8	T9	T10	T11	T12	L1	L2	L3	L4	L5
19				7.4		7.1		8.8		
21	6.3		7.8		8.8		9.7			10.0
21				7.1	6.8	8.2				
23	5.3	6.0								
33			6.5		7.8		7.8		10.8	
36	5.9	7.1	7.5							
38					7.8		8.1		8.8	
43		6.9		8.4		8.8		9.2		9.8
			7.2			7.8			9.3	
46				7.4		7.8		10.8		11.8
Crocker and Higgins										
40					9.5	11.0				
47	5.3									
Mean[1]	5.8	6.7	7.3	7.6	7.8	7.9	8.5	9.6	9.6	10.5
Mean[1] for lumbar vertebrae						9.2				

[1] Geertz data only

of the trabecular bone. He found that the cortex generally contributes 45 to 75% of the vertebral body strength regardless of the ash content of the trabecular bone.

These sources as well as several others indicate that the upper limit of lumbar vertebral breaking strength is approximately 1.0×10^9 dynes (2250 lbs.). Although Rockoff reported that his strengths were elastic limit loads, it appears that the load deflection curves for vertebra are essentially linear up to the point of failure. Since the elastic limit is defined as the point at which the load-deflection curve deviates from linearity, it is quite close to the breaking strength.

IV.3 Elastic Moduli of the Vertebral Cortex and the Trabecular Bone

Data for the elastic modulus of the vertebral cortex could not be found in the literature. However, several investigators have reported elastic moduli of cortical bone from other bones. McElhaney (1966) reported a value of 1.52×10^{11} dyne/cm^2 (2.2×10^6 psi) for the elastic modulus of compact bone from an embalmed human femur. Evans (1970) reports values of 1.45×10^{11}, 1.59×10^{11} and 1.74×10^{11} dyne/cm^2 (2.1×10^6, 2.51×10^6 and 2.52×10^6 psi) for the elastic moduli of compact bone from a wet embalmed adult femur, tibia, and fibula respectively. Yamada (1970) obtained a mean value of 1.04×10^{11} dyne/cm^2 (1.51×10^6 psi) for the elastic modulus of wet femoral compact bone of people 20 - 39 years of age. He also reports a value of 8.82×10^8 dyne/cm^2 (1.28×10^4 psi) for the elastic modulus of wet trabecular bone from human lumbar vertebrae.

IV.4 Vertebral Geometric Properties

Belytschko, et al., based the equivalent radii of the vertebral bodies on Lanier's (1939) mean values of the transverse and sagittal diameters. If we assume an elliptical vertebral body cross-section and the transverse and

sagittal diameters are given by $2a_{oj}$ and $2b_{oj}$ (vertebral level j) then the equivalent radius is $r_j = \sqrt{a_{oj} b_{oj}}$.

The value which Belytschko, et al., used for the vertebral cortical bone thickness, 0.3 mm, was based on Kulak (1974). Kulak measured the cortical bone thickness of sectioned vertebrae by viewing them under a microscope through a measuring eyepiece. These vertebrae were obtained from the lumbar region of five subjects. The mean value obtained was 0.32 mm. It is possible that the cortical shell thicknesses of vertebrae in the thoracic region are less than 0.3 mm, but since these values have not been reported in the literature to the authors' knowledge, the assumption of a constant vertebral cortical shell thickness of 0.3 mm for all vertebral levels will be used.

IV.5 Failure Criteria for the Injury Potential Function

Table 4.2 lists the values of experimental axial compression failure loads used by Belytschko, et al. They evidently based their values for T8 through L-5 primarily on the work of Geertz (1946). The values for T1 through T7 are based on the assumption that the vertebral cross-sectional area; and hence breaking strength, decreases linearly with vertebral level. This is very close to true for levels T8 through L5.

For the elastic moduli of the vertebral cortex and trabecular bone, they cite values from Evans of 1.5×10^{11} and 7.35×10^{8} dyne/cm^2 respectively (2.18×10^{6} and 1.07×10^{4} psi) which appear to be in reasonable agreement with those found by other investigators.

Comparing the parameters (breaking strength, elastic moduli, etc.) which Belytschko, et al. used in their evaluation of injury potential, with those discussed in the previous section, it is apparent that the failure criteria

Table 4.2. Maximum axial compression for pure compression (A2) and maximum bending moment for pure bending (A1) used by Belytschko, et al., in their preliminary evaluation of injury potential

Vertebral Level	r_o (1)	A2 (3)	A1 (2)	$(\sigma_o)_{max}$ (4)
L5	2.165	10.29	10.19	2.18
L4	2.203	9.80	9.87	2.03
L3	2.154	9.31	9.18	1.98
L2	2.078	8.82	8.40	1.95
L1	2.019	8.33	7.72	1.91
T12	1.972	7.84	7.11	1.84
T11	1.883	7.35	6.37	1.82
T10	1.7181	6.86	5.64	1.81
T9	1.690	6.37	4.98	1.78
T8	1.619	5.88	4.41	1.73
T7	1.538	5.58	3.98	1.74
T6	1.437	5.29	3.53	1.78
T5	1.388	4.90	3.16	1.71
T4	1.323	4.60	2.84	1.69
T3	1.271	4.21	2.49	1.62
T2	1.226	3.92	2.24	1.57
T1	1.162	3.62	1.96	1.54

(1) Equivalent radius (cm)

(2) Maximum bending moment for pure compression (dyne/cm x 10^8) computed from Eq. 4.6

(3) Experimentally determined compressive breaking load (dyne x 10^8) from Geertz, reported by Payne

(4) Maximum vertebral cortex stress (dyne/cm^2 x 10^9) from Eq. 4.4

(maximum axial compression load and maximum bending moment) computed from these parameters is acceptable within the range of accuracy permitted by the available data. Consequently, the present injury potential study incorporated identical parameters in the development of the injury potential function described in Section IV.1.

This injury potential analysis has been incorporated as part of the head spine simulation program as follows. During each step of the time integration process, the axial force N and the two moments M_y and M_z are obtained for each vertebral level j. Since the program treats the vertebrae as rigid bodies and the discs as deformable elements, the axial force and moments are not directly available, so the vertebral forces at level j are considered as the average of the forces in the discs above and below the vertebral body; i.e.

$$
\begin{aligned}
M_y &= \tfrac{1}{2}(\hat{m}_{yI} + \hat{m}_{yK}) \\
N &= \tfrac{1}{2}(\hat{f}_{xI} + \hat{f}_{xK}) \\
M_z &= \tfrac{1}{2}(\hat{m}_{zI} + \hat{m}_{zK})
\end{aligned}
\tag{4.10}
$$

where I and K are the secondary nodes at the top and bottom of the vertebral body j. Although the local $\hat{x}$ axes of the disc above and below the vertebral body may differ slightly in orientation, this has been neglected. The local $\hat{y}$ and $\hat{z}$ directions in each disc correspond to the moments in the frontal and sagittal planes, respectively.

The injury potential function is then evaluated for both moments

$$
\begin{aligned}
IPF_1 &= \frac{|N|}{\overline{A1}_j} + \frac{|M_y|}{\overline{A2}_j} \\
IPF_2 &= \frac{|N|}{\overline{A1}_j} + \frac{|M_z|}{\overline{A2}_j} \quad .
\end{aligned}
\tag{4.11}
$$

If either of these values exceeds the previous maximum for level j, it is stored.

At the end of the simulation, the maximum values of the injury potential functions encountered are printed out in graphical form. Since Eq. (4.11) normalizes IPF relative to 1.0 for each vertebral level, the values of IPF indicate the likelihood of injury at each level. If IPF is much smaller than 1.0 at a level, injury is very unlikely whereas values of IPF in the neighborhood of 1.0 or greater than 1.0 indicate that vertebral failure is likely at that level.

In order to interpret the likelihood of injury in a statistical sense, the normal distributions as fit by Payne (1972) to the data of Geertz, Crocker and Higgins and Nachemson were used to obtain standard deviations. These lead to probabilities of failure as shown in Fig. 6.20.

The extension of this post-processor to other modes of motion segment failure will only involve the development of additional injury potential functions. Thus, to consider vertebral dislocations, it is only necessary to develop a function and appropriate injury thresholds associated with dislocations. As part of the function development, the mechanism of failure and causative forces must be determined. This procedure is currently under study under a separate contract by the AMRL.

CHAPTER V

PRIMATE HEAD-SPINE MODELS

Because of the difficulty of obtaining experimental results for human subjects, data were obtained and prepared for similar models of primates. The goal of this effort is to compare the predictions of model simulations of nonhuman primates with experiments in order to validate the basic modeling concepts. In addition, it is hoped that such studies will shed further light on the procedures of scaling results from nonhuman primates to humans.

In this investigation, preliminary model data was prepared for the following primates:

1. chimpanzee;
2. baboon;
3. rhesus monkey.

We will here describe the sources of this data, how it was processed, and give some results for the models. In addition, we will list some of the major data needed to lay a sounder groundwork for these models; it is interesting to observe that while data is much easier to procure for nonhumans, much less is reported in the literature.

V.I Chimpanzee

Geometric data for the chimpanzee spine was based on Kazarian, et al., (1976), who provided the vertebral body heights, intervertebral disc heights and endplate areas, and figures of a chimpanzee spine. These figures were digitized to provide the geometric data for the model. Since only the areas of endplates were given, a circular cross-section was assumed and the radius was computed. The model structure is shown in Fig. 5.1.

The mass data for the chimpanzee was determined on the basis of measurements reported by Rholes and Fineg (1961), for two groups of chimps: one group

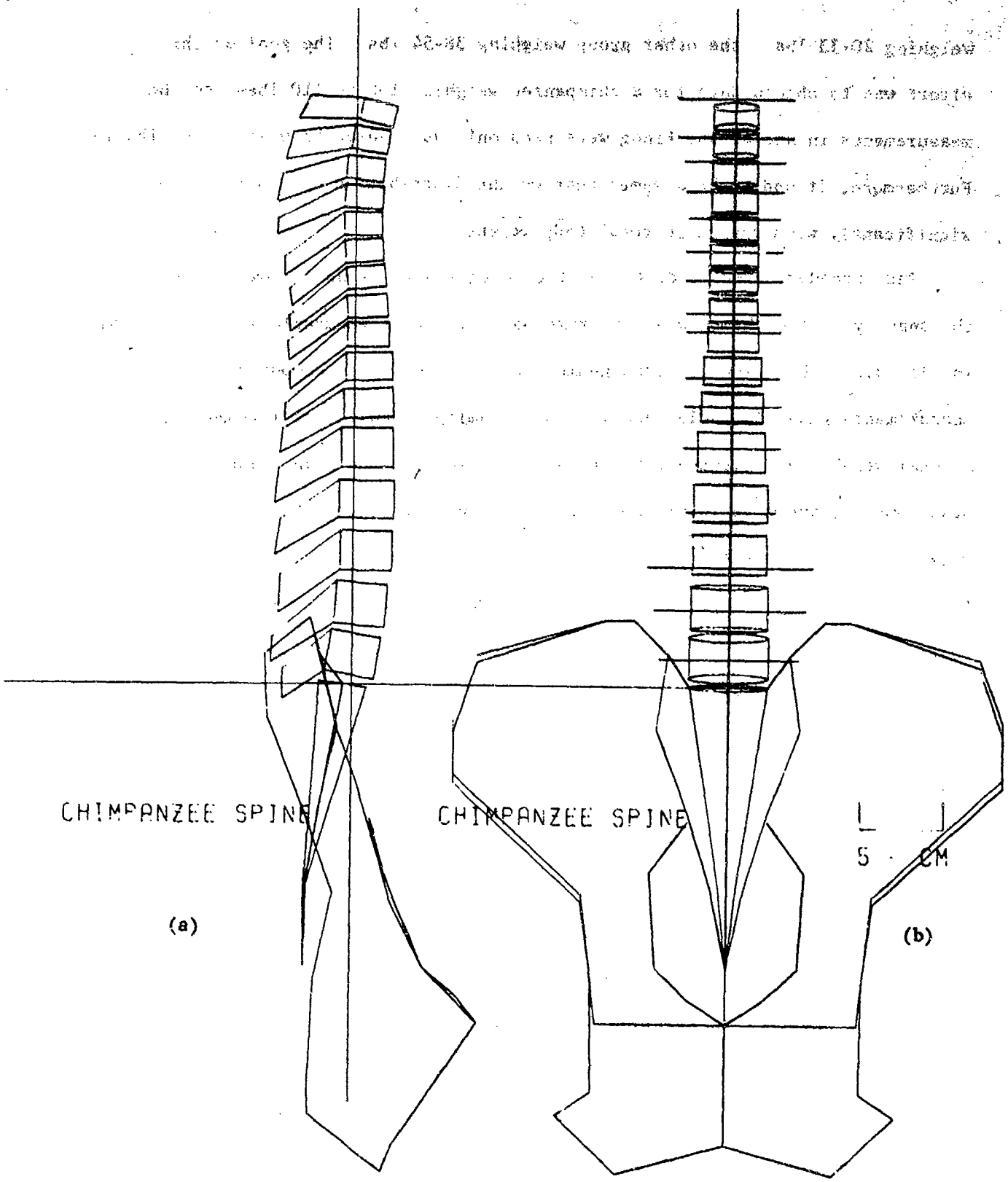

Figure 5.1. Chimpanzee spine model: (a) sagittal plane view (b) frontal plane view

weighing 20-33 lbs., the other group weighing 38-54 lbs. The goal of this effort was to obtain data for a chimpanzee weighing 100 to 110 lbs., so the measurements in Rholes and Fineg were used only as a guide to weight distribution. Furthermore, it had to be assumed that weight distribution does not change significantly with change in total body weight.

The procedure used to determine the model masses is as follows. First the anatomy of the chimps was approximated by a set of geometric solids as shown in Fig. 5.2. The volume of each geometric figure was then computed using the measurements given in Rholes and Fineg, assuming a density of 1 gram/cm^3. A total weight was computed for the maximum, minimum, and mean values of these measurements, and a ratio of the weight of each part of the anatomy to the total weight. These ratios are given in Table 5.1. As can be seen, except for a few discrepancies, the proportion between total weight and the weight of a portion of the anatomy is somewhat independent of the total weight, so that these ratios can be used to estimate the weight of the anatomical segments.

Next, it was established that for the torso, the ratio of the width of the torso to the height of the torso is reasonably independent of the total weight. By using a ratio of width of to height of chest of 1.18 as determined from the measurements given in Rholes and Fineg, the torsal height of the chimp for which a skeletal figure was provided by Kazarian (1976) was estimated.

Then using these dimensions and the geometry of the torso as depicted in Fig. 5.3 (provided by Kazarian (1976)), the weight of the torso segments from T1 to L4 were determined. Also, the total weight of the chimpanzee for which the skeletal figure was provided was estimated and was found to be 111 lbs.

To determine the mass of each vertebral segment of the torso, it was necessary to know the cross-sectional area of the torso and the thickness at each level. The thickness of each level was based on the vertebral body heights

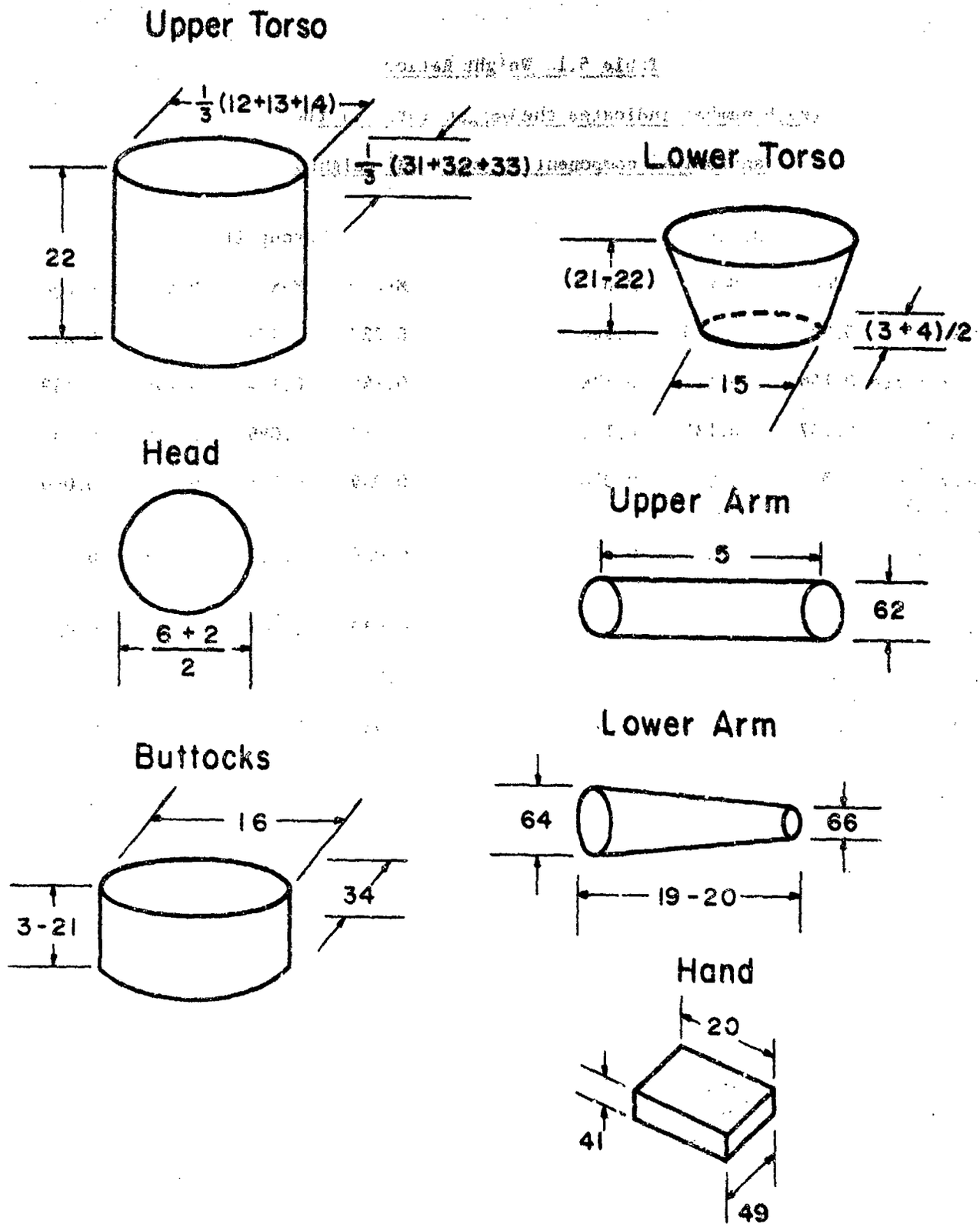

Figure 5.2. Idealizations of anatomical components of chimpanzee into geometric solids; numbered measurements refer to Rholes and Fineg (1961).

Table 5.1 Weight Ratios

(each number indicates the weight ratio of the anatomical component to the total weight)

	Group I			Group II			
	Med	Max	Min	Med	Max	Min	Average
Chest	0.235	0.230	0.264	0.227	0.177	0.237	0.228
Lower torso	0.166	0.122	0.126	0.145	0.134	0.146	0.143
Head	0.137	0.135	0.171	0.112	0.096	0.138	0.132
Upper arm (each)	0.033	0.042	0.040	0.039	0.041	0.047	0.040
Lower arm (each)	0.025	0.020	0.007	0.026	0.023	0.036	0.023
Hand (each)	0.018	0.042	0.007	0.030	0.067	0.011	0.029
Buttocks	0.076	0.060	0.037	0.058	0.082	0.055	0.066
Upper leg (each)	0.076	0.071	0.079	0.082	0.071	0.073	0.075
Lower leg (each)	0.025	0.022	0.033	0.026	0.022	0.036	0.027
Foot (each)	0.014	0.029	0.013	0.026	0.033	0.015	0.022

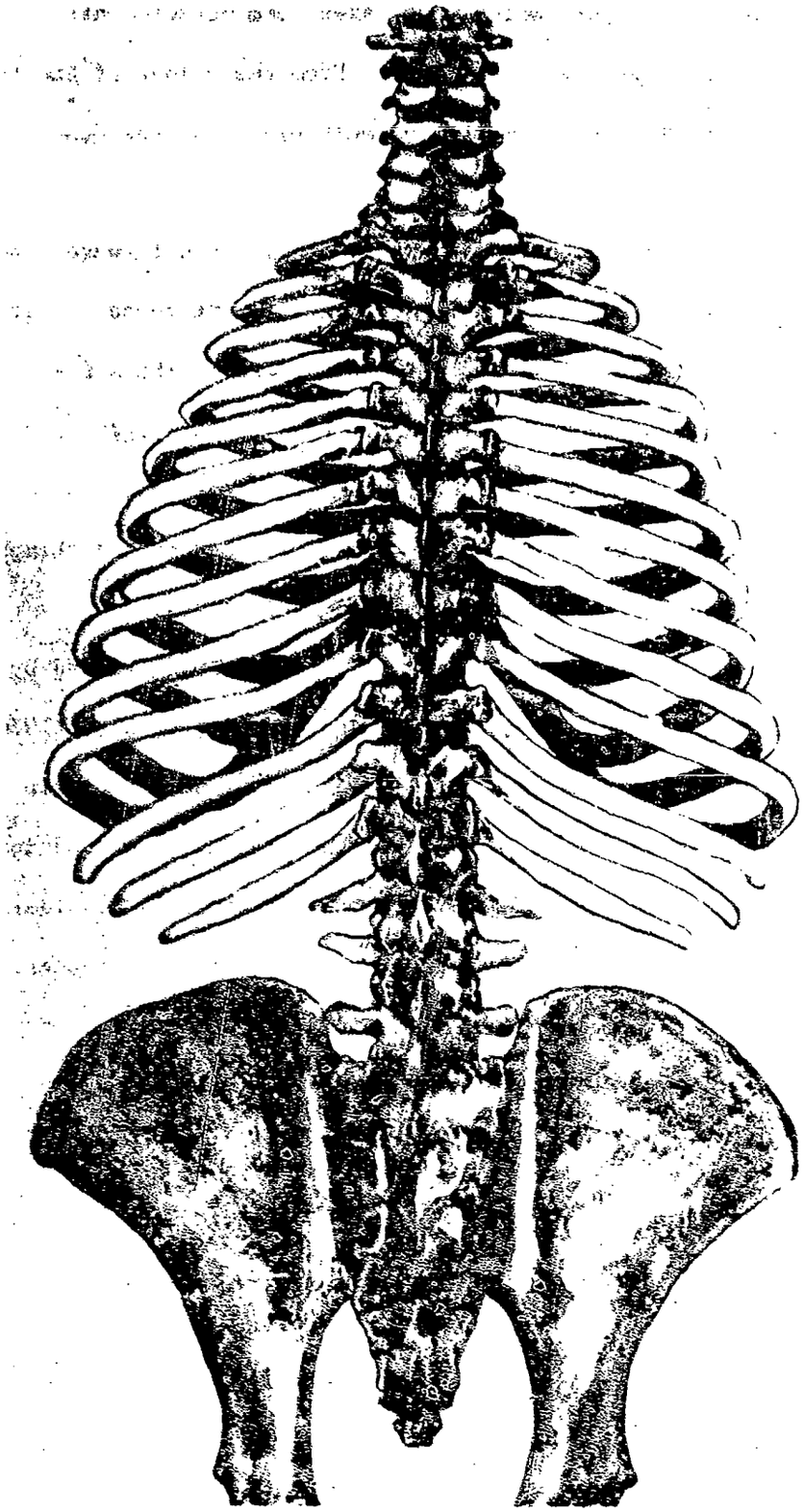

Figure 5.3. Chimpanzee torso geometry from Kazarian (1976).

and intervertebral disc heights which were taken from measurements of the skeletal figure. The area was found from Figure 5.2. From the volume of the torso at a vertebral level, the mass was computed by multiplying by the density of 1 gram/cm^3.

The equations for the moments of inertia, I_x, I_y, and I_z were derived on the basis of elliptical cross sections. The results were compared with the masses of the vertebral levels of the human spine used in the Air Force model. The masses of the human spine were between 1.2 to 2 times larger than that for the chimp. The human anatomy considered in the Air Force model has a total weight of 169 lbs., which is approximately 1.6 times that of the chimpanzee. The masses and moments of inertias are given in Table 5.2.

The stiffness data for the intervertebral discs was determined by using the procedures of Belytschko, et al., (1974) and Schultz, et al., (1974). In these procedures, it is assumed that the level-to-level variations in intervertebral disc stiffnesses depend directly on the geometries of the intervertebral discs and can be deduced from strength of materials considerations. Furthermore, since no disc stiffnesses were available for chimpanzees, the material properties were assumed to be identical to human discs. The axial, bending and torsional stiffnesses at a level J are given by

$$\begin{aligned} (\text{axial stiffness})_J &= R_1 A_J \\ (\text{bending stiffness})_J &= R_2 K_J^B \\ (\text{torsional stiffness})_J &= R_3 K_J^T \end{aligned} \tag{5.1}$$

where

$$\begin{aligned} A_J &= \frac{r_o^2 - r_i^2}{IDH} \\ K_J^B &= \frac{0.5}{IDH}\left(r_o^4 - r_i^4\right) \\ K_J^T &= 2\, K_J^B \end{aligned} \tag{5.2}$$

Table 5.2a

Masses and Moments of Inertia of Torso Sections

	Major radius a(cm)	Minor radius b(cm)	Height of section h(cm)	Mass m(gm)	Moments of Inertia I_{xx}(gm-cm^2)	I_{yy}(gm-cm^2)	I_{zz}(gm-cm^2)
T1	14.35	10.3	1.43	680	18000	35000	52800
T2	14.35	10.3	1.61	760	20400	39400	59500
T3	14.35	10.3	1.61	760	20400	39400	59500
T4	14.35	10.3	1.55	730	19600	38000	57000
T5	14.35	10.3	1.55	730	19600	38000	57000
T6	14.35	10.3	1.61	760	20400	39400	59500
T7	14.35	10.3	1.55	730	19600	38000	57000
T8	14.35	10.3	1.55	730	19600	38000	57000
T9	14.35	10.3	1.67	790	21000	41000	61600
T10	14.35	10.3	1.90	900	24000	46500	70000
T11	14.35	10.3	2.14	1000	27300	52500	79000
T12	14.35	10.3	2.86	1350	36800	70600	10600
L1	14.35	10.3	2.86	1350	36800	70600	10600
L2	13.66	9.67	2.86	1200	29000	57000	85000
L3	12.97	9.00	2.97	1100	23300	47500	69000
L4	12.29	8.35	2.74	900	16000	34500	50000

Note: $\frac{b^2}{3} << a^2, b^2$ so h does not have much of an effect of I when elliptical cylinder is a thin disc.

$$I_{xx} = \frac{m}{4}(b^2 + \frac{h^2}{3}) \qquad I_{zz} = m(\frac{a^2}{4} + \frac{b^2}{4}) \qquad \text{where } m = \rho\pi abh$$

Table 5.2b. Inertial data for vertebral levels L4-T11 for chimpanzee with viscera model

Level	$m^{(2)}$	$I_{\bar{x}}^{(3)}$	$I_{\bar{y}}^{(3)}$	$I_{\bar{z}}^{(3)}$
	Visceral mass data		L4-T11	
L4	6.690	1.150	3.215	4.281
L3	8.870	2.042	4.483	6.394
L2	10.030	2.581	5.431	7.874
L1	11.570	3.214	6.785	9.841
T12	10.820	2.782	6.340	8.975
T11	8.100	1.855	4.722	6.515
	Vertebral mass data		L4-T11	
L4	2.310	0.128	0.239	0.338
L3	2.230	0.091	0.267	0.325
L2	2.060	0.057	0.292	0.331
L1	1.960	0.060	0.273	0.306
T12	2.710	0.081	0.717	0.762
T11	2.030	0.055	0.531	0.571

(1) Inertial data for torso segments T10-L3 is given in Table 5.2a

(2) Translational mass - grams x 10^2

(3) Rotational masses about body coordinates $\bar{x}$, $\bar{y}$, $\bar{z}$ gm·cm^2 x 10^4

where r_i and r_o are the inside and outside radii of the annulus fibrosis, and IDH is the intervertebral disc height. Eqs. (5.2) follow from elementary strength of materials treatment of the stiffness of a disc. It was assumed that $r_i = 0.75\ r_o$.

The geometric factors of the chimp spine were based on data provided by Kazarian. We assumed that the R_1, R_2, and R_3 for chimpanzees and humans were the same, i.e. that material properties of the two species are similar. These constants were then determined in the following manner. In Table 1 of Belytschko, et al., (1974), geometric data at intervertebral levels L2/L3, T12/L1, T10/T11, and T8/T9 were given. From this data A, K^B and K^T for those levels were calculated.

Table 2 of Schultz, et al. gives stiffnesses at L2/L3, T12/L1, T10/T11, and T8/T9. Ratios were set up for corresponding quantities at the corresponding levels and the constants R_1, R_2 and R_3 were determined using the average of the four levels (corresponding values at all four levels deviated little from the respective averages). The values are

$$R_1 = 0.144 \times 10^9 \text{ dynes/cm}^2$$

$$R_2 = 0.746 \times 10^8 \text{ dynes/cm}^2 \qquad (5.3)$$

$$R_3 = 1.27 \times 10^8 \text{ dynes/cm}^2$$

The geometric data (A, K^T, K^B) for the chimp appears in Table 5.3 while the stiffnesses for the chimp spine model appear in Table 5.4.

It should be noted that there were discrepancies between the tabulated geometry (used in obtaining the stiffnesses) and the geomtrey of the chimpanzee skeletal figure. The reasons for this are:

1) IDH for the given data is larger than the IDH measured from the chimp's skeletal figure. There is about a 50% discrepancy.

Table 5.3

Geometries of Chimpanzee Intervertebral Discs

Level	IDH(cm)	Area(cm^2),A	r_o(cm)	r_i(cm)	K^B(cm^3)	K^T(cm^3)
C3	0.42	2.94	0.97	0.73	0.72	1.43
C4	0.42	2.87	0.96	0.72	0.69	1.38
C5	0.42	2.89	0.96	0.72	0.69	1.38
C6	0.43	2.66	0.92	0.69	0.57	1.14
C7	0.40	2.74	0.93	0.70	0.64	1.27
T1	0.71	3.10	0.99	0.74	0.47	0.93
T2	0.73	3.28	1.02	0.77	0.50	1.00
T3	0.74	3.37	1.04	0.78	0.54	1.08
T4	0.74	3.64	1.08	0.81	0.63	1.26
T5	0.74	3.43	1.04	0.78	0.54	1.08
T6	0.70	4.86	1.24	0.93	1.16	2.31
T7	0.94	4.31	1.17	0.88	0.68	1.35
T8	0.94	4.22	1.16	0.87	0.66	1.32
T9	0.95	5.05	1.27	0.95	0.94	1.88
T10	1.00	5.73	1.35	1.01	1.14	2.28
T11	1.00	5.97	1.38	1.04	1.23	2.46
T12	1.20	6.44	1.43	1.07	1.20	2.39
L1	1.30	7.29	1.52	1.14	1.41	2.81
L2	1.40	8.05	1.60	1.20	1.60	3.20
L3	1.20	8.10	1.61	1.21	1.92	3.81
L4	1.40	9.43	1.73	1.30	2.18	4.36

where IDH, Area are given

$$r_o = \sqrt{\frac{\text{Area}}{\pi}} \qquad K^B = \frac{1}{2\text{IDH}} (r_o^4 - r_i^4)$$

$$K^T = \frac{1}{\text{IDH}} (r_o^4 - r_i^4)$$

$$r_i = \frac{3}{4} r_o$$

Table 5.4
Chimpanzee Stiffness Data

Level[1]	Intervertebral Discs Axial (dyne/cm x 10^9)	Intervertebral Discs Bending (dyne-cm/rad x 10^8)	Intervertebral Discs Torsional (dyne-cm/rad x 10^8)	Visceral[2] Elements Axial (dyne/cm x 10^7)
C3	0.42	1.07	0.91	
C4	0.41	1.03	0.88	
C5	0.42	1.03	0.88	
C6	0.38	0.85	0.72	
C7	0.39	0.95	0.81	
T1	0.45	0.69	0.60	
T2	0.47	0.75	0.64	
T3	0.49	0.81	0.69	
T4	0.52	0.94	0.80	
T5	0.49	0.81	0.69	
T6	0.70	1.72[3]	1.47[3]	
T7	0.62	1.01	0.86	
T8	0.51	0.98	0.84	
T9	0.73	1.40	1.19	
T10	0.83	1.71	1.45	2.20
T11	0.86	1.84	1.56	1.81
T12	0.93	1.78	1.52	1.55
L1	1.05	2.10	1.79	1.55
L2	1.16	2.39	2.03	1.29
L3	1.17	2.84	2.44	1.16
L4	1.36	3.25	2.77	0.26

(1) Refers to element below designated vertebral level

(2) Visceral elements are located between the pelvis and T10. Stiffnesses of all viscera/spine interconnecting elements ≈ 1.0 x 10^7 dyne/cm

(3) Though based on data, appears spurious

1 kp ≈ 10^6 dynes

2) Area for the given data is smaller than the area measured from the chimp skeletal figure. There is about a 25% discrepancy.

The chimp stiffnesses in the upper spine are only 0.4 of the human stiffnesses. However, the chimp data lacks the relative maximum stiffness found in humans around T11, but instead increases continuously to L4, where the stiffnesses are comparable to human intervertebral disc stiffnesses.

The visceral bulk modulus was obtained by using Eqs. (4.5) and (4.6) of Belytschko, et al., (1976), using a radius of 12 cm as taken from Table 5.2 and a membrane thickness of 0.5 cm. The resulting stiffnesses are given in Table 5.4.

A modal analysis, an impedance analysis and an ejection analysis of the model of a chimpanzee spine were performed with the ligamentous spine both with and without viscera. Table 5.5 lists the first six axial natural frequencies and the first seven sagittal plane natural frequencies for the chimpanzee isolated ligamentous spine and compares them with the AMRL-TR-76-10 human spine model. Although a casual comparison indicates that the frequencies of the chimpanzee spine in the axial mode are somewhat smaller than those for the model of the human spine, a comparison of the modes (not given) shows that there is a significant difference in the nature of the lower modes between the chimpanzee and the human models. In the chimpanzee, the two lowest axial modes are almost entirely associated with head movement and involve very little deformation of the lower thoracic and lumbar regions, whereas in the human spine model the lowest axial mode involves considerable lower back deformation. Thus the chimpanzee axial mode corresponding to the first human axial mode of 17 Hz is 54 Hz. Thus, as expected, the chimpanzee model modes are significantly higher. Similarly, the first flexural modes of the chimpanzee involve primarily head-neck motion.

TABLE 5.5

Comparison of Natural Frequencies of Human Spine Model (HSM) and Chimpanzee Spine Model (CSM)

Axial Frequencies (Hz)

HSM	CSM
17.09	13.97
32.31	31.81
51.29	53.96
77.22	77.72
100.74	105.22
124.98	131.91

Sagittal Plane Frequencies(Hz)

HSM	CSM	Ratio $\left(\frac{CSM}{HSM}\right)$
1.28	0.76	0.59
3.14	2.04	0.65
5.99	3.70	0.62
9.94	5.32	0.54
13.31	7.24	0.54
16.71	8.55	0.51
18.45	10.30	0.56

This difference between the chimpanzee and human can be directly related to the mass distribution. In the chimpanzee, the ratio of head mass to total mass is quite large compared to the human, whereas the opposite holds for the pelvic mass. It should be noted that these differences in mass in our model are based on rather crude data obtained from gross measurements. However, this difference, while not exactly represented in our model, certainly exists, and it could shed some light on the difficulties in scaling studies; because of the differences in mass distributions, the modal character of the human and chimpanzee are evidently significantly different, thus precluding any simple scaling laws.

An ejection simulation was made with the chimpanzee spine - viscera model. The prescribed acceleration consisted of a peak magnitude of 10g which was reached in 14 msec, with an onset rate of 714g per second. The 10g magnitude was maintained at constant value for the remainder of the simulation. The total duration of the simulation was 40 msec. Figure 5.4 shows the axial force time histories at T9-T10 and T3-T4.

Impedance curves were obtained for the two column chimpanzee model. These are shown in Fig. 5.5.

We would again like to stress the large number of extrapolations that were necessary in obtaining the 100 lb. chimpanzee model. Any additional data would be of great value. Some suggested data are:

a) axial stiffness at any level for a chimpanzee cadaver motion segment (it would be useful to have the size or weight of the chimp corresponding to this stiffness);

b) any other disc stiffness, e.g. bending;

c) a series of photographs or x-rays of a 100 lb chimp to verify our size scaling procedures.

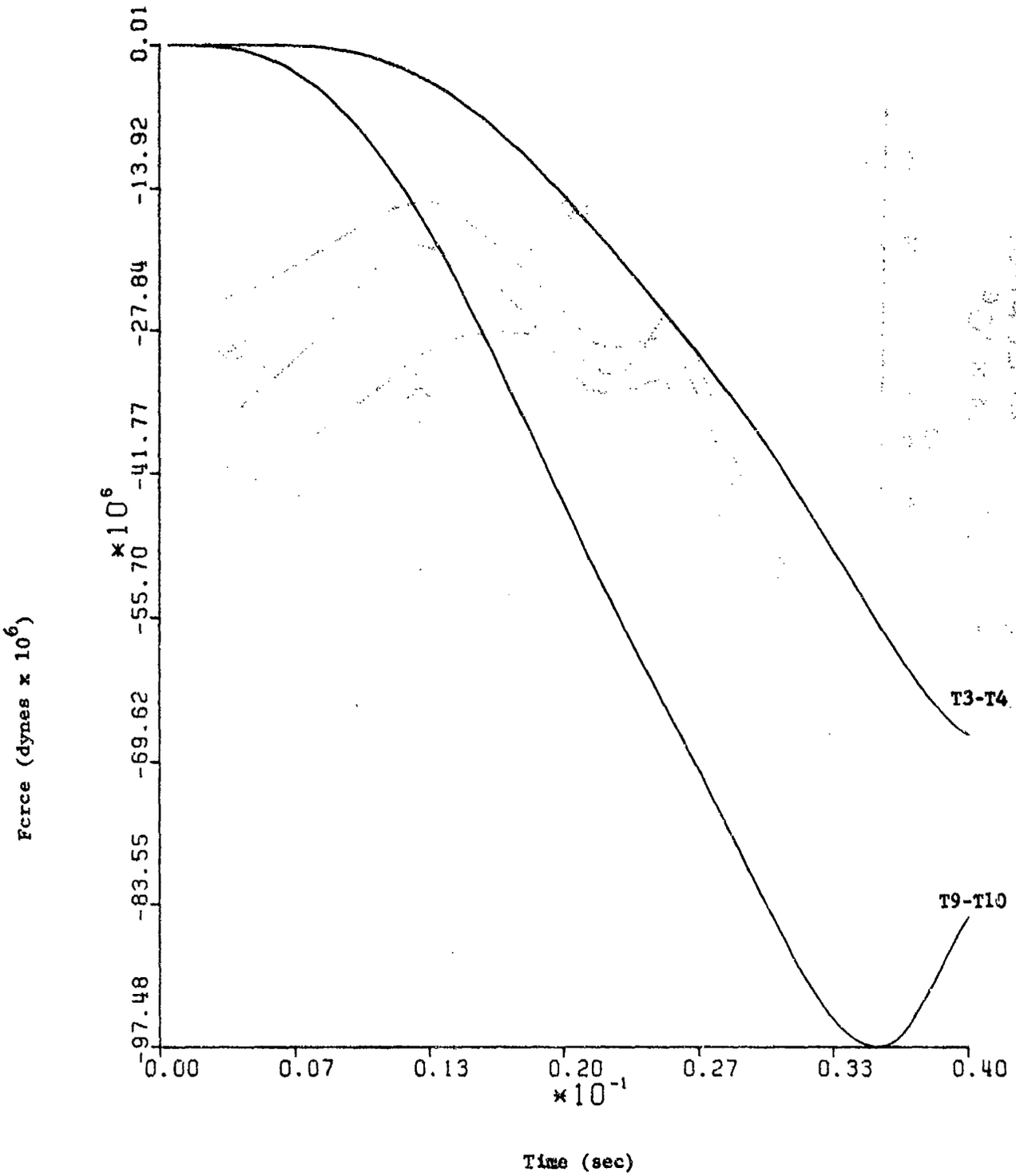

Figure 5.4. Axial force response in the T3-T4 and T9-T10 discs from ejection of chimpanzee model.

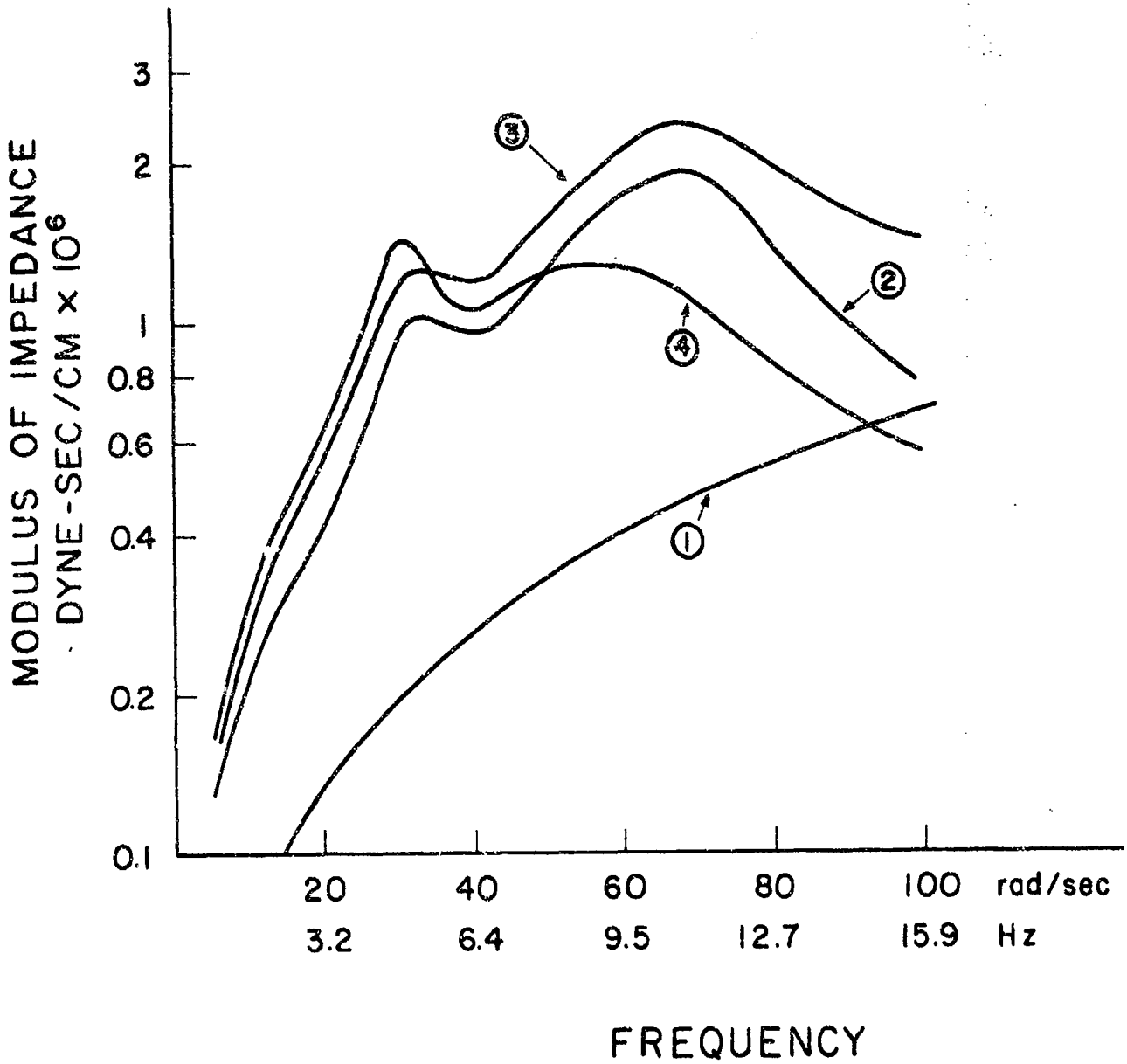

Figure 5.5 Impedance of chimpanzee model with viscera: (1) pelvic mass impedance; (2) impedance of chimpanzee without pelvic mass; (3) impedance of chimpanzee with pelvic mass; (4) impedance of chimpanzee with buttocks. Buttock stiffness is 6.55×10^7 dyne/cm.

V.2 Baboon

The geometrical data of the baboon was obtained in the same manner as that of the chimpanzee, based on data of Kazarian (1976). The resulting model geometry is plotted in Fig. 5.6.

Mass data is based on Reynolds (1974), who measured the inertial properties of anatomical segments of four frozen cadaver baboons. The baboons ranged in mass from 10.8 kg to 12.66 kg. It is of interest to observe that the densities were also measured by Reynolds (p. 73); they ranged from a low of 0.98 gm/cm^3 in the torso to a high of 1.12 gm/cm^3 in the feet and hands, with an average of 1.016 gm/cm^3. Thus the density assumptions made in determining the chimpanzee inertias are quite reasonable: the major sources of error would probably be the idealizations of anatomical segment volumes and the extrapolations. The torso percentage of total volume in the baboon is higher than our estimated percentage for the chimpanzee (53% vs 44%) and the head is lower (8.3% vs 13.2%).

The head mass and moments of inertia were taken directly from the measurements of Reynolds. Since Reynolds did not segment the torso, the inertial properties of the torso segments were obtained by using the data of Kazarian for vertebral body and intervertebral disc heights, a radius of 7.35 cm and the density given by Reynolds. The inertia data is given in Table 5.6.

Stiffness data was constructed using the measurements of Kazarian (1976), Eqs. (5.1) and (5.2), and the R_i factors from human motion segments. This data is given in Table 5.7. No separate visceral column is included.

The impedance of the baboon model is shown in Fig. 5.7. It should be noted that here reliable mass data is available for the head, yet the model exhibits a substantially different impedance curve from the human model, indicating again a potential source of difficulty in scaling.

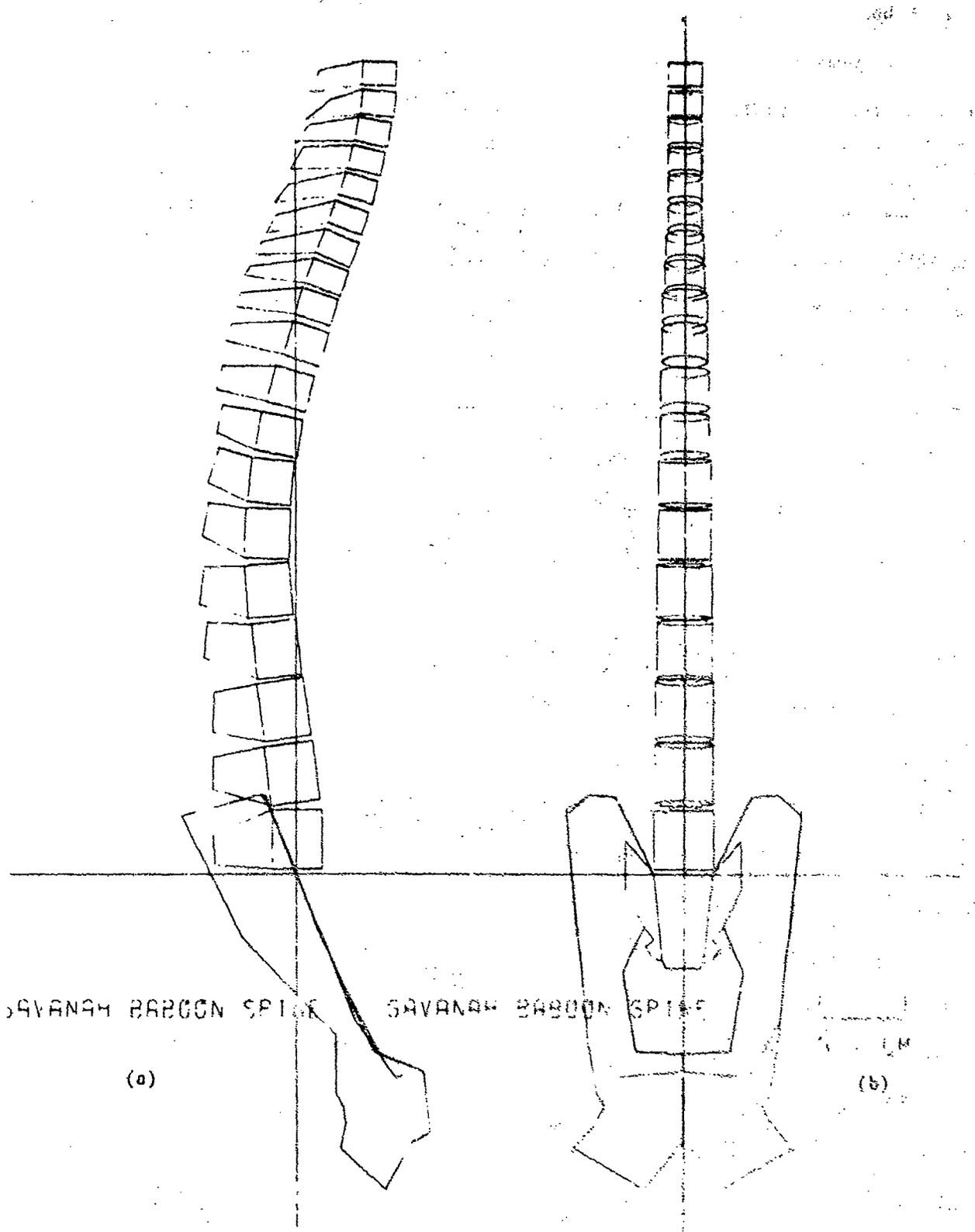

Figure 5.6. Baboon spine model: (a) sagittal plane view; (b) frontal plane view

TABLE 5.6

BABOON INERTIA DATA

Level	Mass m ($gm \times 10^2$)	Moments of Inertia ($gm\text{-}cm^2 \times 10^3$) I_{xx}	I_{yy}	I_{zz}
Head	9.266	21.990	20.240	9.158
T1	1.989	2.708	2.708	5.373
T2	2.041	2.780	2.780	5.513
T3	2.438	3.333	3.333	6.585
T4	2.387	3.262	3.262	6.448
T5	2.456	3.358	3.358	6.634
T6	2.300	3.140	3.140	6.213
T7	2.490	3.406	3.406	6.726
T8	2.508	3.431	3.431	6.774
T9	2.525	3.455	3.455	6.820
T10	2.560	3.504	3.504	6.915
T11	2.940	4.041	4.041	7.941
T12	3.165	4.363	4.363	8.594
L1	3.476	4.812	4.812	9.389
L2	3.857	5.369	5.369	10.418
L3	3.994	5.573	5.573	10.791
L4	4.583	6.458	6.458	12.379
L5	4.566	6.432	6.432	12.333
L6	4.496	6.325	6.325	12.144
L7	4.341	6.091	6.091	11.726
Pelvis	16.430	37.200	37.200	59.173

TABLE 5.7

STIFFNESSES OF BABOON DISCS

Level	Axial Stiffness (dyne/cm x 10^8)	Bending (dyne-cm/rad x 10^8)	Torsional (dyne-cm/rad x 10^8)
Neck	0.25	1.76	1.50
T1	1.90	1.56	1.33
T2	1.60	1.60	1.37
T3	1.70	1.45	1.23
T4	1.80	1.07	0.91
T5	2.10	0.98	0.84
T6	2.00	0.42	0.36
T7	2.20	0.51	0.43
T8	2.40	0.45	0.38
T9	2.50	0.43	0.37
T10	2.80	0.34	0.29
T11	2.90	0.34	0.29
T12	3.10	0.30	0.25
L1	3.00	0.24	0.20
L2	4.40	0.28	0.24
L3	4.70	0.22	0.19
L4	5.20	0.18	0.15
L5	5.70	0.18	0.15
L6	5.60	0.22	0.19
L7	5.90	0.30	0.25

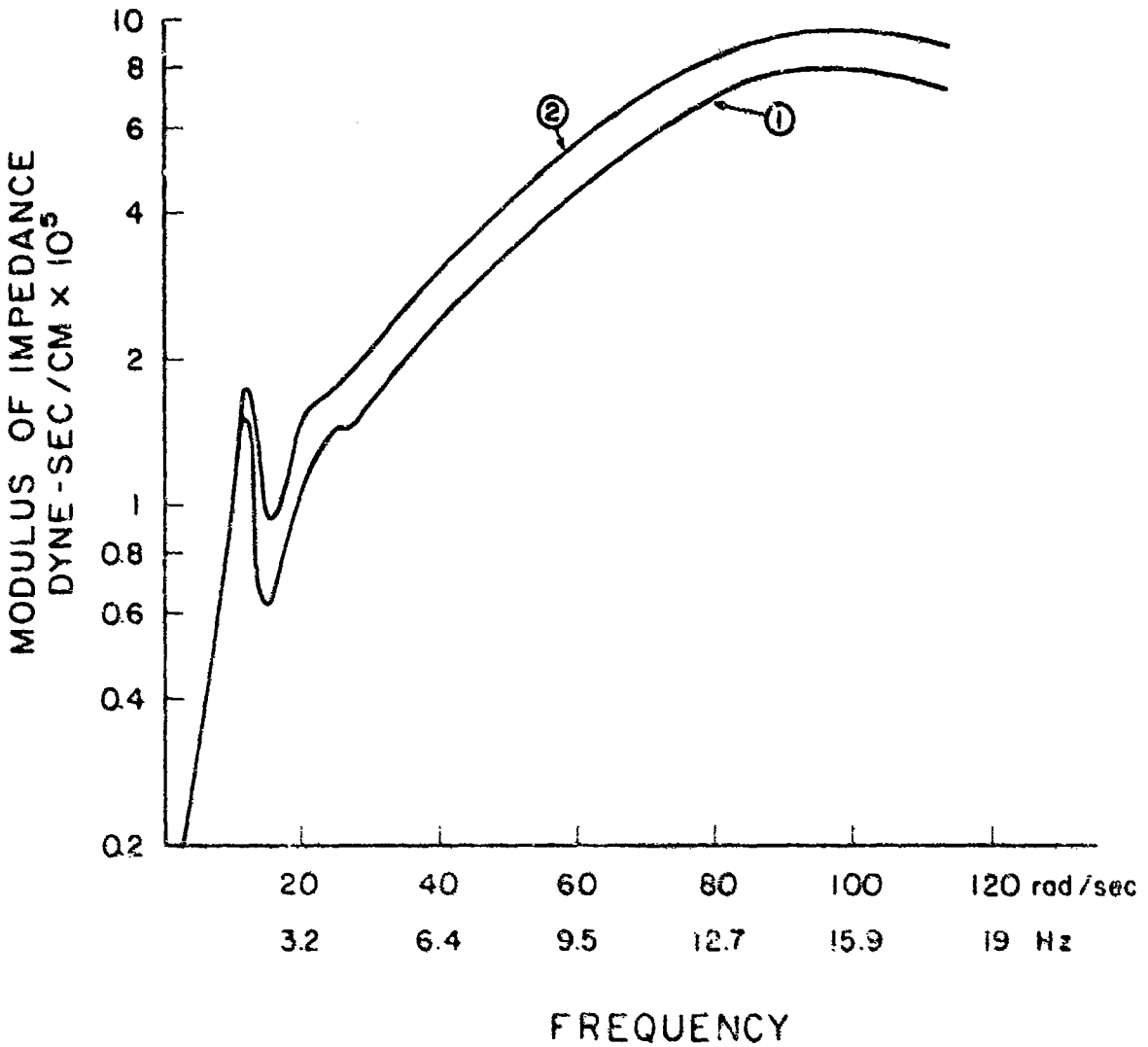

Figure 5.7. Impedance of baboon: (1) without pelvic mass; (2) pelvic mass included

V.3 Rhesus Monkey

For the rhesus monkey, only the measurements and skeletal figures were available for data extraction. The geometry of the model is shown in Fig. 5.8. For the rhesus monkey a total weight of 21 lbs (9.55 kg mass) was specified, so the mass distribution data was scaled from the baboon. Stiffness data was obtained using the same procedures as for the chimpanzee and baboon. Inertial and stiffness data is given in Tables 5.8 and 5.9. The impedance of the rhesus monkey model is also shown in Fig. 5.9.

In addition to better stiffness data, which is needed for all of the primate models, specific inertia data would be useful for the rhesus monkey.

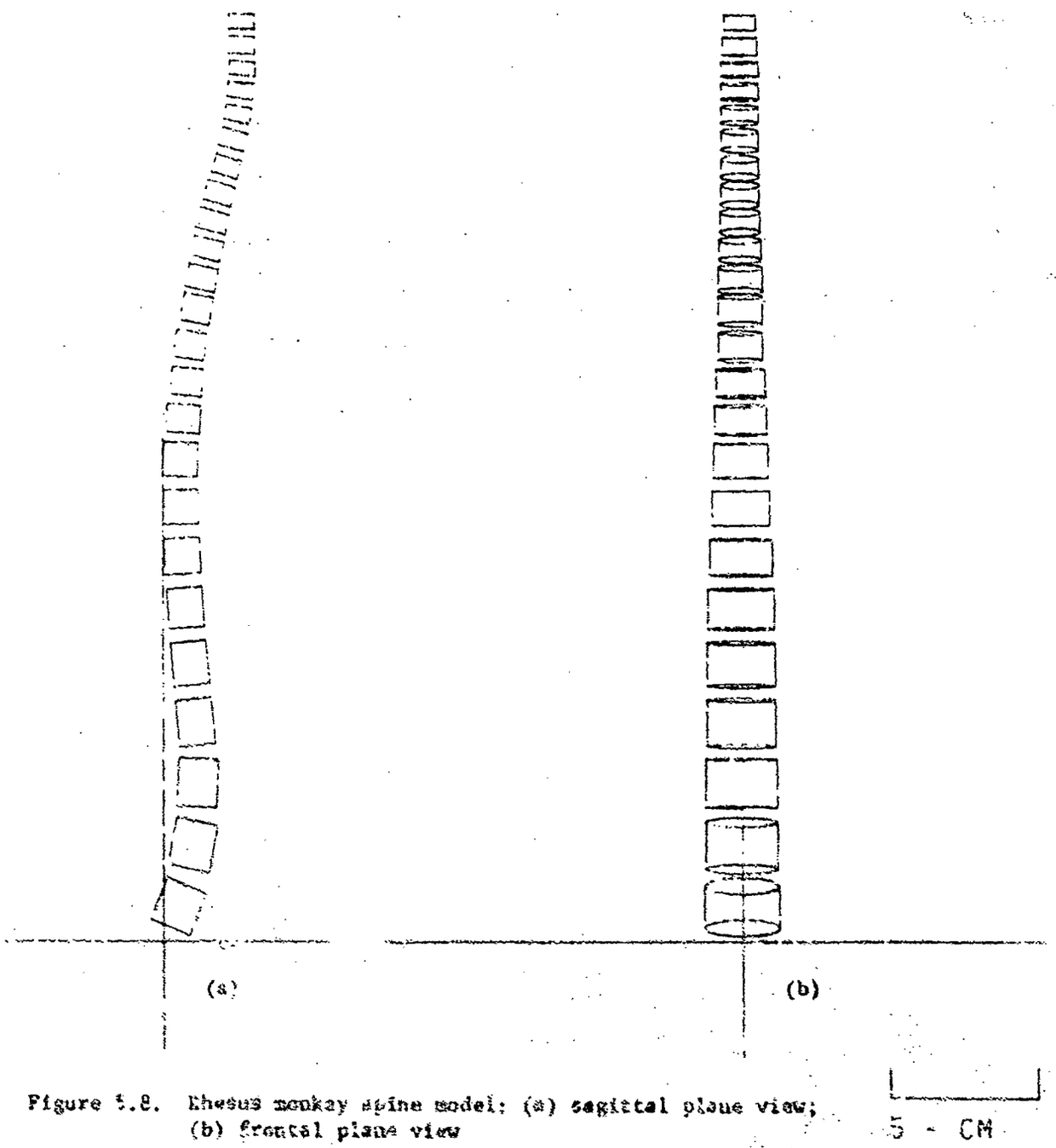

Figure 5.8. Rhesus monkey spine model: (a) sagittal plane view; (b) frontal plane view

Table 5.8. Rhesus monkey inertia data

Level	Mass m ($gm \times 10^2$)	Moments of Inertia ($gm\text{-}cm^2 \times 10^3$) I_{xx}	I_{yy}	I_{zz}
Head	6.520	7.465	7.465	7.465
T1	0.813	0.683	0.683	1.358
T2	0.952	0.801	0.801	1.590
T3	0.941	0.792	0.792	1.572
T4	0.941	0.792	0.792	1.572
T5	0.952	0.801	0.801	1.590
T6	1.941	0.792	0.792	1.572
T7	1.070	0.902	0.902	1.787
T8	1.251	1.059	1.059	2.090
T9	1.241	1.050	1.050	2.072
T10	1.241	1.050	1.050	2.072
T11	1.369	1.162	1.162	2.287
T12	1.551	1.322	1.322	2.590
T13	1.636	1.399	1.399	2.733
L1	1.690	1.446	1.446	2.823
L2	1.829	1.572	1.572	3.055
L3	2.064	1.788	1.788	3.448
L4	2.118	1.838	1.838	3.537
L5	2.139	1.858	1.858	3.573
L6	2.107	1.828	1.828	3.519
L7	2.011	1.739	1.739	3.359
Pelvis	10.490	16.865	16.865	23.364

Table 5.9. Rhesus monkey stiffness data

Level	Axial Stiffness (dyne/cm x 10^8)	Bending (dyne-cm/rad x 10^7)	Torsional (dyne-cm/rad x 10^7)
Neck	0.02	2.10	1.70
T1	1.20	1.50	1.30
T2	1.10	0.90	0.80
T3	1.10	1.50	1.30
T4	1.30	1.90	1.70
T5	1.50	2.20	1.90
T6	1.70	3.00	2.50
T7	1.60	2.20	1.90
T8	1.30	1.60	1.40
T9	1.70	2.40	2.00
T10	1.90	3.40	2.90
T11	2.10	4.20	3.60
T12	2.40	3.30	2.80
T13	2.40	3.30	2.80
L1	2.90	4.80	4.10
L2	3.10	5.10	4.30
L3	3.30	6.00	5.10
L4	3.20	5.50	4.70
L5	4.00	9.10	7.70
L6	3.50	7.00	6.00
L7	4.00	9.40	8.00

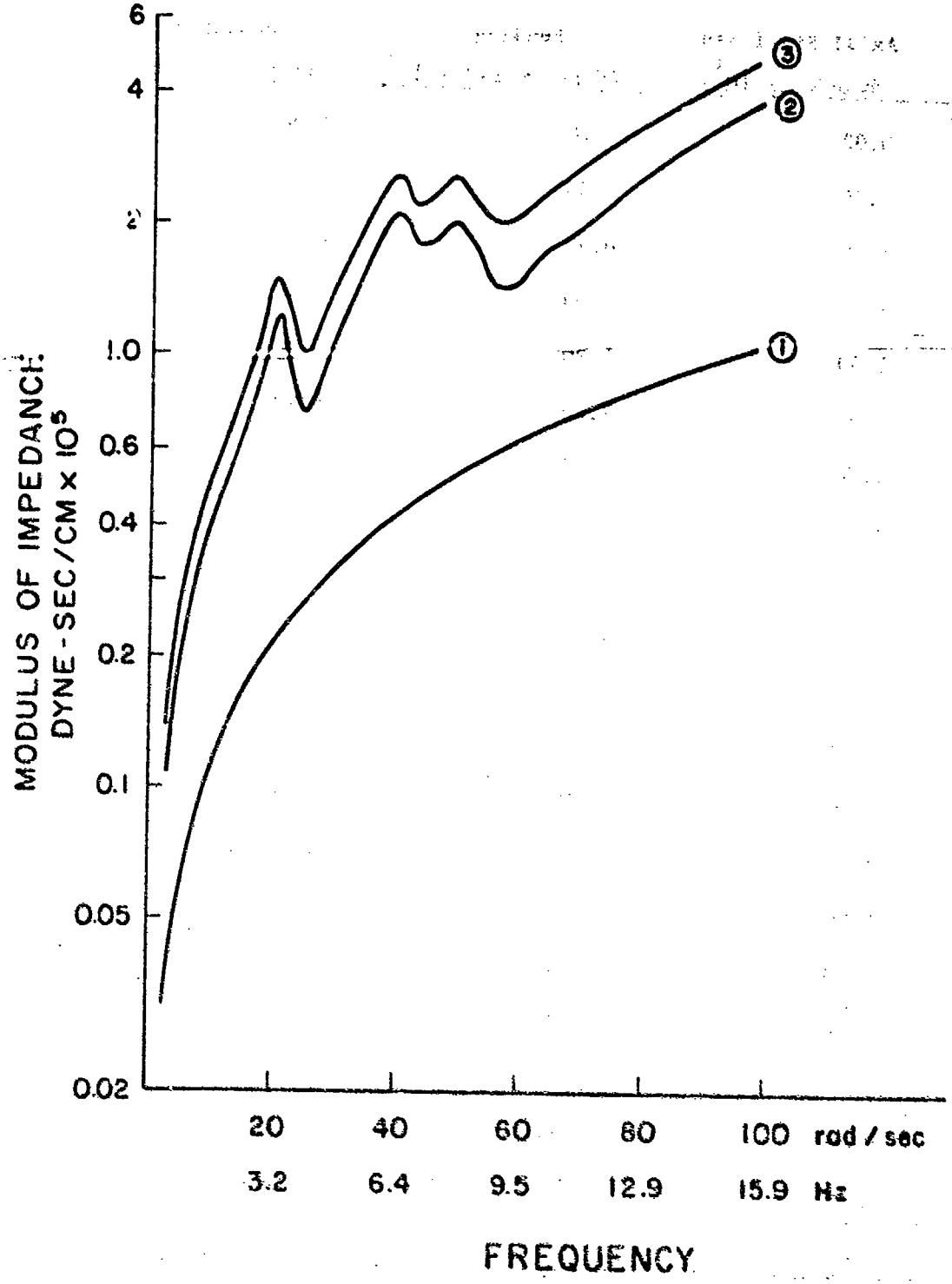

Figure 5.9. Impedance of rhesus monkey: (1) pelvic mass impedance: (2) without pelvis; (3) with pelvis

CHAPTER VI

SIMULATIONS OF PRE-EJECTION PILOT ALIGNMENT

VI.1 Motivation and Method

Mohr, et al., (1969) and Li, et al., (1970), have discussed the importance of the pre-ejection posture as a factor in modifying a crewman's tolerance to accelerations experienced during ejection from disabled high performance aircraft. According to Bosee and Payne (1961), the optimal spinal alignment is the normal seated position, with the vertebral bodies "located squarely over each other". Any deviation from this optimal spinal configuration, such as that resulting when a crewman is slumped forward or sidewards in the seat, would increase the possibility of injury during ejection.

In this Chapter we will consider the pilot alignment phase of the ejection sequence and will present a method for analyzing the spinal response to loadings encountered during alignment.

VI.2 Computer Modeling of Belt and Shoulder

The pre-ejection pilot alignment is accomplished via the powered inertia lock reel which, when required, activates the restraining belt, forcing the crew member into the eject position (Fig. 6.1). In the pre-ejection alignment models the belt forces are transmitted to the spine through rigid bodies representing the shoulders and through the ribs. Based on the work of Eycleshymer and Schoemaker (1970), it was determined that the sagittal plane cross-sections of the shoulders could be approximated as circular segments.

The belt forces are transmitted to the shoulder rigid bodies and the ribs through points (which we shall call contact points) which approximate the shape of the upper torso in planes parallel to the sagittal (yz) plane, 8.13 cm on either side of the sagittal plane. Fig. 6.2 shows a typical contact point configuration in a plane parallel to the sagittal plane. Contact points 1 to j + 2 are secondary

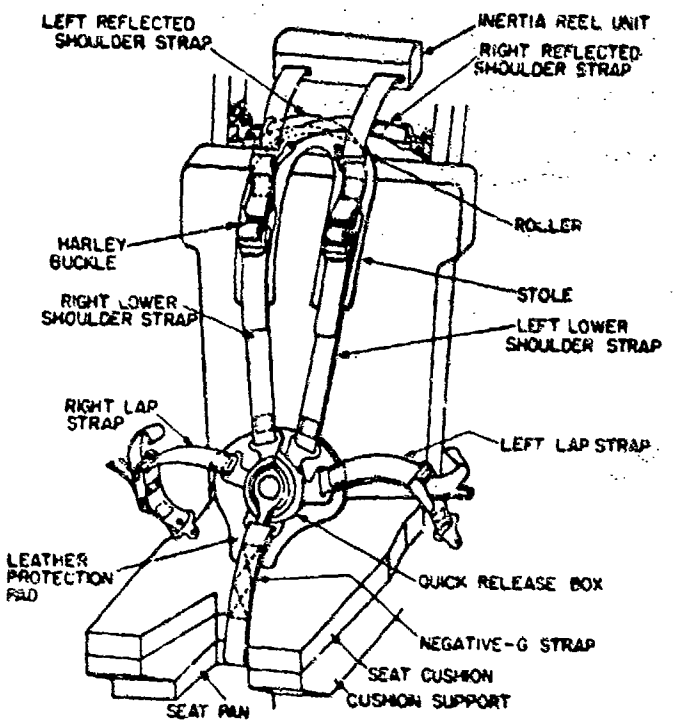

Figure 6.1. Typical inertia reel unit and harness configuration.

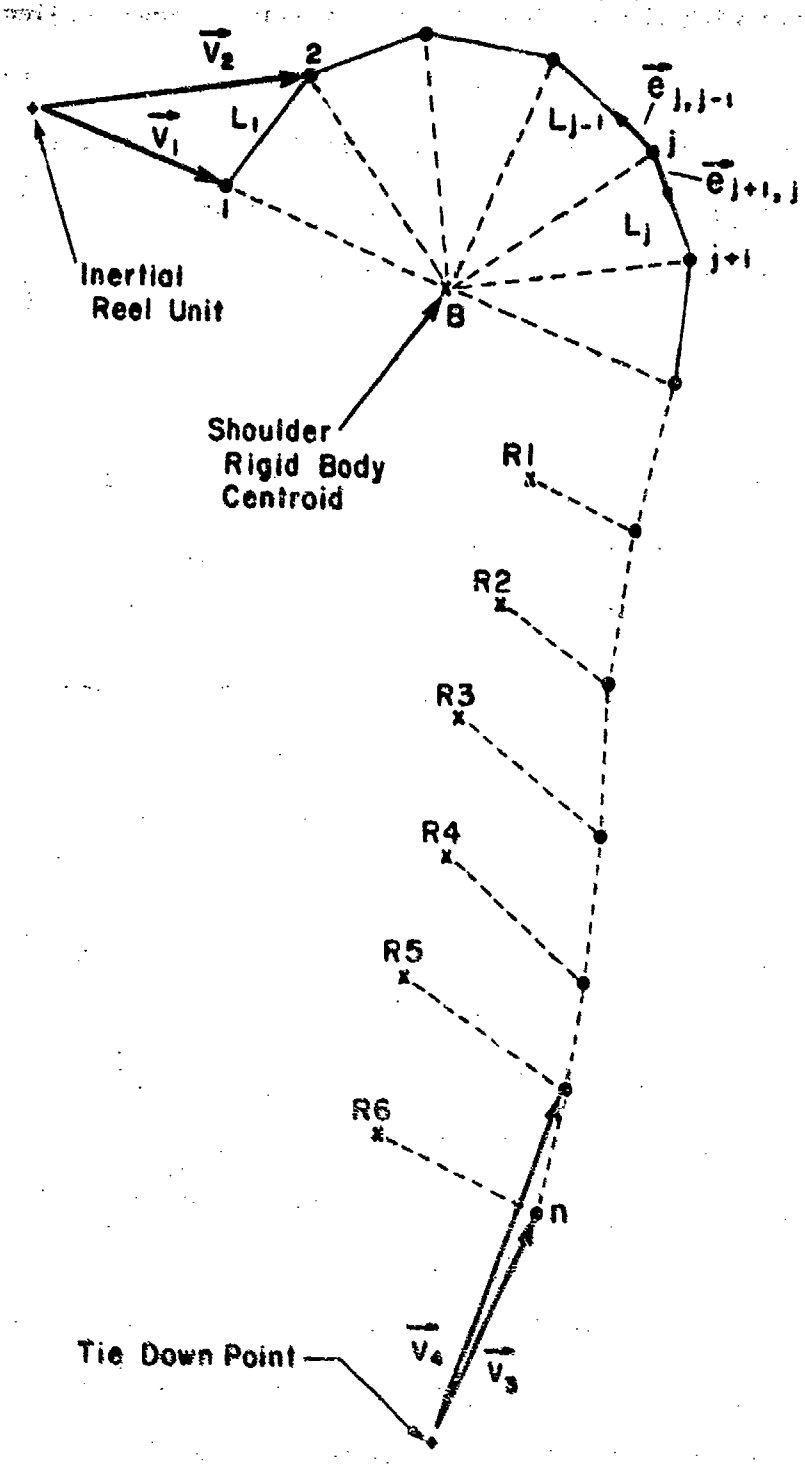

Figure 6.2. Typical contact point configuration.

nodes associated with the shoulder rigid body primary node, called SRB. Contact points j + 3, to n are secondary nodes associated with ribs, R1 to R6, respectively. Each rib has only one contact point. The inertia lock reel (ILR) and tie down point (TDP) locations shown in Fig. 6.2 are not drawn to scale.

At each time step, t_i, the location of a contact point, J, is given by

$$x_{kJ}(t_k) = x_{kJ}(t_{i-1}) + u_{kJ}(t_{i-1}) \tag{6.1}$$

where

x_{1J}, x_{2J}, x_{3J} are the global coordinates; (x_1 and x, x_2 and y and x_3 and z are used interchangeably)

$u_{kJ}(t_{i-1})$ = displacements of contact point J computed at time step t_{i-1}.

Next a check is made for contact between the belt and the contact points. Contact between a posterior contact point (toward the seatback) and the belt is determined by checking whether contact at that point would introduce any concave kinks into the belt. At all times, the position of the inertia lock reel (ILR) is given, so this is determined by checking the sign of the global x component of the cross product of the vector from the inertia lock reel to a possible contact point and the vector from the inertia lock reel to the next contact point, as illustrated for contact point 1 in Fig. 6.2, where the condition would be

$$\vec{i}\cdot(\vec{v}_1 \times \vec{v}_2) \quad \begin{cases} \leq 0, \text{ belt does not contact point 1} \\ > 0, \text{ belt contacts point 1.} \end{cases} \tag{6.2}$$

Contact between an anterior (chest side) contact point and the belt is similarly determined so that no concave kinks exist in the belt between the chest and the tie down point. For example, for contact point n in Fig. 6.2,

$$\vec{i}\cdot(\vec{v}_3 \times \vec{v}_4) \quad \begin{cases} \geq 0, \text{ belt does not contact point n} \\ < 0, \text{ belt contacts point n.} \end{cases} \tag{6.3}$$

No force is applied to any point which is not in contact with the belt, so loss of

contact between the belts and parts of the shoulder and torso is possible.

The force (in the plane of the contact points) on a typical contact point, for example point J in Fig. 6.2, is determined by

$$\vec{F}_J = T\,(\vec{e}_{J,J-1} + \vec{e}_{J+1,J}) \tag{6.4}$$

where T = belt tension, and $\vec{e}_{J,J-1}$ and $\vec{e}_{J+1,J}$ are unit vectors along the belt as shown in Fig. 6.2.

The global components of $\vec{F}_J$ are then given by

$$\begin{aligned} F_{xJ} &= T\left(\frac{x_{J-1,J}}{L_{J-1}} + \frac{x_{J+1,J}}{L_J}\right) \\ F_{yJ} &= T\left(\frac{y_{J-1,J}}{L_{J-1}} + \frac{y_{J+1,J}}{L_J}\right) \\ F_{zJ} &= T\left(\frac{z_{J-1,J}}{L_{J-1}} + \frac{z_{J+1,J}}{L_J}\right) \end{aligned} \tag{6.5}$$

where $x_{J-1,J} = x_{J-1} - x_J$, etc.

L_J = distance between contact points J+1 and J.

Once the global components of the contact forces have been computed at the contact points, they are transformed into forces and moments acting at the primary nodes (mass centers) of the shoulder rigid bodies and the ribs.

The resultant force at a shoulder rigid body primary node is given by

$$RF_j = \sum_{I=1}^{m} F_{jI} \tag{6.6}$$

where m = number of contact points defining the shoulder rigid body. The resultant moment at a shoulder rigid body primary node is given by

$$\{RM\} = \left[\sum_{I=1}^{m} [\Omega_I]\,[\,]^T\,\{F_I\}\right] \tag{6.6}$$

where

$$[\Omega_I] = \begin{bmatrix} 0 & -\bar{z}_I & \bar{y}_I \\ \bar{z}_I & 0 & -\bar{x}_I \\ -\bar{y}_I & \bar{x}_I & 0 \end{bmatrix} \tag{6.8}$$

and $\bar{x}_I$ are expressed in the body coordinate system of the coordinates of primary node P, and $[\lambda]$ is the body to global coordinate system transformation matrix for the shoulder rigid body primary node P. Since each rib has only one contact point, the forces and moments at the rib primary nodes are given by Eqs. (6.6) and (6.7) without the summations.

The belt forces on the contact points, once they are transformed into forces and moments at the primary nodes of the shoulder rigid bodies, are treated like the other external forces in the equations of motion. No predictor programming is included, so the belt model is only suited for explicit time integration.

The morphology of the interconnections of shoulders and spine is rather complicated. Furthermore, data on the various components of the interconnective tissues are not available. Since forces in these interconnectors themselves were not of interest, they were simplified as much as possible.

The shoulder rigid bodies were connected by beam elements to T1, T2 and T3, (see Fig. 6.3), and the stiffnesses of the beam elements were chosen on the basis of a parameter study. The stiffnesses were varied so that when the shoulders are pulled back, the spinal displacement would lag behind the shoulder displacements by a small amount, but so that no snapback or overshoot in the spinal response was observed. The stiffnesses of these elements and locations of the contact points are given in Table 6.1.

VI.3 Pre-Ejection Pilot Alignment Models

In the following, we will describe how the spine models were prepared for the simulation of the pre-ejection alignment runs. We will designate these models as PAMX-Y, where PAM denotes Pre-ejection Alignment Model and X indicates the initial forward displacement of T1, and Y (if present) indicates an initial lateral displacement. The models, PAM2, PAM4 and PAM4-4, were constructed from the isolated, ligamentous spine without a rib cage. In PAM6, the entire model was included. PAM2

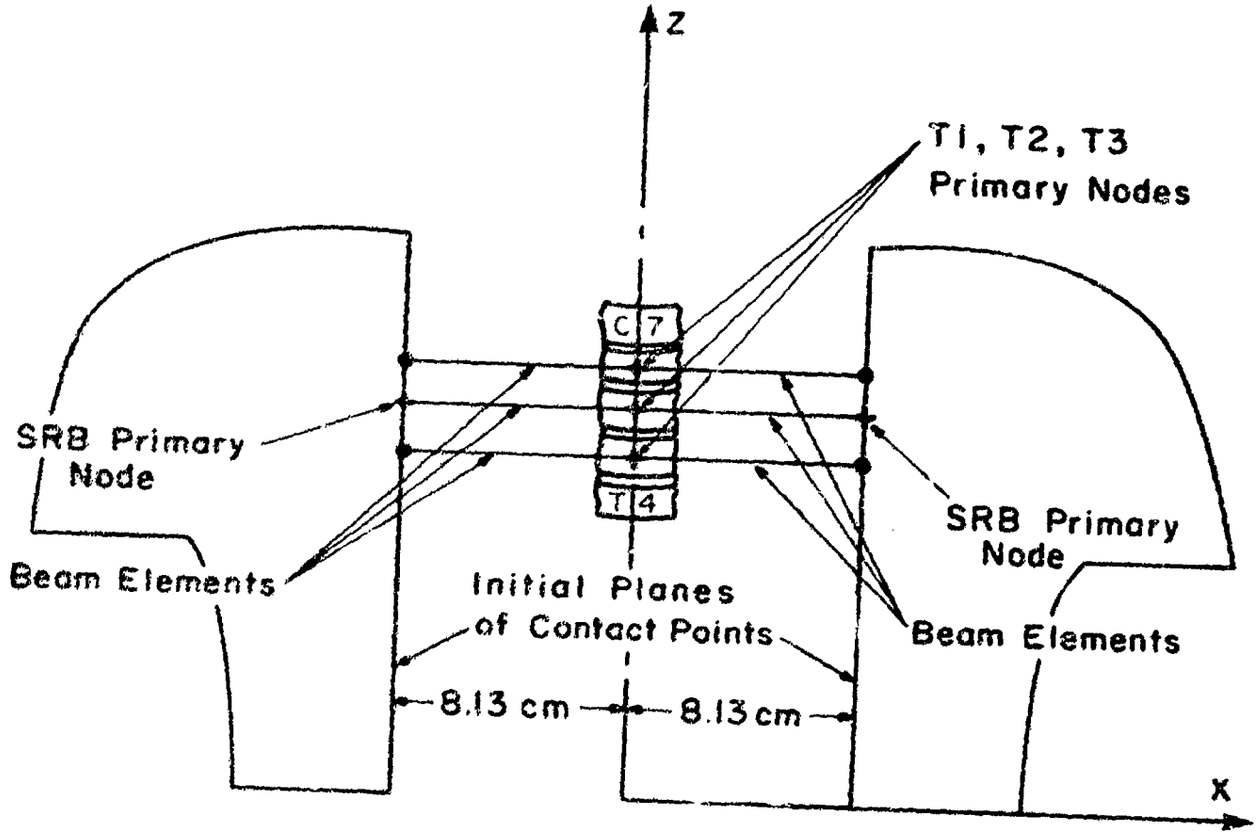

Figure 6.3 Frontal plane view of the beam elements connecting the shoulder rigid bodies to vertebrae T1, T2 and T3.

Table 6.1. Coordinates of contact points and stiffnesses of beam elements connecting the shoulder rigid bodies to vertebra T1, T2 and T3.

LSRB[1] primary node global coordinates (cm):

x = 8.130, y = -13.943, z = 42.900

Local coordinates [2] of contact points (CP)

CP	$\hat{x}$	$\hat{y}$	$\hat{z}$
1	0.0	6.447	2.725
2	0.0	4.221	5.583
3	0.0	0.864	6.946
4	0.0	-2.726	6.448
5	0.0	-5.584	4.222
6	0.0	-6.947	0.865
7	0.0	-6.448	-2.725

Global coordinates of left rib primary nodes and local coordinates[3] of associated contact point (CP)

Rib	x	y	z	CP	$\hat{x}$	$\hat{y}$	$\hat{z}$
1	2.556	-16.328	41.569	8	5.574	-2.871	-5.069
2	3.380	-16.355	37.915	9	4.750	-2.245	-5.515
3	4.115	-15.548	34.556	10	4.015	-2.938	-6.374
4	5.121	-14.320	31.460	11	3.009	-3.827	-7.033
5	5.548	-14.089	27.768	12	2.782	-3.535	-6.305
6	5.574	-12.958	24.478	13	2.556	-3.960	-6.255

Stiffnesses of beam elements between shoulder rigid bodies and T1-T3

Axial: 5×10^7 dyne-cm

Torsion: 1×10^7 dyne-cm

Bending: $k_1 + k_2\theta^2$

$k_1 = 1 \times 10^7$ dyne-cm

$k_2 = 1 \times 10^{10}$ dyne-cm/rad^2

[1] LSRB = left shoulder rigid body

[2] Origin located at LSRB primary node

[3] Origin located at primary node of rib

The right hand side configuration is a mirror image of the left side.

(Fig. 6.4) was obtained by taking the isolated thoraco-lumbar spine model (Fig. 2.1), and placing T1 5.08 cm (2 in) forward from its undeformed position, which is approximately 9.3 cm (3.7 in) forward from the seatback. The remaining vertebral bodies were then positioned so as to obtain a smooth curve for the spine, which is shown in Fig. 6.4.

PAM4 (Fig. 6.5) was obtained from the normal configuration of the isolated thoraco-lumbar spine by a static analysis in which T1 was displaced forward from its undeformed position by 10.16 cm. (4 in). The static analysis then determined the remaining vertebral positions by equilibrium. The initial location of T1 is approximately 14.4 cm (5.7 in) from the seatback.

In PAM4-4 (Figs. 6.6 and 6.7) vertebra T1 was displaced 4 inches forward and 4 inches to the left. The initial configuration was obtained in the same manner as PAM4.

PAM6 (Fig. 6.8) was obtained by taking the complex spine model, CSM (Fig. 2.2) and rotating it forward about L5 until T1 was 15.24 cm. (6 in) forward from its undeformed position. This is approximately 19.4 cm (7.7 cm) from the seatback.

VI.4. Pre-Ejection Pilot Alignment Studies

VI.4.1 Study 1.

In the first study, the shoulder rigid bodies were modeled with 6 contact points per shoulder, as shown in Fig. 6.9 and 6.10. The shoulders are aligned symmetrically with respect to the seatback. The reel is located at approximately the standard height, 3.4 cm (1.3 in) above the acromion. From Kycleshymer and Schoemaker (1970), the acromion appears to be approximately 3.2 cm (1.3 in) above the centroid of T1, while from Pansky and House (1964), the acromion appears to coincide with the bottom of T1. The acromion height in the spine models was taken to be the average of these two values. The tie down points are 8.13 cm (3.2 in) on either side of the pelvic mass center. The force in each belt was zero initially and increased linearly to

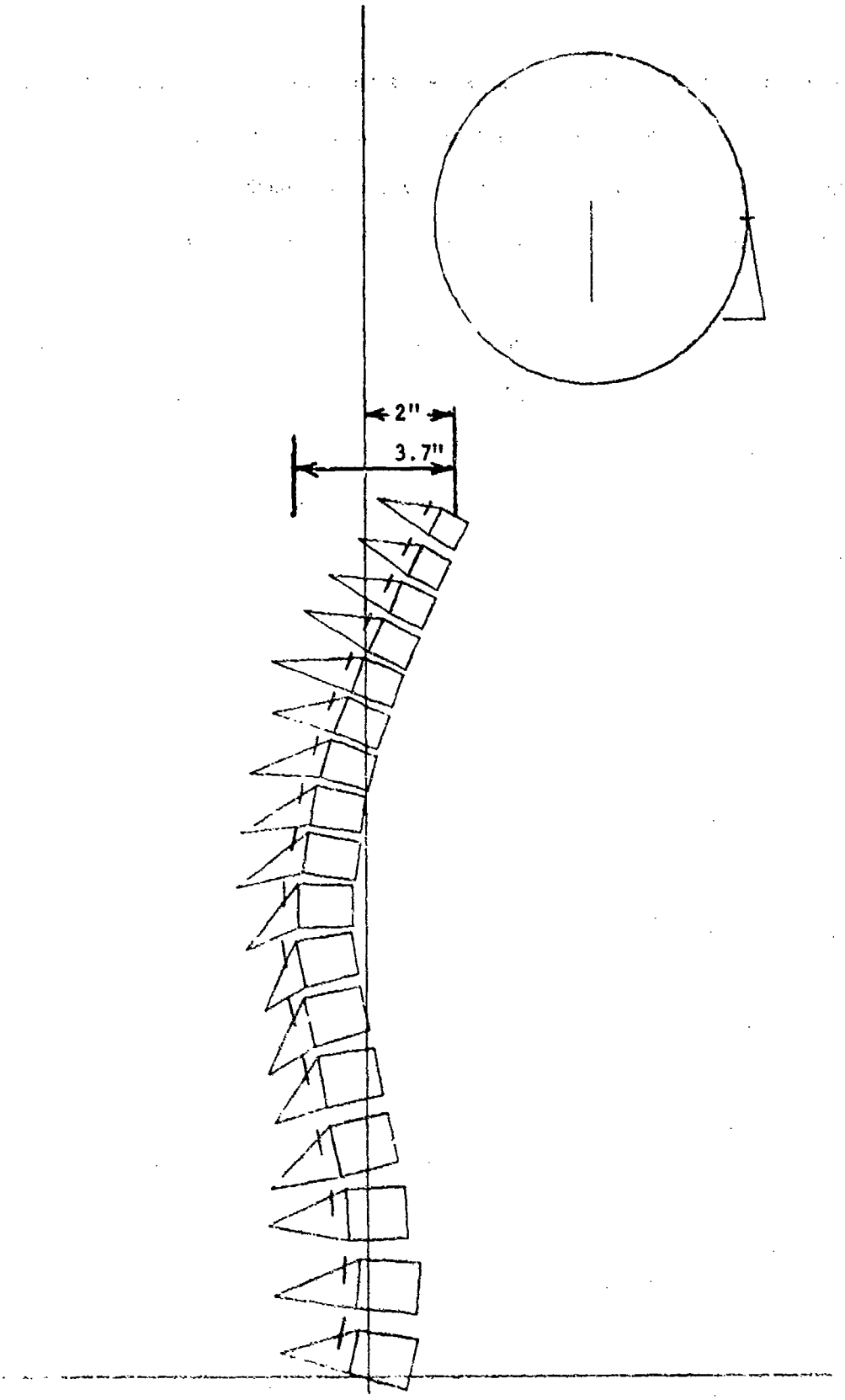

Figure 6.4. PAM2; Pre-ejection pilot alignment model with T1 2" forward from the normal position.

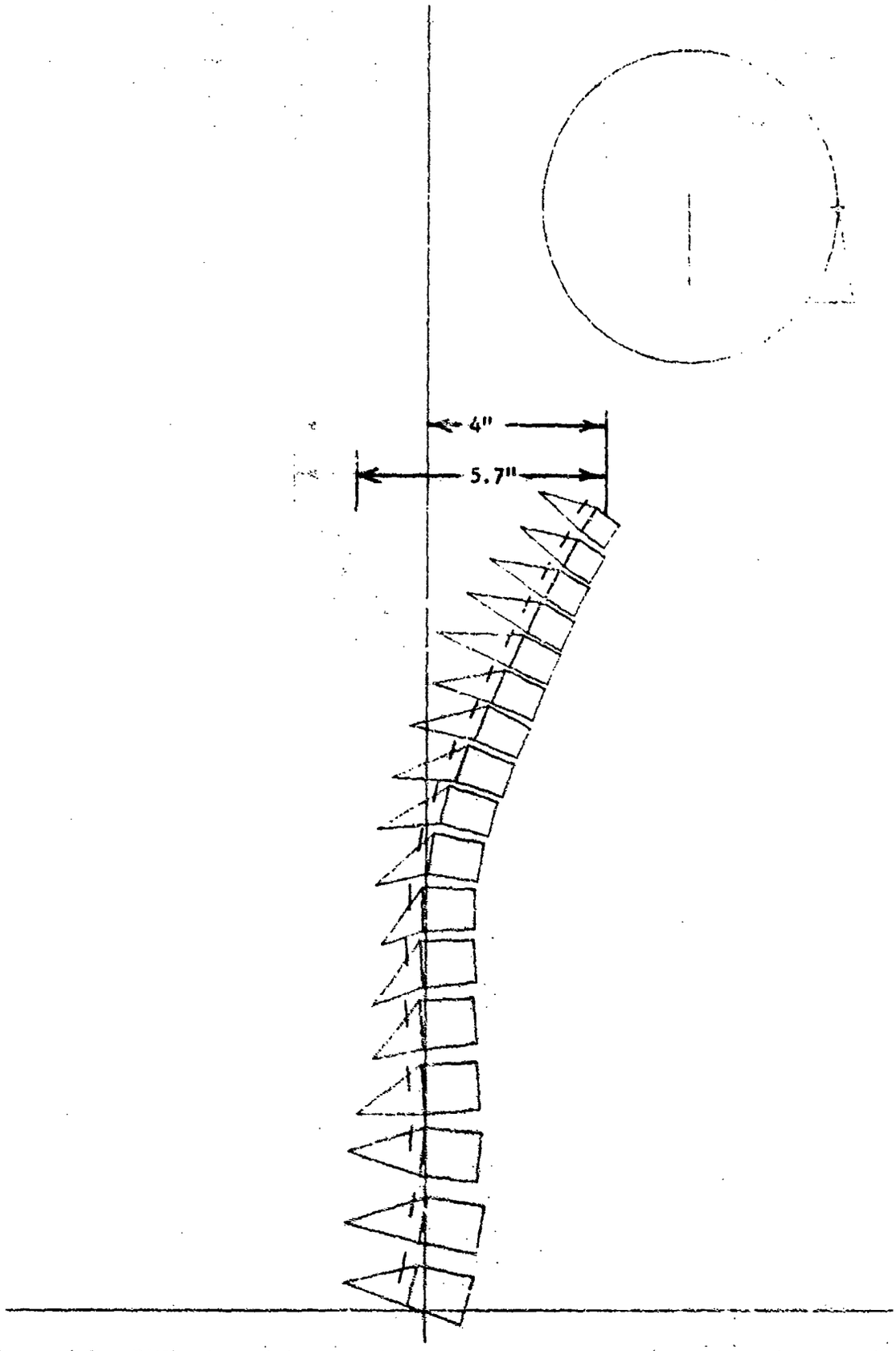

Figure 6.5. PAM4; Pre-ejection pilot alignment model with T1 4" forward from the normal position.

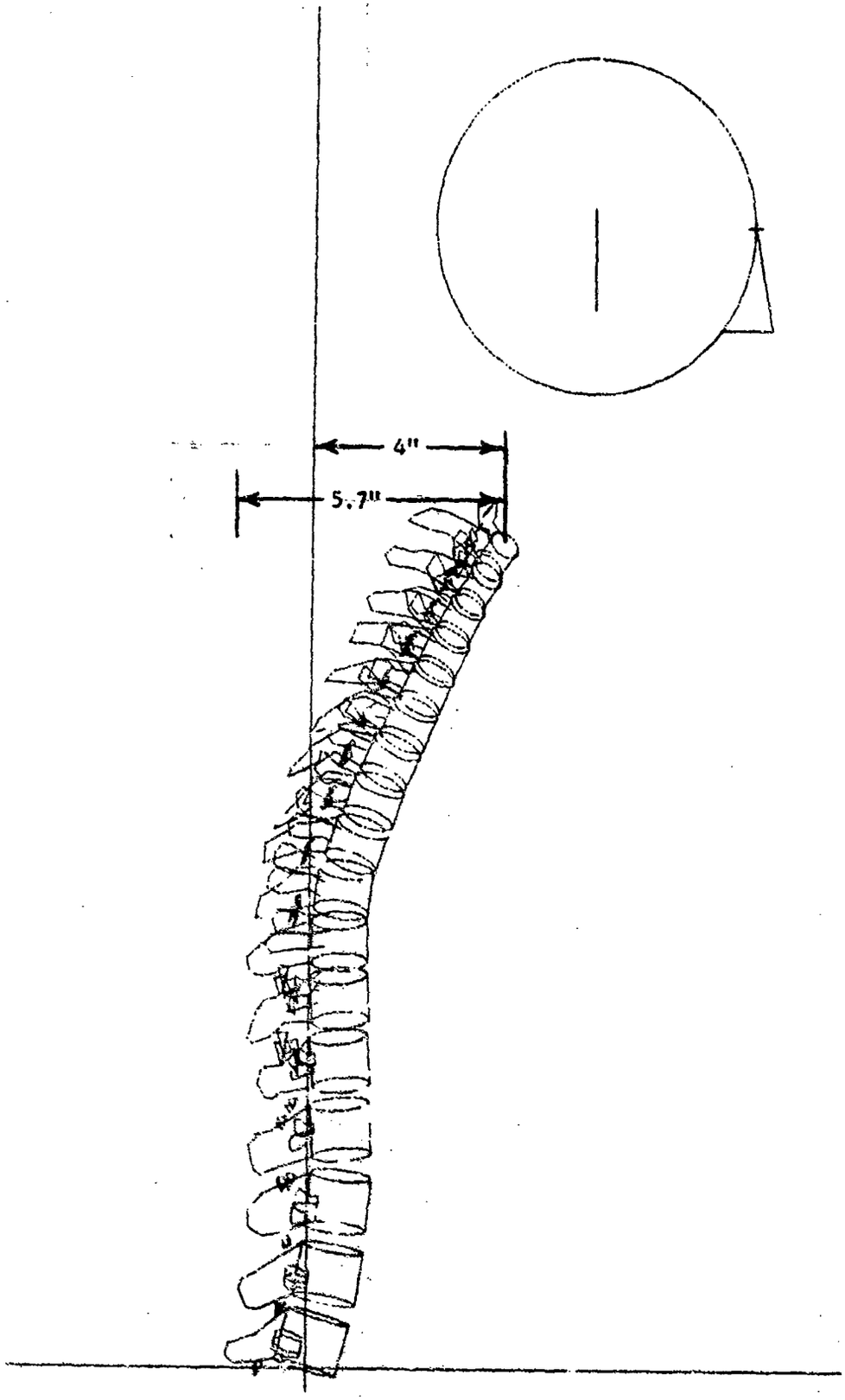

Figure 6.6 PAM4-4; Pre-ejection alignment model with T1 4" forward and to the left of the normal position - sagittal plane view.

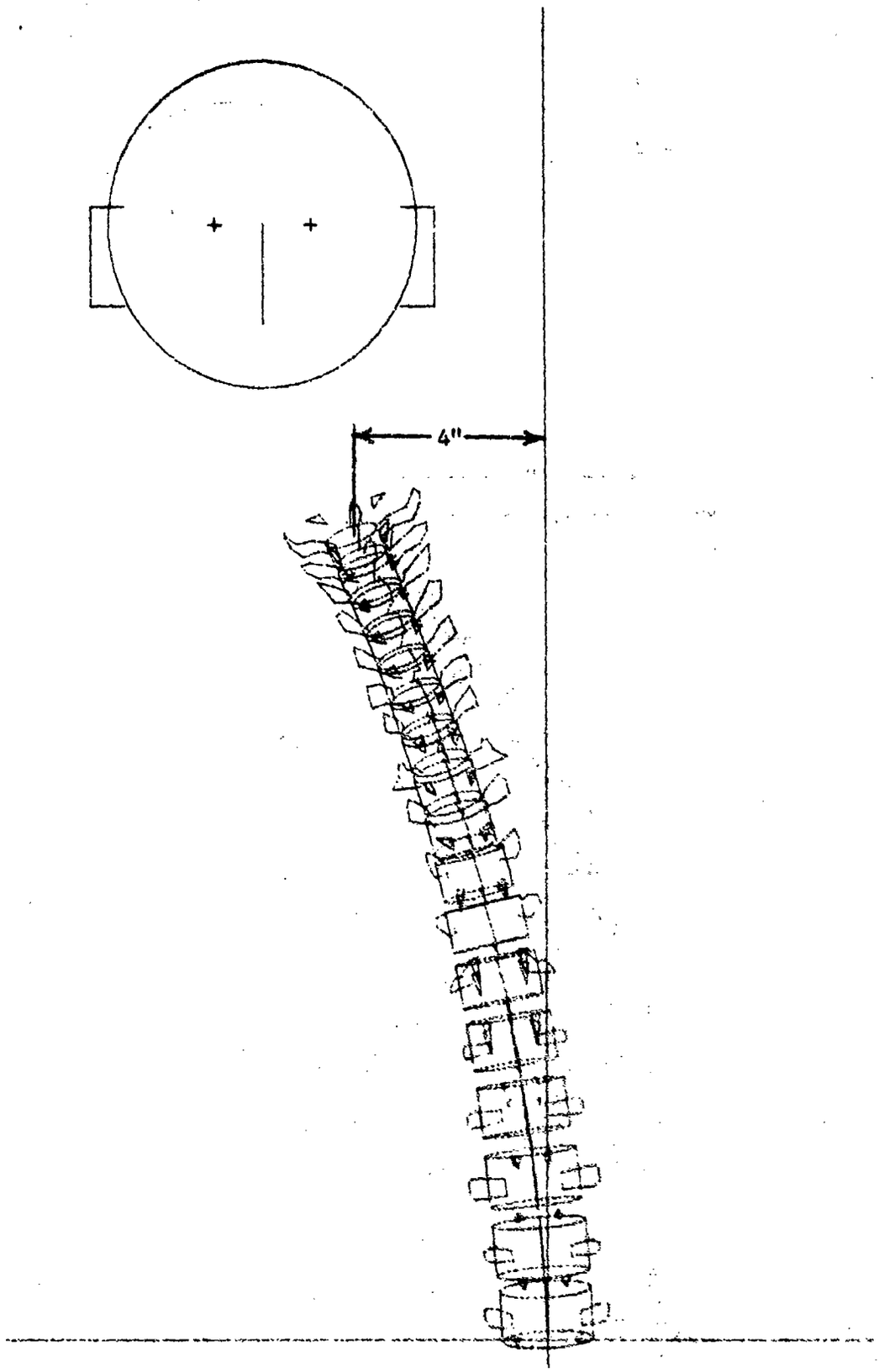

Figure 6.7. PAM4-4; Frontal plane view.

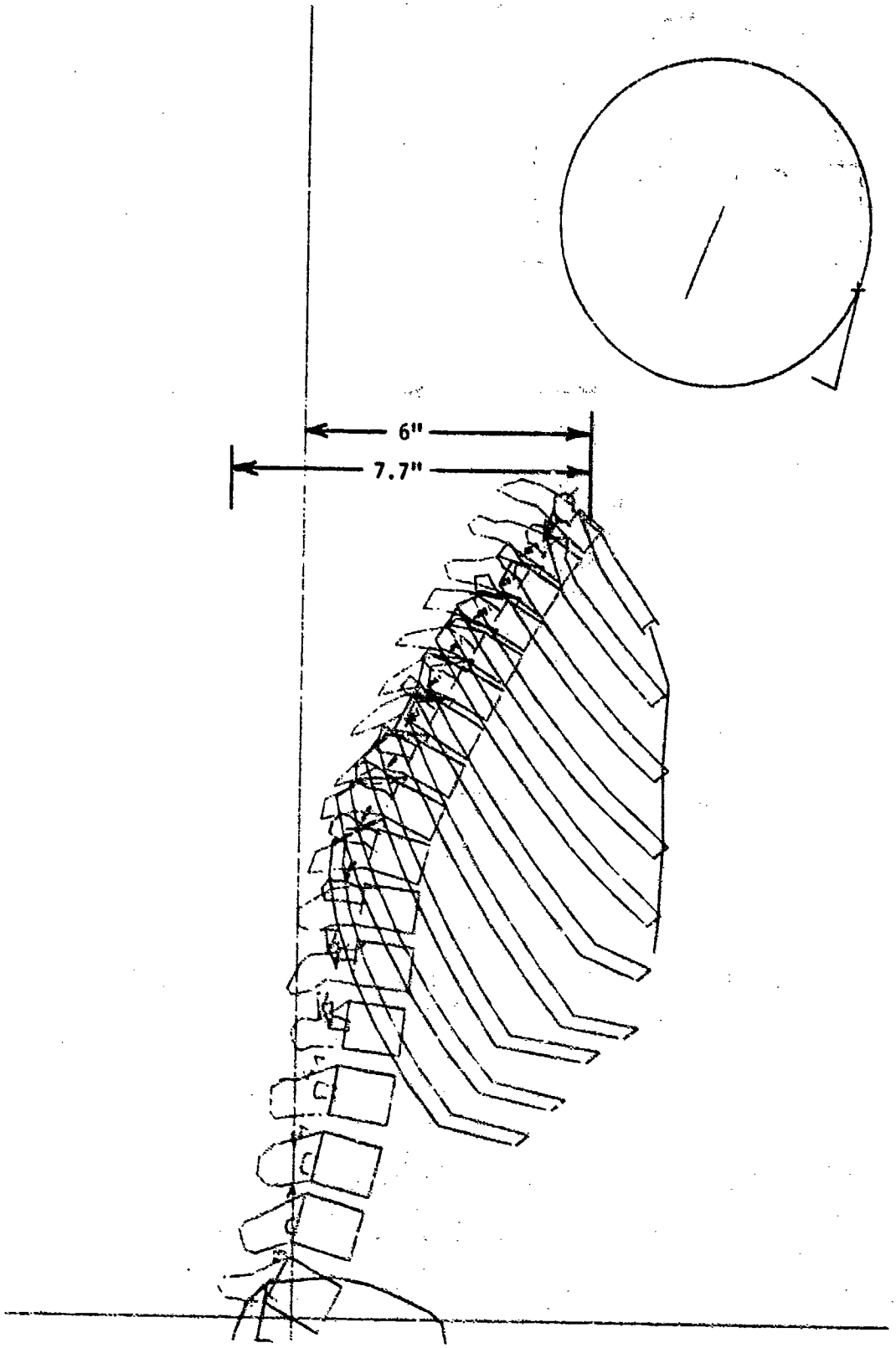

Figure 6.8. PAM6; Pre-ejection pilot alignment model with T1 6" forward from the normal position.

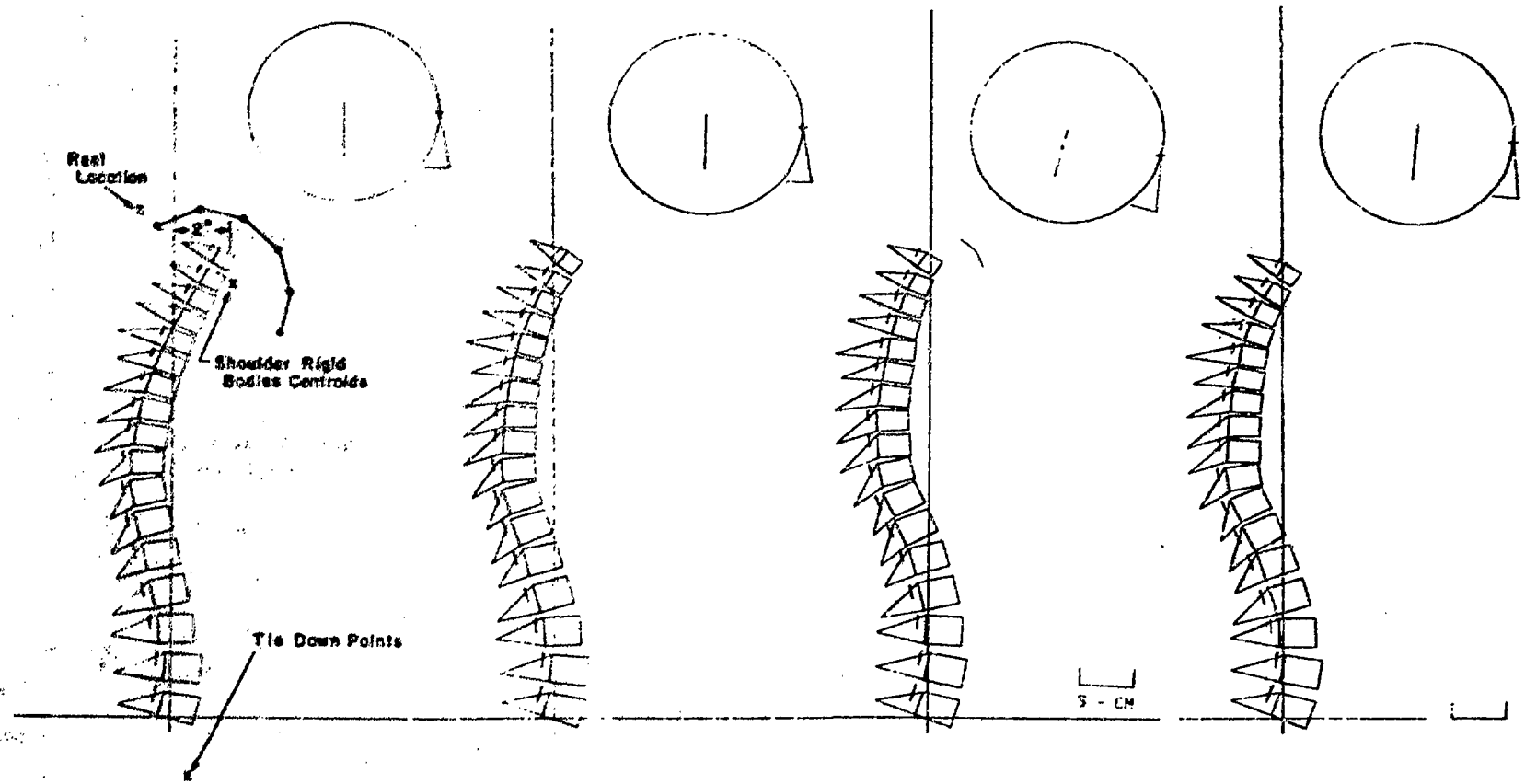

Figure 6.9. Study 1: Response of PAM2.

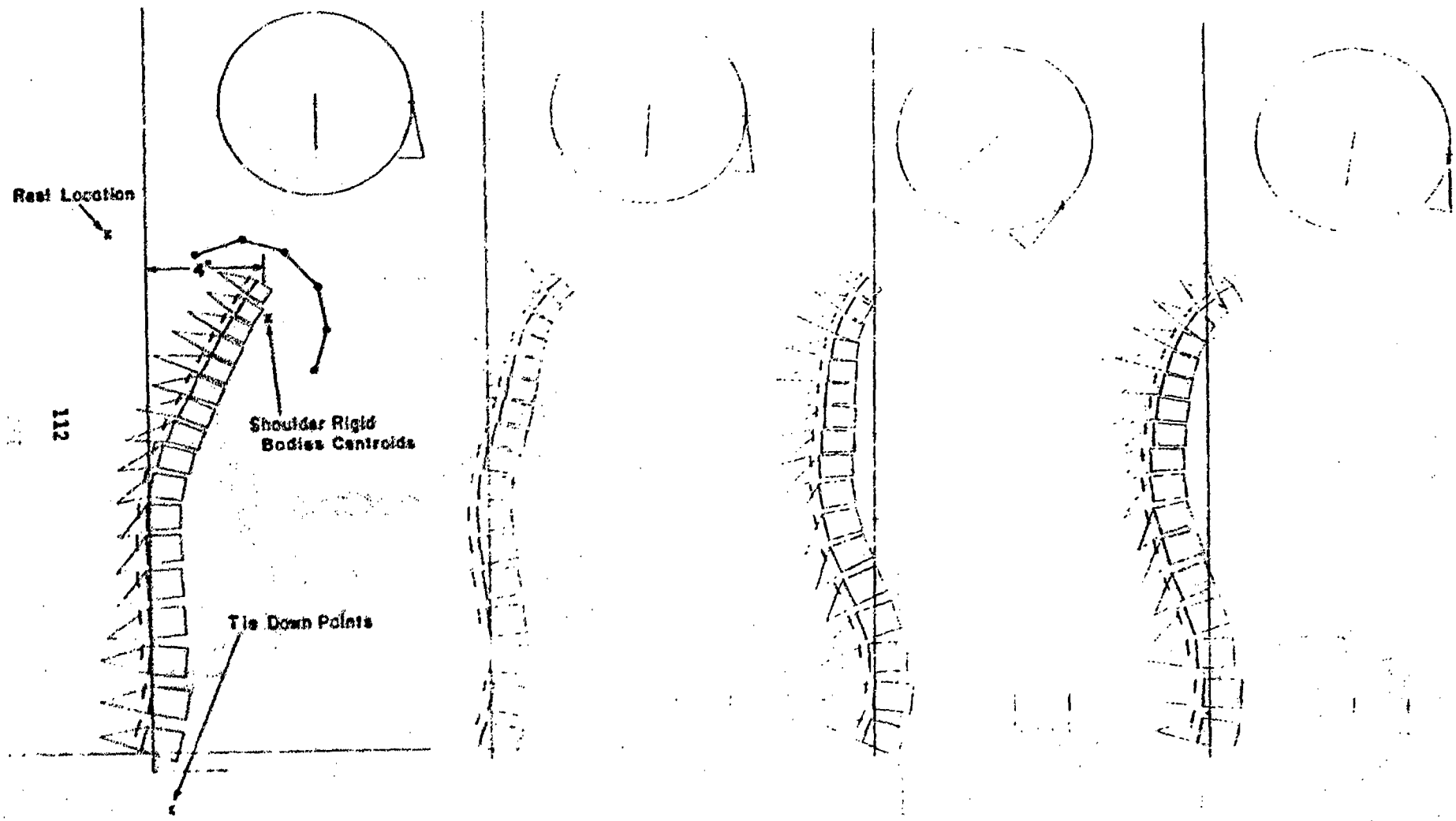

Figure 6.10. Study 1: Response of PAM4.

2.22×10^8 dynes (500 lbs) in 150 msec, for a combined belt force of 4.45×10^8 dynes (1000 lbs) at 150 msec.

The models PAM2 and PAM4 were used in this study. Figures 6.9 and 6.10 show the 0, 50, 100 and 150 msec pilot configurations for PAM2 and PAM4 respectively. Table 6.2 compares peak axial force and sagittal plane bending moment magnitudes for the neck and intervertebral discs T3/T4 and L3/L4.

VI.4.2 Study 2.

Study 2 considers a nonsymmetric initial configuration. PAM4-4 was subjected to the same pre-ejection belt force as that in Study 1. Figures 6.11 and 6.12 depict the 0, 50, 100 and 150 msec pilot configurations, sagittal and frontal plane views respectively. Two features of the model had adverse effects on the results: (1) the orientations of the shoulder rigid bodies were rotated too much initially; (2) the seatback does not offer any resistance to lateral motion of the spine because Coulomb frictional resistance is not modeled.

VI.4.3 Study 3.

Here the effects of changing the location of the reel were studied. Two runs were made, one with the reel 2.2 cm (0.9 in) below the standard height, and one with the reel 7.2 cm (2.8 in) below the standard height. The model used was PAM2 with the mass center of the head shifted slightly closer to the seatback than in Study 1. The tie down point location, belt force time history, and shoulder rigid bodies orientations were the same as in Study 1. Figures 6.13 and 6.14 show the 0, 50, 100 and 150 msec pilot configurations for the reel at 50.8 cm and 45.8 cm respectively.

VI.4.4 Study 4.

Here the effects of removal of a portion of the seatback was considered. The model used was PAM2. The reel height was 0.9 in below the standard height and the tie down point location, belt force time history and shoulder rigid bodies orien-

Table 6.2 Peak Magnitudes of Internal Forces for Pre-ejection Alighment Studies 1 to 4

Level	Reel at standard height PAM2	Reel at standard height PAM4	PAM2 Cutoff seat	PAM2 Reel 0.9 in Below Std. Ht.	PAM2 Reel 2.8 in Below Std. Ht.
Neck axial force (dynes x 10^7)	9.2	12.3	9.22	5.67	10.61
Neck sagittal plane bending moment (dyne-cm x 10^8)	2.6	3.7	7.8	1.54	4.77
T3-T1 axial force (dynes-cm x 10^7)	16.4	15.3	21.1	14.24	29.68
T3-T4 sagittal plane bending moment (dyne-cm x 10^8)	1.2	1.9	1.4	.54	.99
L3-L4 axial force (dynes x 10^7)	19.8	18.9	28.4	15.27	28.72
L3-L4 sagittal plane bending moment (dyne-cm x 10^8)	0.9	1.2	1.2	.97	1.34

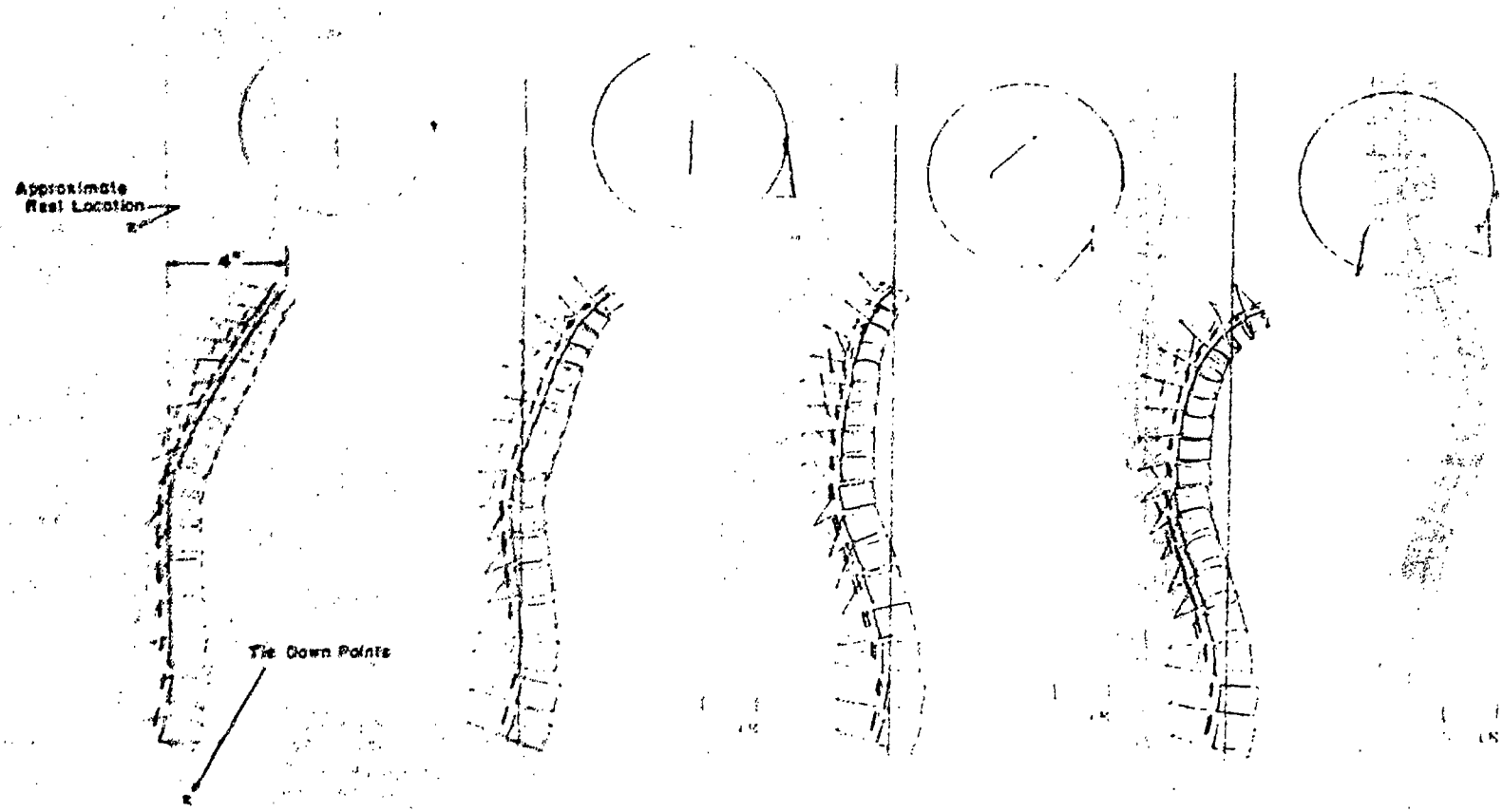

Figure 6.11. Study 2: Sagittal plane response of PAM4-4.

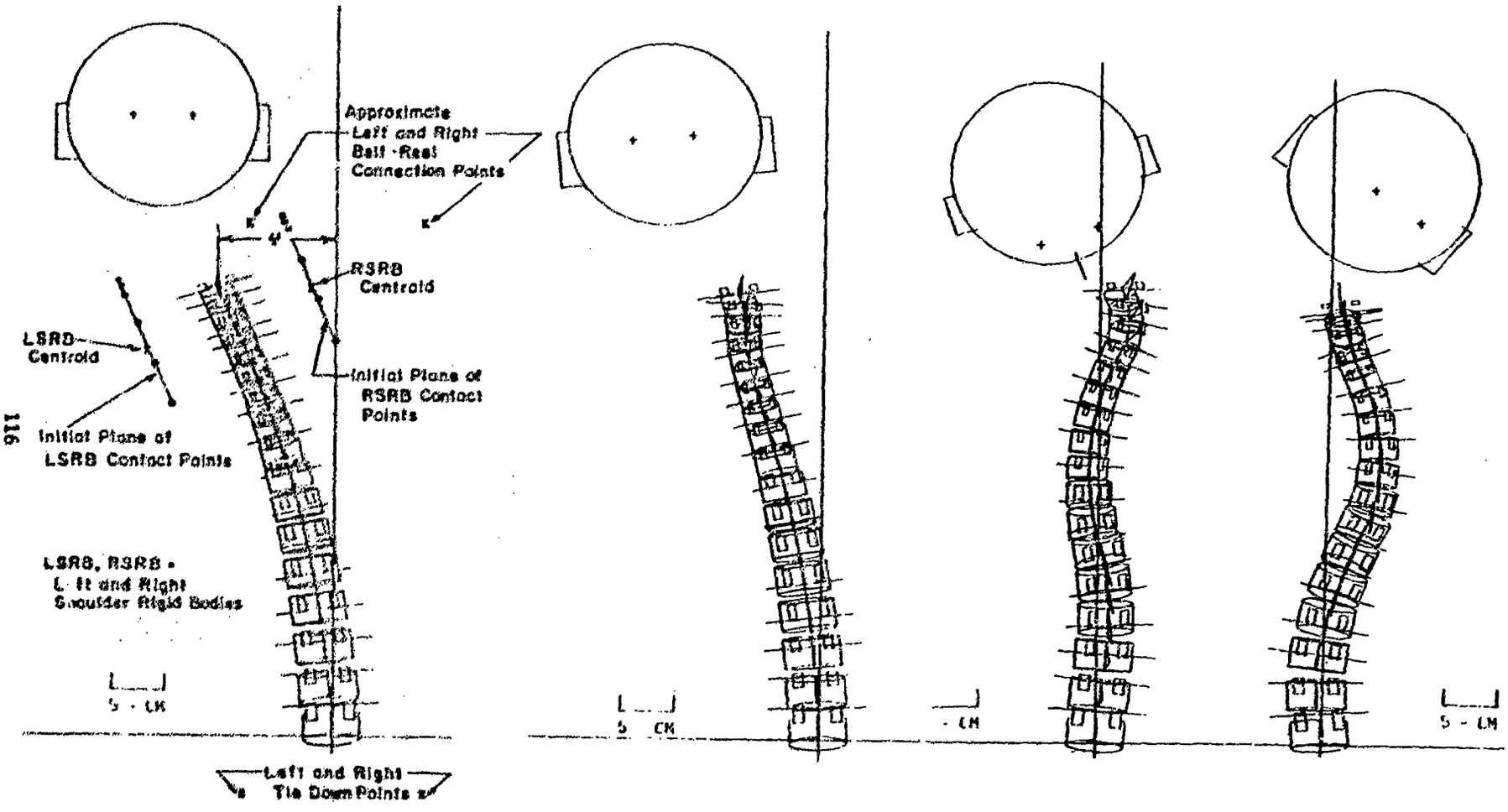

Figure 6.12. Study 2: Frontal plane response of PAM4-4.

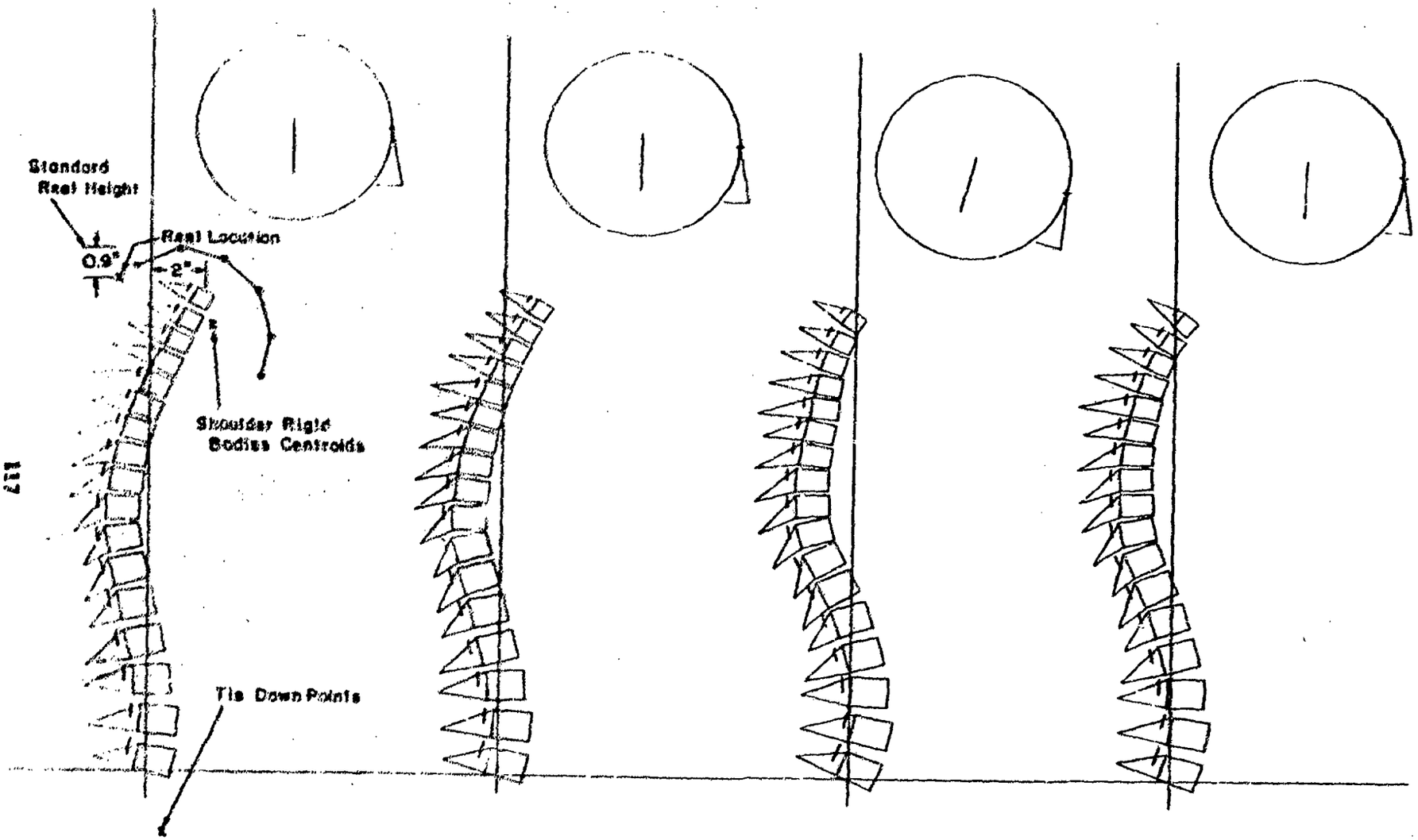

Figure 6.13. Study 3: Response of PAM2, reel height 2.2 cm below standard height.

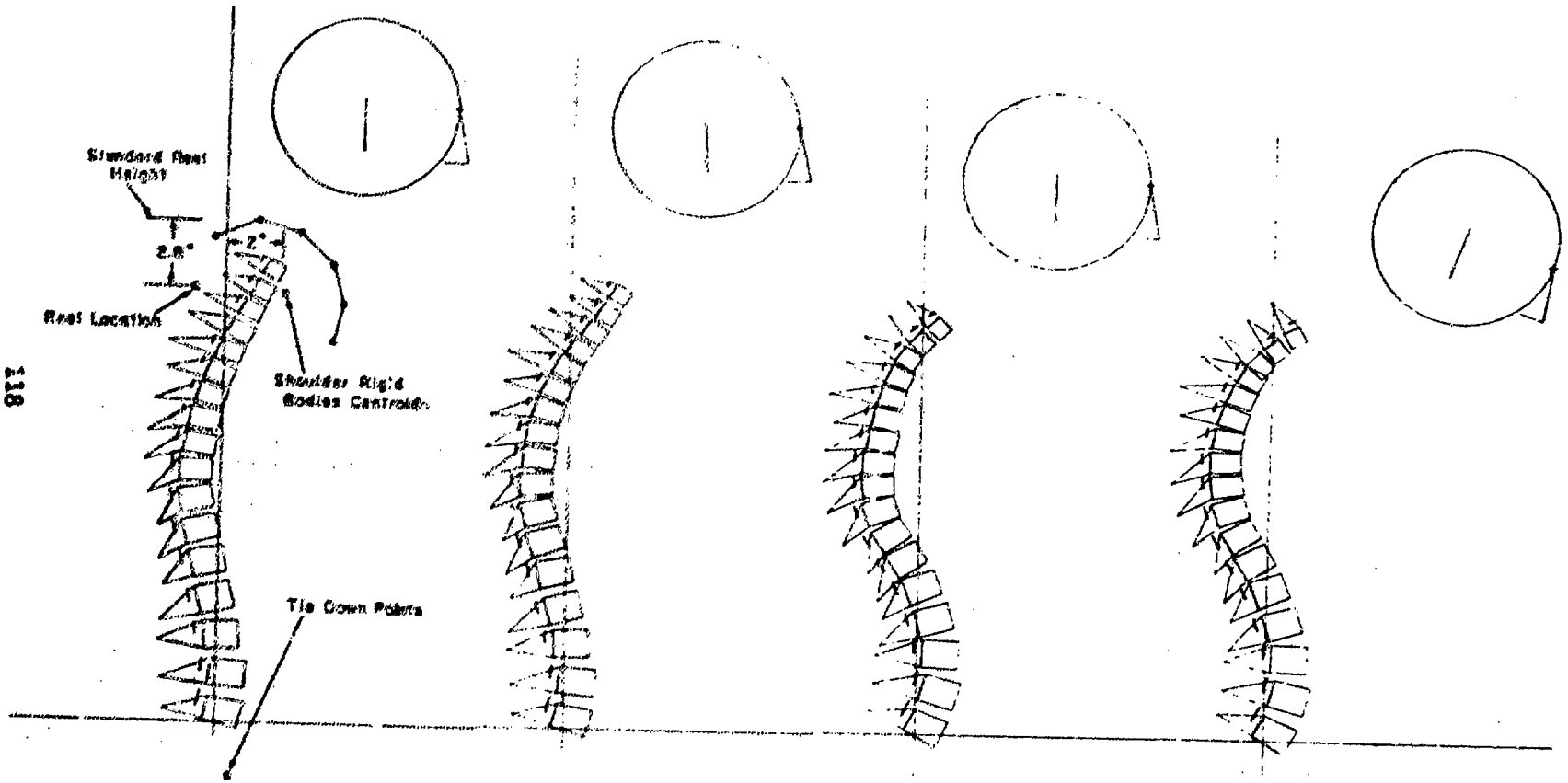

Figure 6.14. Study 3: Response of PAM2, reel height 7.2 cm below standard height.

tation were the same as in Study 1. The seatback was "cut-off" betweeen T5 and T6 so that the head and vertebral bodies T1-T5 were free. Figure 6.15 shows the 0, 50, 100 and 150 msec pilot configurations.

VI.4.5 Study 5.

In study 5, PAM4 was subjected to the belt force time history shown in Fig. 6.16. The continuous curve is that of AMRL retraction test run No. 93 for which the retraction distance was 6 in. The reel is located at the standard height and the tie down point location is the same as in the previous studies. The shoulder rigid bodies, which are aligned symmetrically with respect to the seatback, have been refined to more closely approximate the shape of the shoulders and are modeled by 7 contact points per shoulder rigid body. Although the shape of the shoulder rigid bodies is approximated as a circular segment, this shoulder rigid body is more refined than those used in the previous studies and the radius was chosen to agree with the actual physical dimensions. Figure 6.17 depicts the 0, 50, 100, 150 and 200 msec pilot configurations. Table 6.3 lists the peak axial compressive forces and sagittal plane bending moments and the approximate times at which they occur.

VI.4.6 Study 6.

In the final study, the rib cage was included, and belt interaction with both the shoulder rigid bodies and the ribs was considered to investigate the effects of belt force transmission through the rib cage. The reel and tie down point locations were the same as for study 5. The belt force time history is again that shown in Fig. 6.16. Figure 6.18 is a photograph of an initial pilot configuration used for the AMRL retraction test run No. 93 for which the retraction distance was 6 in. The initial pilot configuration used in this study, PAM6 (T1 6 in forward from its normal position, 7.7 in forward from the seatback), appears to be similar to that shown in Fig. 6.18. but the photograph only gives a rough idea of the spine's initial configuration. Figure 6.19 shows the 0, 50, 100, 150 and 200 msec pilot

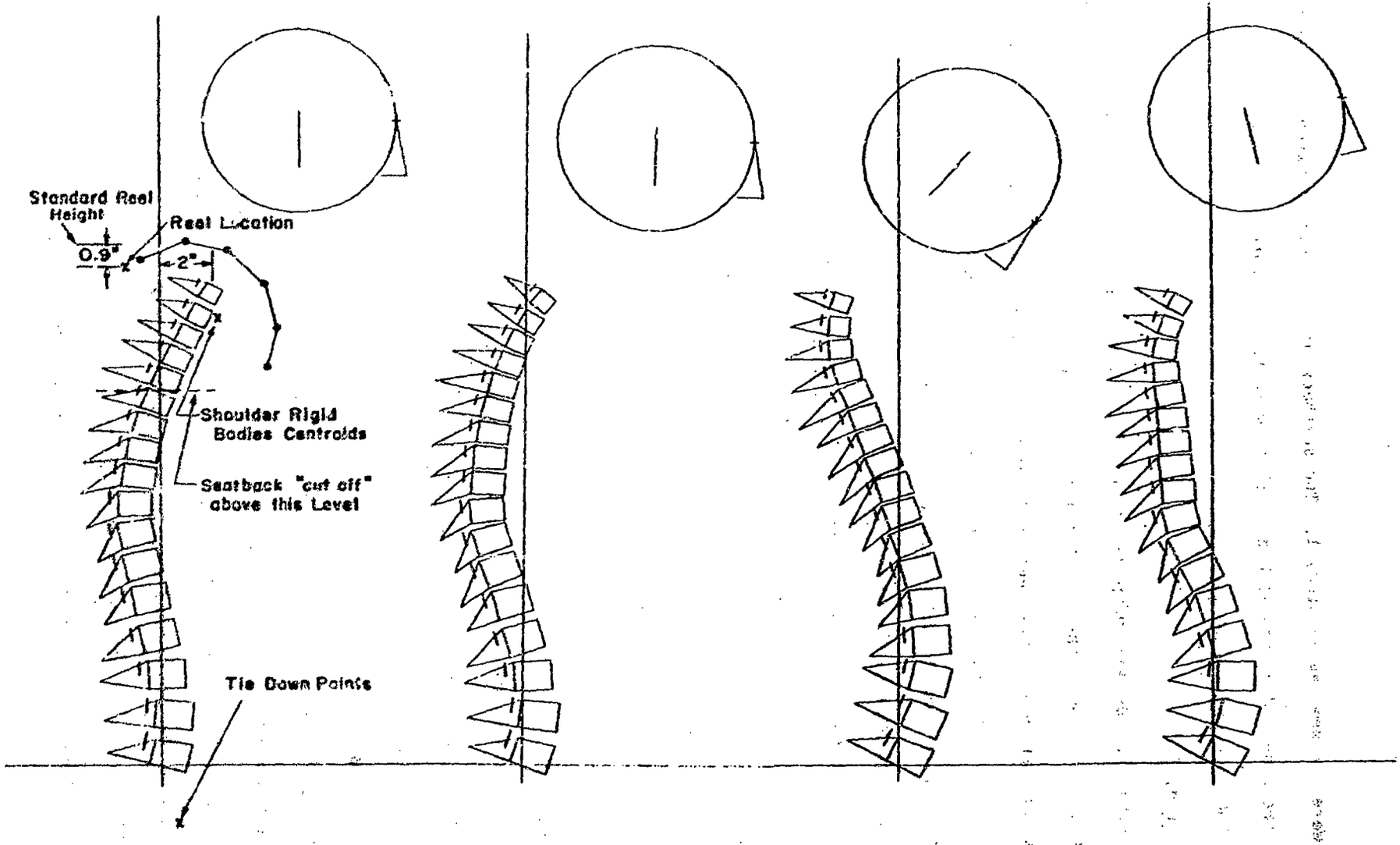

Figure 6.15. Study 4: Response of PAM2.

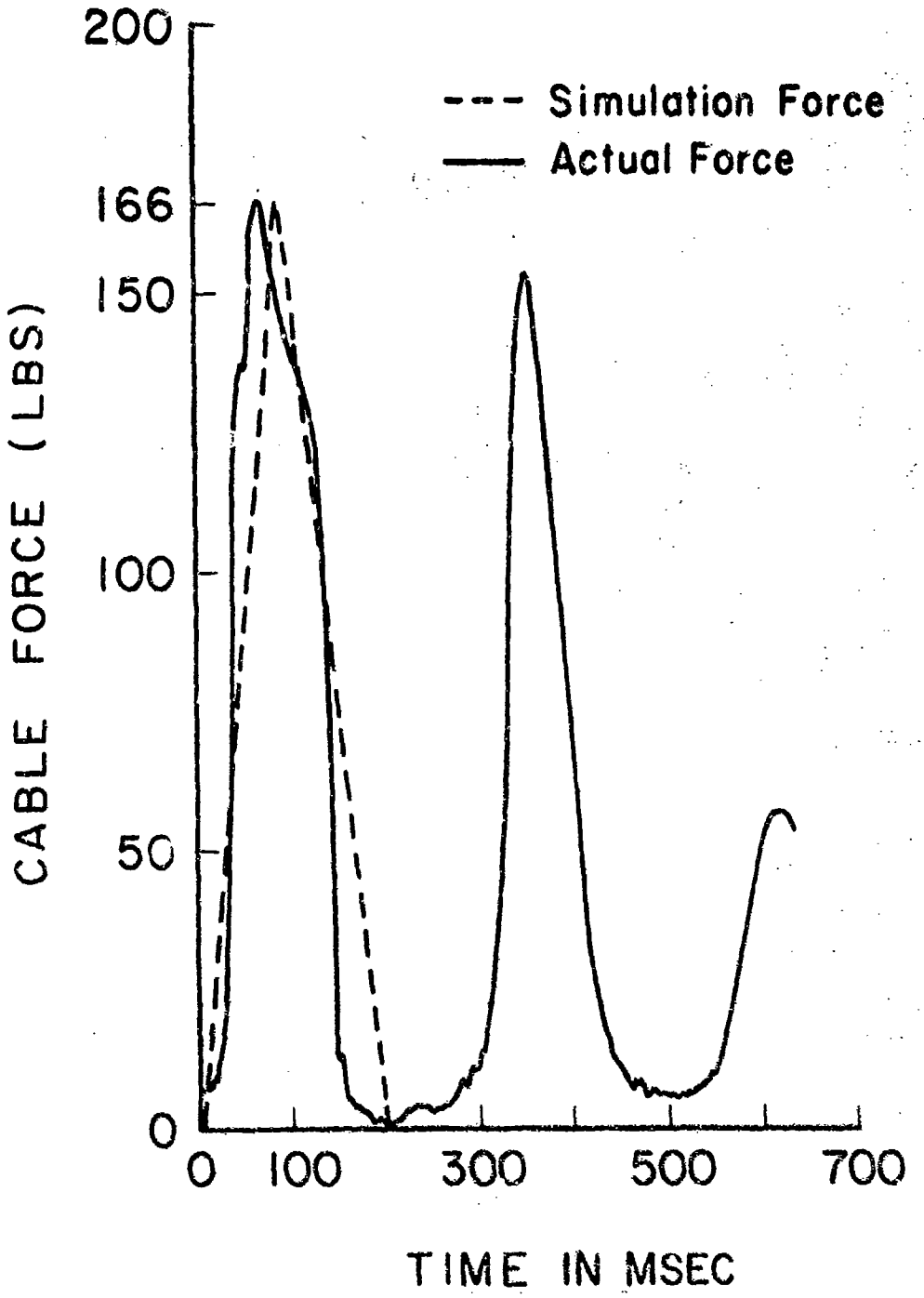

Figure 6.16. Belt force time history from AMRL retraction test run No. 93. Dashed curve is belt force time history used in Studies 5 and 6.

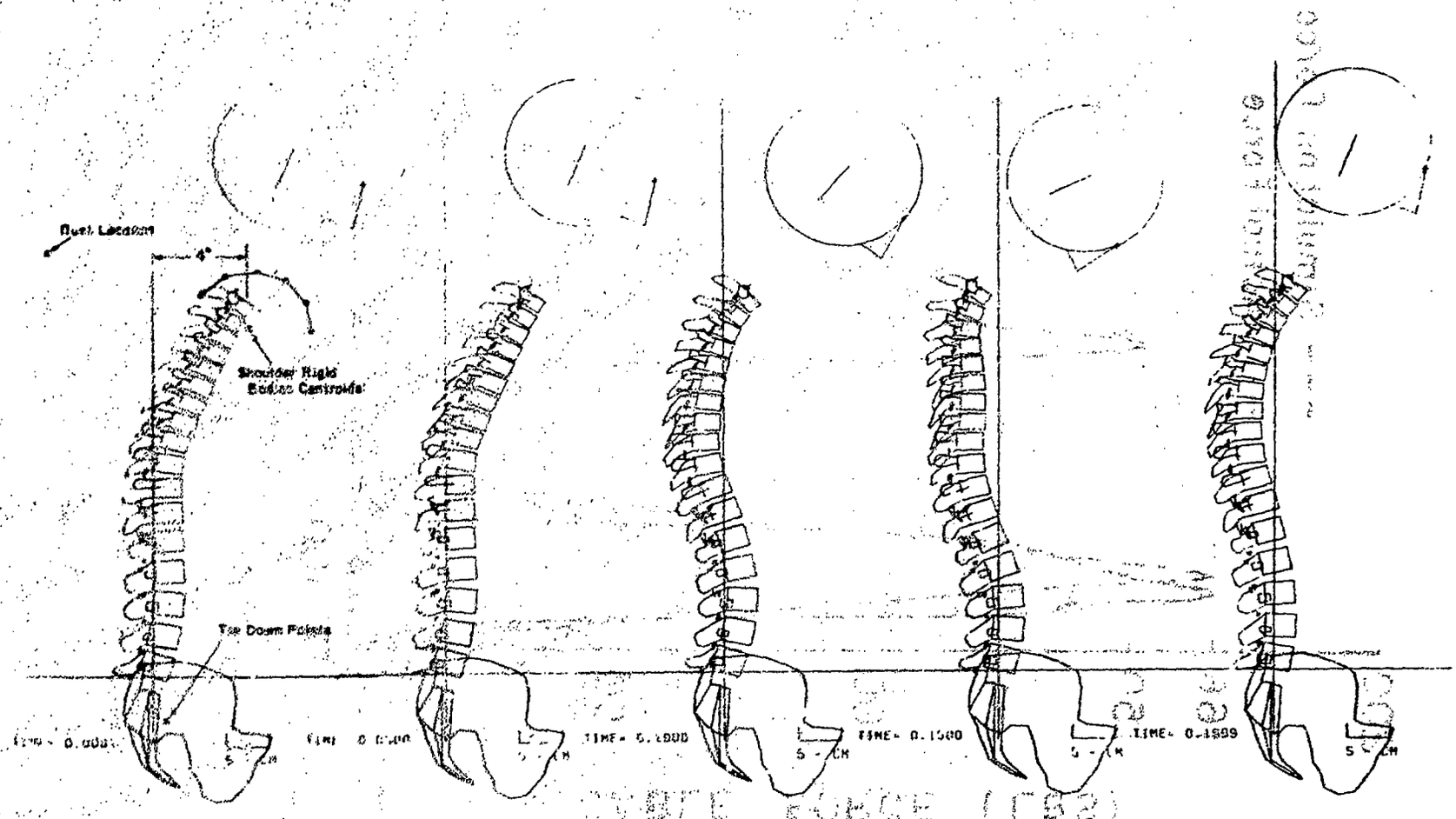

Figure 6.17. Study 3: Response of PAM4.

Table 6.3 Maximum internal forces for pre-ejection alignment study 5.

Level	Maximum force F	Time of max. force t(F)	Moment at t(F)	Maximum moment M	Time of max. moment t(M)	Force at t(M)
L5-L4	16.13	128	2	7.90	171	8
L4	15.76	126	5	9.76	142	4
L3	16.18	130	6	10.38	138	10
L2	16.77	130	6	8.23	112	4
L1	16.66	130	5	8.48	110	1
T12	14.13	128	3	7.96	110	1
T11	13.13	143	6	7.77	169	2
T10	11.56	143	1	9.34	108	1
T9	10.83	140	4	8.86	185	8
T8	9.74	140	10	9.55	138	9
T7	10.92	138	7	9.48	132	6
T6	11.06	124	8	11.59	198	0
T5	12.41	116	5	13.15	195	3
T4	11.75	111	9	11.00	108	9
T3	14.01	115	17	17.43	112	11
T2	6.98	114	12	12.91	116	6
T1	4.95	118	7	7.[illegible]9	128	5
Neck	8.45	132	32	64.89	142	5

Forces in dynes x 10^7

Moments in dyne-cm x 10^7

Time in milliseconds

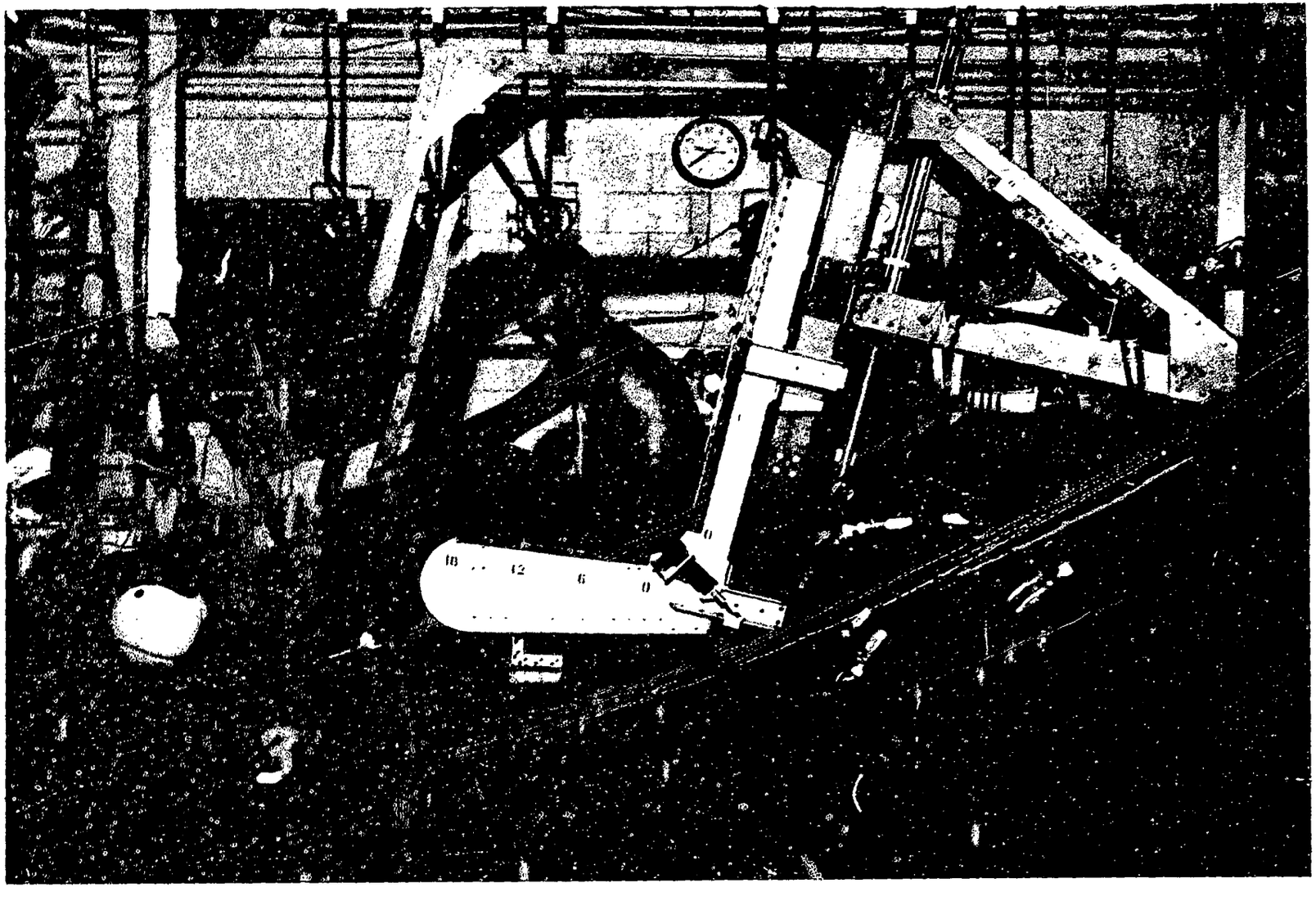

Figure 6.18. Initial pilot configuration for AMRL retraction test run No. 93. Retraction distance is 6".

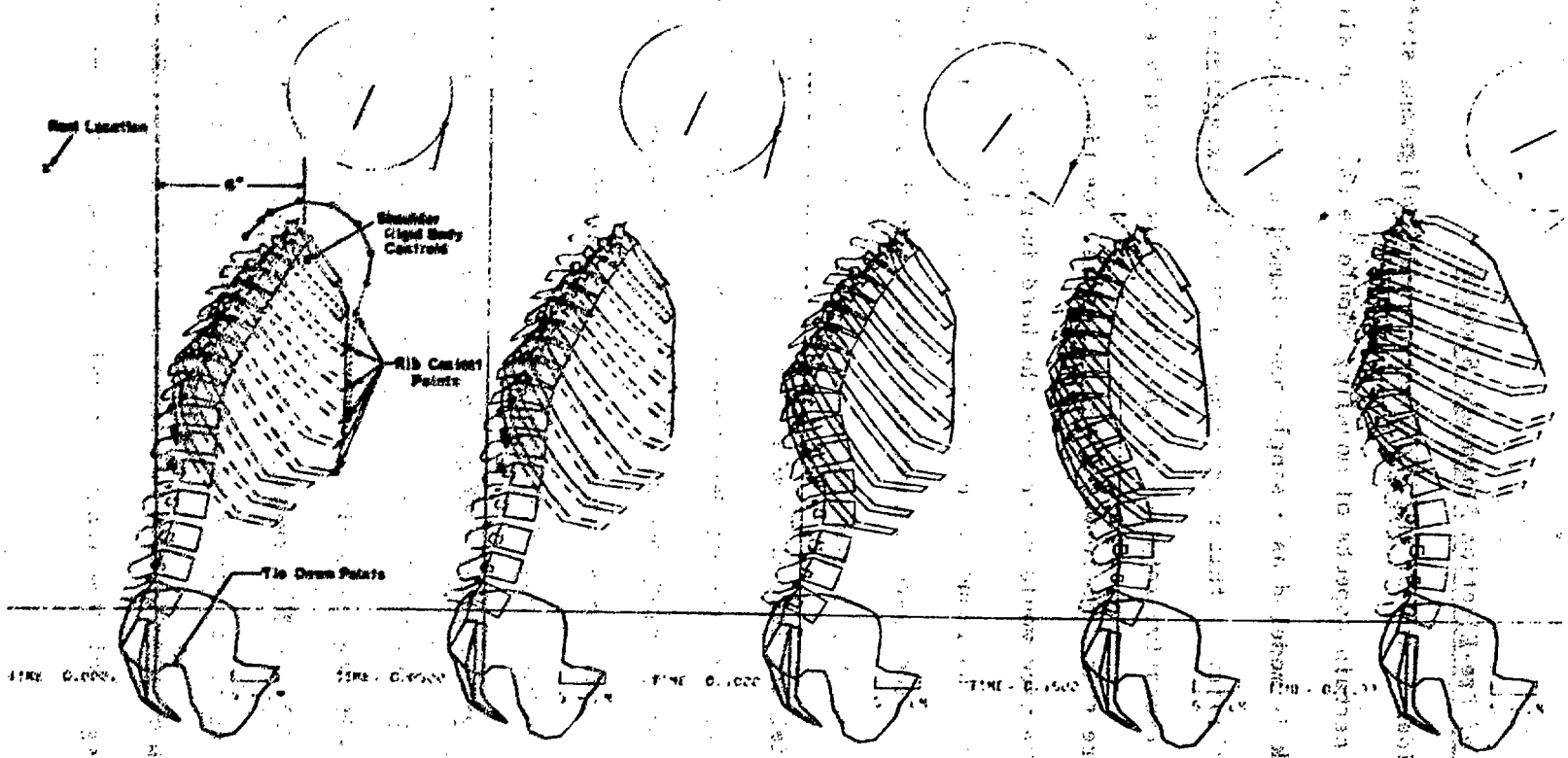

Figure 6.19. Study 6: Response of PAM6.

configurations. In Study 6, the injury potential function post processor (see Chapter IV) was available; Figure 6.20 gives the injury potential function for this study.

VI.5 Discussion of Pre-Ejection Alignment Studies

Before considering any of the pre-ejection pilot alignment studies individually, some comments on certain aspects of modeling should be made. In all of these studies, the neck is modeled as a single beam element connecting the head directly to T1. The flexibility of this neck element results in exaggerated motions of the head, leading to excessive rotation of T1. This is particularly evident for the cases with T1 more than 2 in forward from its normal position (e.g. studies 5 and 6). The muscles of the neck would distribute the head inertial effects over a larger part of the torso, thus reducing the moments at T1. Furthermore, in the earlier studies, the belt forces were transmitted through the shoulder rigid bodies only to T1, T2 and T3, further increasing forces on these vertebrae.

In the initial studies, the combined belt force was too high, because more accurate belt force time history data were not yet available. Therefore, rather than trying to predict injury potentials for studies 1-4, we concerned ourselves primarily with the gross effects observed in these studies.

It can be seen from Table 6.2, that when T1 is 4 in. forward (PAM4), the neck axial force and sagittal plane bending moment increased about 40% respectively over the 2 in forward initial configuration (PAM2). The axial forces in the T3-T4 and L3-L4 discs were affected very little. The sagittal plane bending moments at these levels increased 58% and 33%, respectively. These increases in sagittal plane bending moments can be attributed to increased inertial affects of the head-helmet mass. Comparison of the 150 msec configurations of PAM2 and PAM4 shows that the upper thoracic region of PAM4 exhibits considerably more sagittal plane curvature than PAM2.

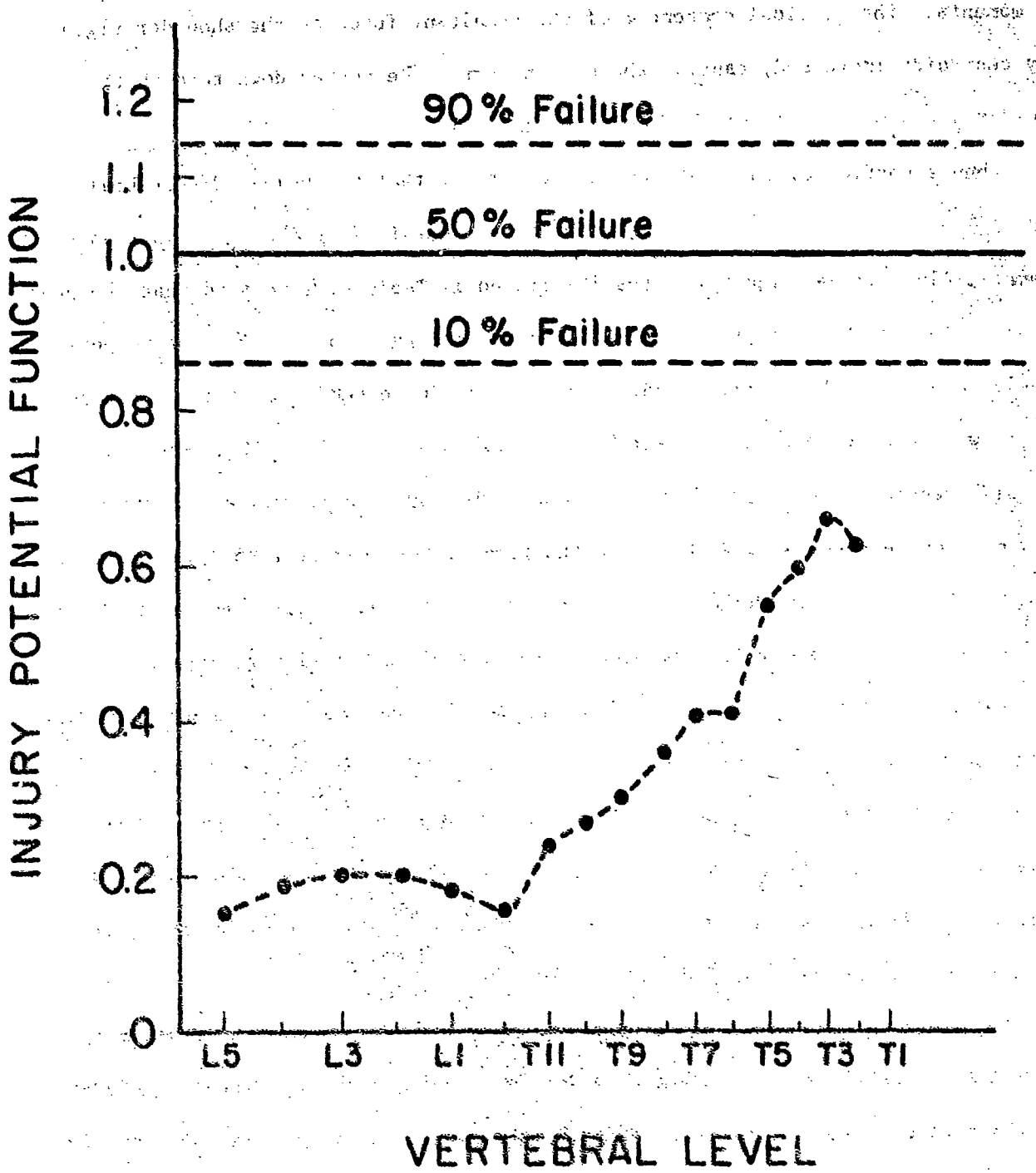

Figure 6.20. Study 6: Injury Potential Function for PAM6.

The results of Study 3, which considered the effects of varying the reel height, are presented in Figs. 6.13, and 6.14 and Table 6.2. Lowering the reel height from 0.9 in to 2.8 in results in a considerable increase in the internal axial forces and moments. The vertical component of the resultant force at the shoulder rigid body centroids increased, causing the crew member to be pushed down through the shoulder rigid bodies as well as back into the seat.

When a portion of the seatback was cut off so that the head and vertebral bodies T1-T5 do not contact it, the forces sustained by the spine increased dramatically. If we compare the results listed in Table 6.2, we find that the peak axial forces in the neck and the L3-L4 disc are increased by 63% and 86% respectively, and the peak sagittal bending moments are increased by 406% and 20% respectively when the seatback is "cut-off". The peak mid-thoracic axial forces and sagittal bending moments are increased also. The 100 msec pilot configuration, Fig. 6.15 corresponds approximately to the time of the peak neck sagittal bending moment. In this configuration, the upper thoracic region has been pulled back over the top of the seatback while the head-helmet mass is still slumped forward.

The results of Study 5, depicted in Fig. 6.17, show far less curvature of the spine because of the reduced belt force levels. This is due to the improved modeling of the shoulder rigid bodies, as well as the considerably less severe belt force time history. If we check the internal forces against the injury criteria presented in AMRL-TR-76-10, it is found that internal force levels in the spine (T1-L5) are well below injury levels.

The inertial effects of the head-helmet mass are particularly evident in the 150 and 200 msec pilot configuration of Fig. 6.19 from Study 6. Except for large forward rotations at T1, the spine appears to behave quite well. The 100 and 150 msec configurations appear to indicate large downward rotation of the rib cage relative to the spine, due to the increased curvature of the thoracic region of the

spine. This difficulty arises because there is no obstruction to downward rotation of the rib cage in PAM 6, the inclusion of the abdominal viscera in this model would limit this downward motion.

It may be of some interest to note that the 150 and 200 msec configurations of studies 5 and 6 respectively, are very similar in spinal alignment except for the larger forward rotations at T1 in Study 6. In Study 5, the belt interacted only with the shoulder while in Study 6, the belt also interacted with rib pairs R1-R7. It is observed that in both cases, the spinal configurations when the seat is contacted are similar. From Table 6.2, it can be seen that including belt interaction with the ribs has the effect of reducing the compressive forces in the lumbar region, and although the sagittal plane bending moment is somewhat increased in the lumbar region, it appears to be distributed more uniformly along the spine.

Figure 6.20 depicts the injury potential function, IPF, for Study 6. All the vertebral bodies (particularly in the lumbar region) are well below the injury level. The vertebral body T1 has not been shown because of the unrealistically high neck moment.

In summary:

1) The forces caused by pre-ejection retraction alone are not sufficient to lead to lower vertebral injuries; however it does induce curvature of the lower spine, and the studies of Belytschko, et al., (1976) have shown that increased curvature leads to increased force levels in ejection.

2) The forces and initial curvature are increased as the reel height relative to the shoulder is decreased.

3) Isolated spine models can reasonably well reproduce the results of the more complex models.

4) The forces and curvatures in the upper spine are strongly affected by the motion of the neck and spine, so improved models of the neck are needed to obtain a complete picture of the response.

CHAPTER VII

EJECTION SIMULATIONS

VII.1 Introduction and Objectives

In this Chapter we consider the response of the spine models in ejection. These studies have three objectives:

1) to evaluate the effects of various components of the model, such as the viscera and seat belt, especially with respect to the force levels in the spine and the curvature;

2) to compare the results of models which have been matched with experimental impedance data with the previous models in Belytschko, et al., (1976);

3) to compare the results obtainable from models of varying degrees of complexity, such as the simplified spine model, SSM and the complex spine model, CSM, in ejection simulations.

One of the goals of the second objective was to observe the effects of parameters which must be chosen quite arbitrarily in a simulation, such as head positions. It should be noted that some of these studies were made before our final viscera data was completed through the impedance studies.

Except where noted, the acceleration profile used in all of the studies has a rate of onset of 714 g/sec for 14 msec, and then a constant acceleration of 10 g for 66 msec, for a total duration of 80 msec. After 80 msec, the acceleration vanishes. The acceleration vector is perfectly vertical (+z) for all runs. In all cases, the problems are treated as three dimensional, although a two dimensional representation would often be adequate. The explicit integration scheme was used with a time step of 10^{-4} seconds, thus requiring 800 time steps for a solution duration of 80 msec.

VII.2 Isolated Ligamentous Spine Model

VII.2.1 Unrestrained Ligamentous Spine Model

The first two simulations involved the isolated ligamentous spine models

(ILS and ILSV from Chapter II) and considered the effects of the secondary column, which represents the ribs in the thoracic region and the viscera in the lumbar region, on the transmission of the acceleration induced forces along the spine. The seatback was included, but the restraint system was not. Table 7.1 gives the peak internal forces for the simulation without and with the secondary column; Fig. 7.1 depicts the initial and 80 msec pilot configurations for the simulation without the secondary column while Fig. 7.2 depicts the 80 msec pilot configuration with the secondary column. The initial pilot configuration was the same as in Fig. 7.1.

From Table 7.1 we can see that including the secondary column causes a slight increase in the axial compressive forces, while the sagittal plane bending moment is reduced considerably in the lumbar region and increased slightly in the mid to upper thoracic region. The secondary column is a simplified representation of the secondary path of force transmission provided by the viscera and ribs. When it is absent, the spine and its associated ligaments are the only path for the entire load. Lucas and Bresler (1961) demonstrated that the static frontal plane buckling load for an isolated ligamentous spine constrained against sagittal plane motion is 2×10^6 to 10×10^6 dynes. The sagittal plane bending stiffness is somewhat lower than the frontal plane bending stiffness due to the sagittal plane curvatures. This would indicate a lower static sagittal plane buckling load. Since the axial compressive forces transmitted along the spine during an ejection simulation are several orders of magnitude greater than the frontal plane static buckling load as determined by Lucas and Bresler (1961) one would expect a response such as depicted in Fig. 7.2 when the secondary path of load transmission is not included.

One result that may appear contradictory at first is that the axial load is reduced when the secondary column is not included. However in the absence of a secondary column, the vertical acceleration of the head and upper torso are reduced

Table 7.1 Comparison of peak internal forces for ejection simulations with and without secondary column (no restraint system)

Level[1]	Axial force dynes 5 x 10^8		Moment dyne-cm x 10^7	
	without	with	without	with
L5	-2.92	-3.41	-23.80	-6.48
L4	-2.46	-2.76	20.60	18.76
L3	-2.34	-2.87	47.60	28.18
L2	-2.07	-2.75	57.87	25.96
L1	-2.03	-2.40	36.45	22.56
T12	-1.91	-2.27	-14.12	15.78
T11	-1.79	-2.53	-23.43	-17.45
T10	-1.70	-2.28	-35.80	-22.00
T9	-2.06	-1.84	-34.99	-25.02
T8	-1.58	-1.95	-25.70	-27.90
T7	-1.38	-1.87	-18.91	-25.96
T6	-1.27	-1.47	-9.89	-22.78
T5	-1.23	-1.25	-3.63	-12.49
T4	-1.17	-1.19	3.10	8.39
T3	-1.02	-1.04	7.66	10.21
T2	-1.05	-1.06	6.57	11.03
T1	-0.80	-0.91	7.29	8.14
Neck	-0.86	-0.86	-9.86	-9.98

[1] Refers to disc below designated vertebral level

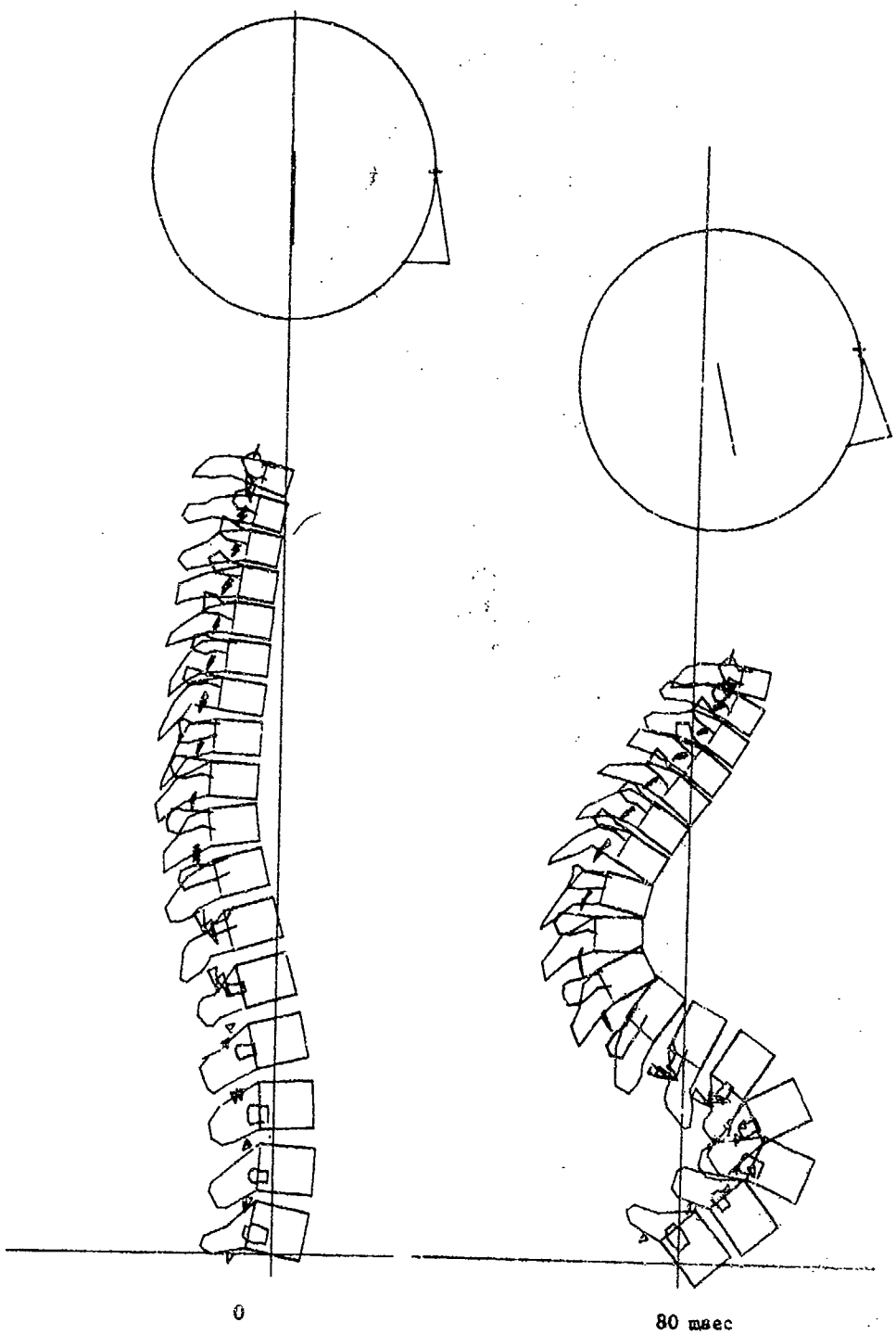

Figure 7.1. Initial and 80 msec pilot configurations for ejection simulation of ILS without secondary column and restraining system.

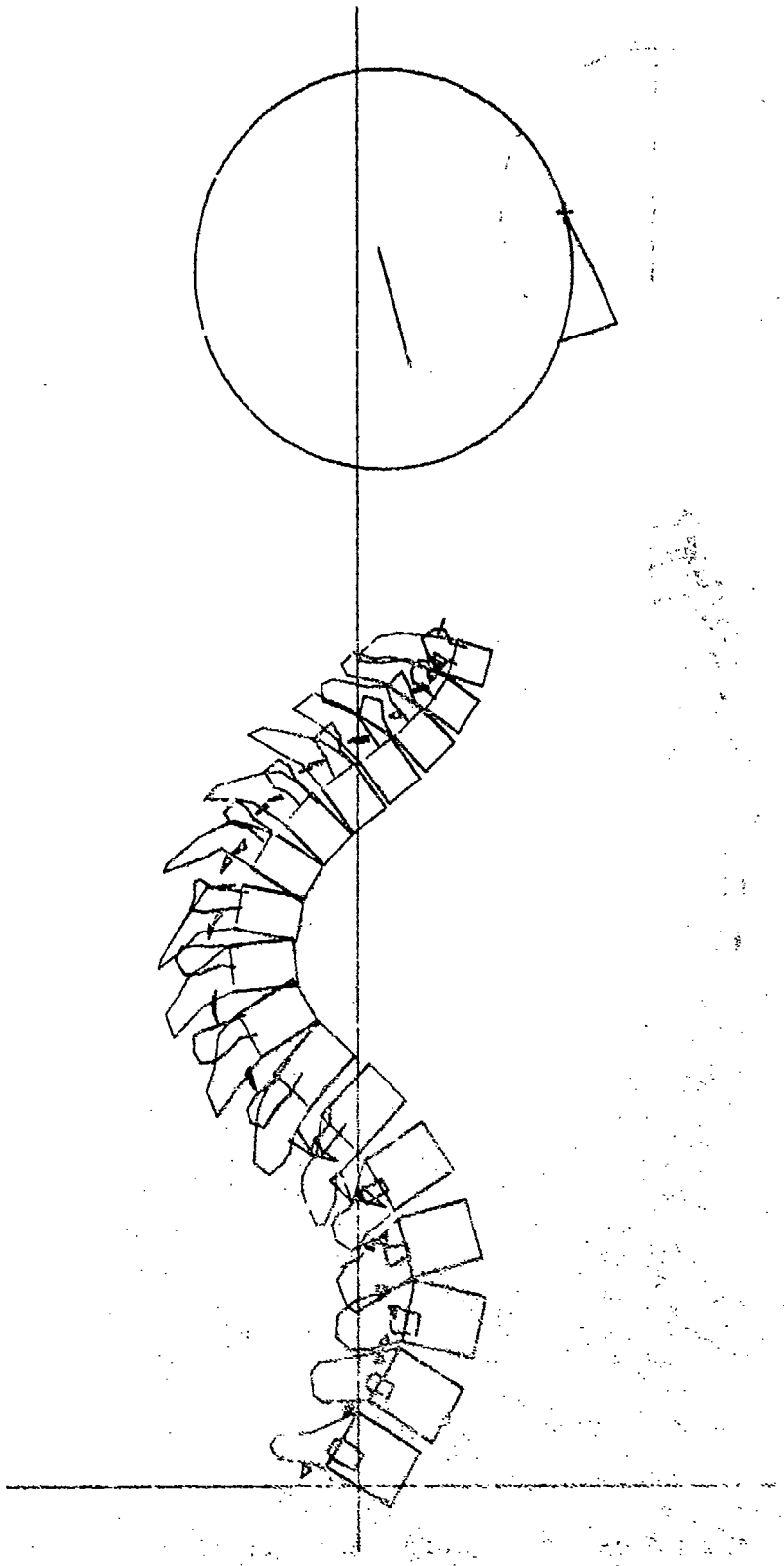

Figure 7.2. 80 msec pilot configuration for ejection simulation of ILS with secondary column; without restraining system.

considerably in the first 80 msec because the excessively flexible spine acts as a "shock" absorber. Thus, while the secondary column carries a significant part of the load if the upper torso is constrained, its net effect is to increase the axial load for an unrestrained simulation.

VII.2.2 Effects of Restraint System

To observe the effects of a harness and seatbelt on the response of the ILS model (with the secondary column), an ejection was simulated with the harness modeled as tensile springs from the seatback to T1, T2 and T3 and the seatbelt as a tensile spring from the seatback to the pelvis. This simulation was run for 3200 time steps for a duration of 320 msec. Table 7.2 lists the peak internal forces and Figs. 7.3 and 7.4 depict the 0, 40, 60, 80 and 120, 160, 240, 320 msec pilot configurations.

As expected, the restraint system has very little effect on the axial forces since it serves primarily to reduce lateral motion. The sagittal plane bending moment is almost unchanged in the lumbar region, but is reduced considerably in the thoracic region (e.g. reductions of 19%, 38% and 51% at T9, T5 and T1, respectively during the first 80 msec). The seatbelt, as modeled, appears to have no observable effect on the response.

It is noteworthy that some of the peak forces occur after the seat acceleration goes to zero. For convenience, we will refer to the first 80 msec and the remaining 240 msec of the simulation as ΔT_1 and ΔT_2, respectively. During ΔT_2 the axial forces become positive, indicating that a tensile wave is induced by the seat acceleration dropping off to zero. The peak sagittal plane bending moment magnitudes at levels L5, T6 to T1 and the neck occur during ΔT_2. For T6 to T3, these values are an average of approximately 100% greater than the respective peaks during ΔT_1. The peak neck moment during ΔT_2 is approximately 4.6 times that during ΔT_1. If we take the moment in T1 to be given approximately by the average of the moments in the T1-T2 disc and the neck, this would yield values of 4.92×10^7 and 16.98×10^7 dyne-cm

Table 7.2 Peak internal forces for 320 msec ejection simulation of ILS model with secondary column and restraint system.

Level[1]	Axial Force dynes x 10^8	Moment dyne-cm x 10^9 ΔT_1	ΔT_2
L5	-3.41	-8.34	-9.82
L4	-2.75	18.77	
L3	-2.87	28.09	
L2	-2.63	25.98	
L1	-2.29	22.54	
T12	-2.25	18.27	
T11	-2.52	-17.26	
T10	-2.25	-20.93	
T9	-1.80	-20.36	
T8	-1.76	-18.23	
T7	-1.75	-15.55	
T6	-1.37	5.70	12.61
T5	-1.29	7.70	12.71
T4	-1.15	6.60	12.81
T3	-0.83	-3.72	-8.55
T2	-1.17	-5.43	-6.94
T1	-1.15	-3.64	-5.49
Neck	-1.05	6.20	28.46

[1] Refers to disc below designated vertebral level

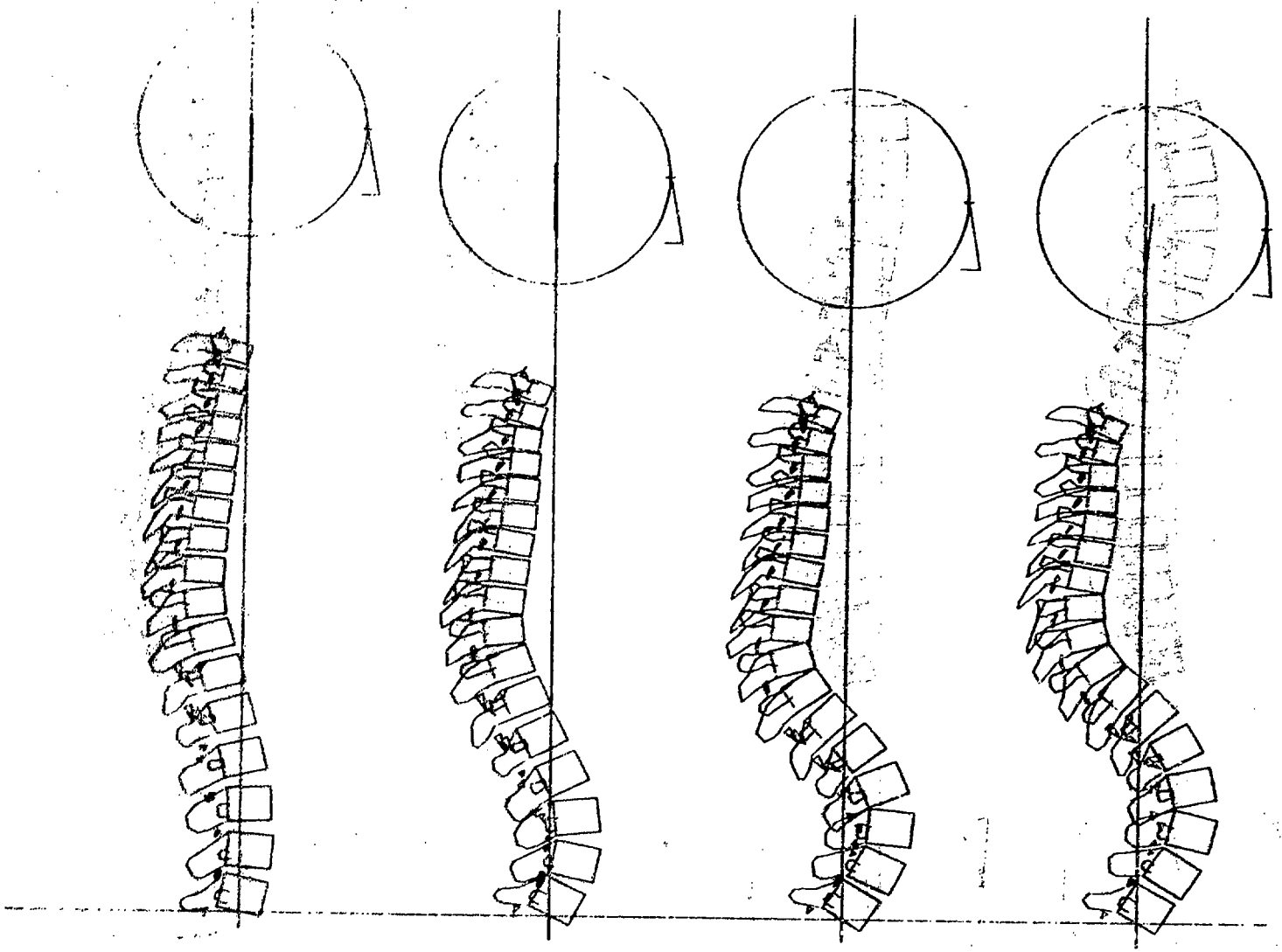

Figure 7.3. Configurations at 0, 40, 60 and 80 msec for ejection of ILS with restraint system.

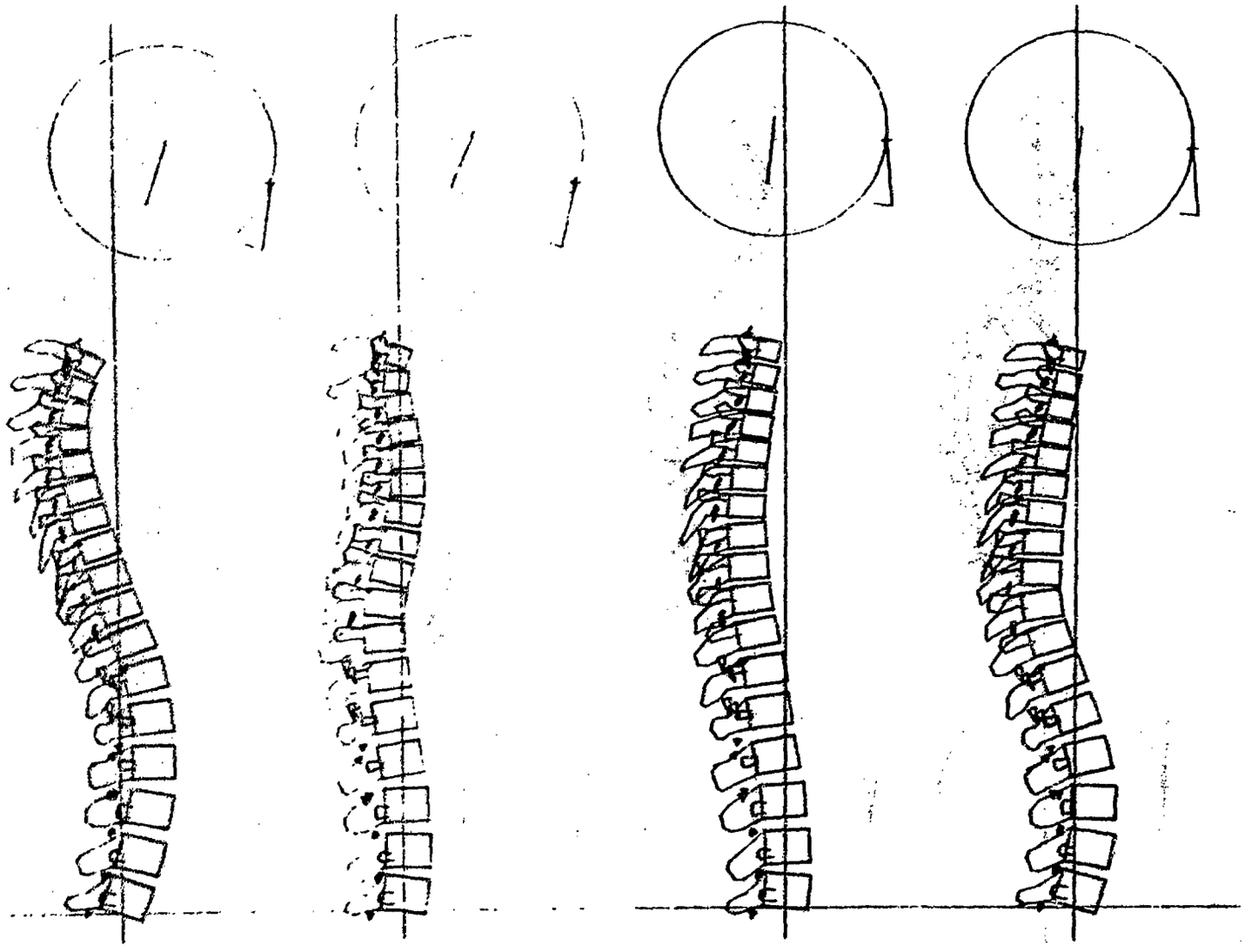

Figure 7.4. Configurations at 120, 160, 240 and 320 msec for ejection of ILS with restraint system.

for ΔT_1 and ΔT_2 respectively, or an increase of 350%.

Assessing these results with the injury criterion indicates that although the combined moment and axial force stresses for those levels discussed above are below the failure values for the entire duration, at T1 the possibility of injury is quite high. It must be kept in mind however, that in this model the neck is modeled as a single beam element between the head and T1 and considers neither the effects of the soft tissues nor the muscles, which would most likely serve to reduce the magnitude of the neck moment transmitted to T1. The modeling of the harness by springs connected directly to T1, T2 and T3 also fails to account for the much less severe distribution of restraining forces through the shoulders and rib cage and associated soft tissues. A larger amount of damping in the model would also lower the force levels during ΔT_2. This simulation demonstrates that the introduction of a restraining system decreases the flexural response of the Isolated Ligamentous Spine during ejection, and permits the pilot to remain upright. The larger duration time allowed for observance of longitudinal and flexural frequencies of 18 and 10 Hz respectively.

VII.2.3 Increased Lumbar Stiffness

Belytschko et al., (1976) noted that if the preloaded state resulting from body weight is taken to be the reference point, a linear approximation to a lumbar disc load deflection curve (above the preloaded state) results in a larger stiffness than from the unloaded state by approximately 33%. The previous simulations did not reflect this value, so a run was made with the ILS model in which the axial and bending stiffnesses of the lumbar intervertebral discs were multiplied by 1.333. The simulation was the same as that previously described except for the increased lumbar disc stiffness; the duration of the simulation is 80 msec.

It was determined that the change in the axial force peak magnitudes is essentially negligible while the peak sagittal plane bending moment magnitude is primarily

increased in the lumbar region by an average of approximately 20% for L1 to L5, while the spine configurations were unchanged. Thus increasing the lumbar stiffness by 33% had negligible effect on the spinal response. During this simulation, the maximum combined force in the spring elements representing the shoulder harness was approximately 1.65×10^8 dynes (370 lbs).

VII.3 Ligamentous Spine with Ribs and Hydrodynamic Visceral Representation

VII.3.1 Normal Configuration

A 10 G_z ejection simulation with acceleration profile and restraint system as described in Section VII.2 was run with the ligamentous spine with ribs and hydrodynamic visceral representation (CSM from Chapter II). Table 7.3 gives the peak internal forces, the peak visceral pressures, and the peak harness forces respectively. Fig. 7.5 depicts the initial, 40, 60 and 80 msec pilot configurations respectively.

This simulation was exactly the same as the one in Section VII.2 (for the first 80 msec) for which the results are given in Table 7.2 and Fig. 7.3. Comparing Tables 7.2 and 7.3, a small increase in the axial force is noted. The peak sagittal plane bending moments show considerable reductions. In the lumbar and thoracic regions and the neck, they are reduced by averages of 65%, 52% and 21% respectively. As can be seen from the 60 and 80 msec pilot configurations, Figs. 7.3 and 7.5, the curvature of the lumber region is less for the hydrodynamic visceral representation than for the secondary column representation.

Table 7.3 indicates a variation in peak pressure values from 4.96×10^5 dyne/cm^2 in the lower portion (PELVIS-L5) of the viscera model to 2.51×10^5 dyne/cm^2 in the upper portion (L3 to the bottom of rib pair 10). Morris, et al., (1961), using interabdominal pressure transducers, determined an abdominal pressure of 2×10^5 dyne/cm^2 during weight lifting experiments. In a dynamic environment, we can expect response magnitudes of up to twice the corresponding static pressure. Hence,

Table 7.3 Peak internal forces for ejection simulation of the CSM

Level[1]	Axial force dynes x 10^8	Moment dyne-cm x 10^9
L5	-3.23	-1.82
L4	-3.00	7.85
L3	-3.00	10.69
L2	-2.92	9.80
L1	-2.67	8.56
T12	-2.50	6.69
T11	-2.49	-8.41
T10	-2.44	-9.93
T9	-2.28	-9.65
T8	-2.39	-11.67
T7	-1.95	-7.79
T6	-1.77	3.12
T5	1.34	2.31
T4	-1.50	3.05
T3	-1.03	-2.95
T2	-1.39	-2.46
T1	-1.21	1.21
Neck	2.12	4.89

Level	Pressure (dyne/cm^2 x 10^5
Lower(Pelvis - L5)	-4.96
Middle (L5-L3)	-4.06
Upper (L3-bottom of rib pair 10)	-2.51

Level		Force (dynes x 10^7)
Pelvis (seatbelt)		6.87
T3	(harness)	4.91
T2	(harness)	3.10
T1	(harness)	1.51

[1] Refers to disc below designated vertebral level

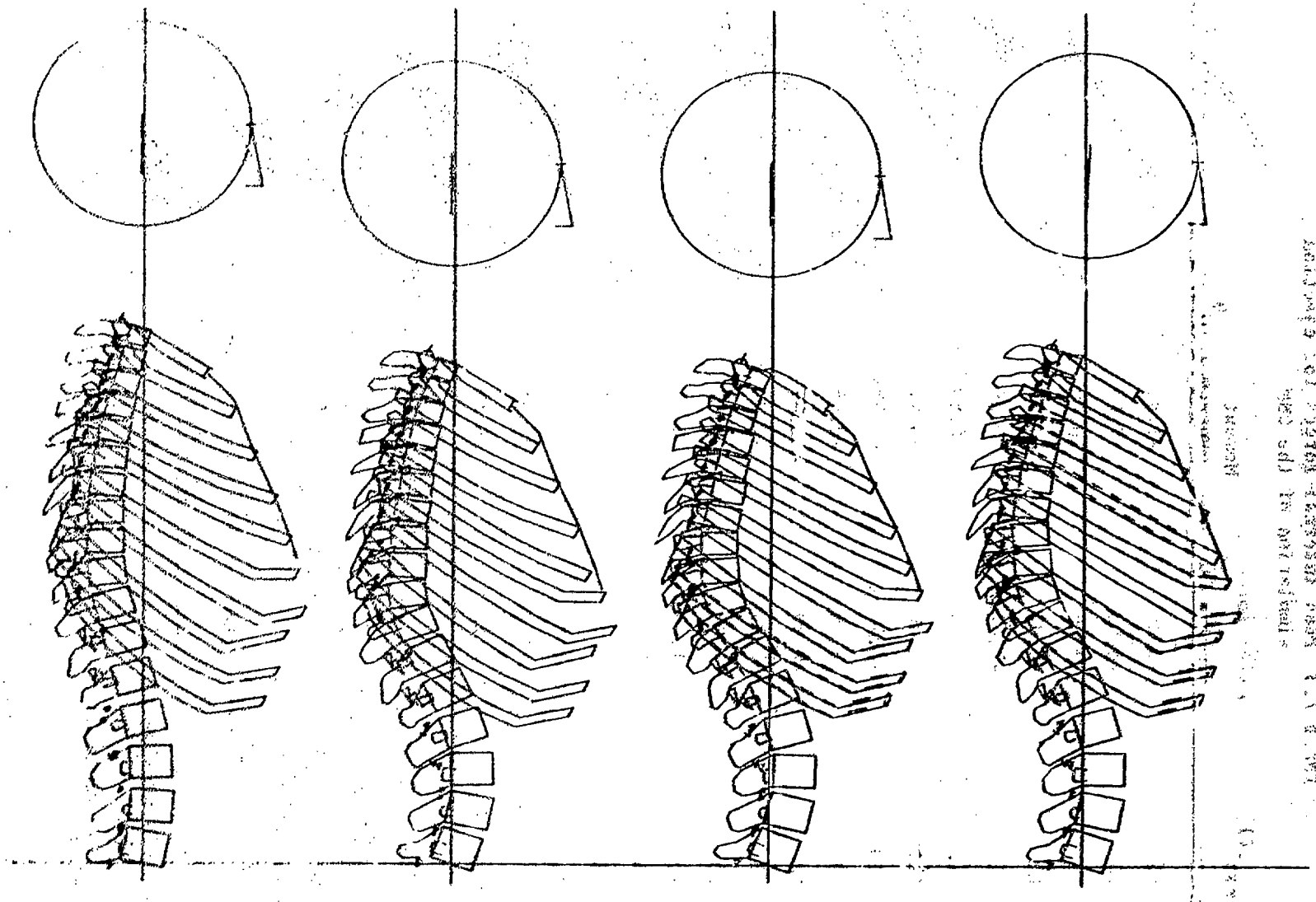

Figure 7.5. Configurations at 0, 40, 60 and 80 msec for ejection of CSM (normal configuration).

comparison with the Morris, et al. result indicates the peak visceral pressure values observed in this simulation are reasonable. The combined peak harness force is 9.52×10^7 dynes (214 lbs) in this simulation.

VII.3.2 Effect of Variation in Harness Location

In the previous simulations, the harness was attached to the seatback at the undeformed height of T1. To see how a change in reel height affects the response, an ejection was simulated with the initial reel height at the undeformed height of T4, thus lowering the reel height by 6.3 cm (2.5 in). Table 7.4 gives the peak internal forces, the peak visceral pressures, and the peak harness forces respectively. Figure 7.6 depicts the initial, 40, 60 and 80 msec pilot configurations, respectively.

Comparing the results listed in Tables 7.3 and 7.4 indicates that lowering the reel height from T1 to T4 has the following effects: the axial forces in the lumbar and thoracic regions are increased slightly while the axial force in the neck shows a small reduction; the peak sagittal plane bending moments undergo negligible change in the lumbar and lower thoracic region but increase an average of 70% from T8-T4, decrease by 40% at T3 and T2, and increase by 80% and 100% at T1 and the neck respectively.

The peak visceral pressures and the total peak harness force show very little change, although lowering the reel did change the distribution of the harness force.

VII.3.3 Variation in Head/Helmet Mass Center Location

To observe the effects of change in the head-helmet mass center on the internal force response, an ejection was simulated with the head-helmet mass center moved forward from its normal location by 4 in. The simulation time was 80 sec.

Table 7.5 lists the peak internal forces and visceral pressures. Figure 7.7 depicts the 0, 40, 60 and 80 msec pilot configurations. Figures 7.8 and 7.9 show

Table 7.4 Peak internal forces for ejection simulation of CSM with reel located at the initial level of T4.

Level[1]	Axial force dyne x 10^8	Moment dyne-cm x 10^9
L5	-3.31	-1.67
L4	-3.10	7.81
L3	-3.07	10.85
L2	-2.95	10.02
L1	-2.79	8.58
T12	-2.69	6.70
T11	-2.53	-8.43
T10	-2.54	-10.08
T9	-2.42	-8.65
T8	-2.70	-13.01
T7	-2.34	-9.83
T6	-2.10	-6.36
T5	-1.76	-6.48
T4	-1.74	-3.96
T3	-1.34	-1.51
T2	-1.44	1.58
T1	-1.19	2.22
Neck	-1.04	9.93

Level	Pressure (dyne/cm^2 x 10^5)
Lower (Pelvis - L5)	-5.26
Middle (L5-L3)	-4.38
Upper (L3-bottom of rib pair 10)	-2.57

Level	Restraining force (dynes x 10^7)
Pelvis (seatbelt)	9.69
T3 (harness)	
T2 (harness)	0.57
T1 (harness)	3.30
	4.91

[1] Refers to disc below designated vertebral level

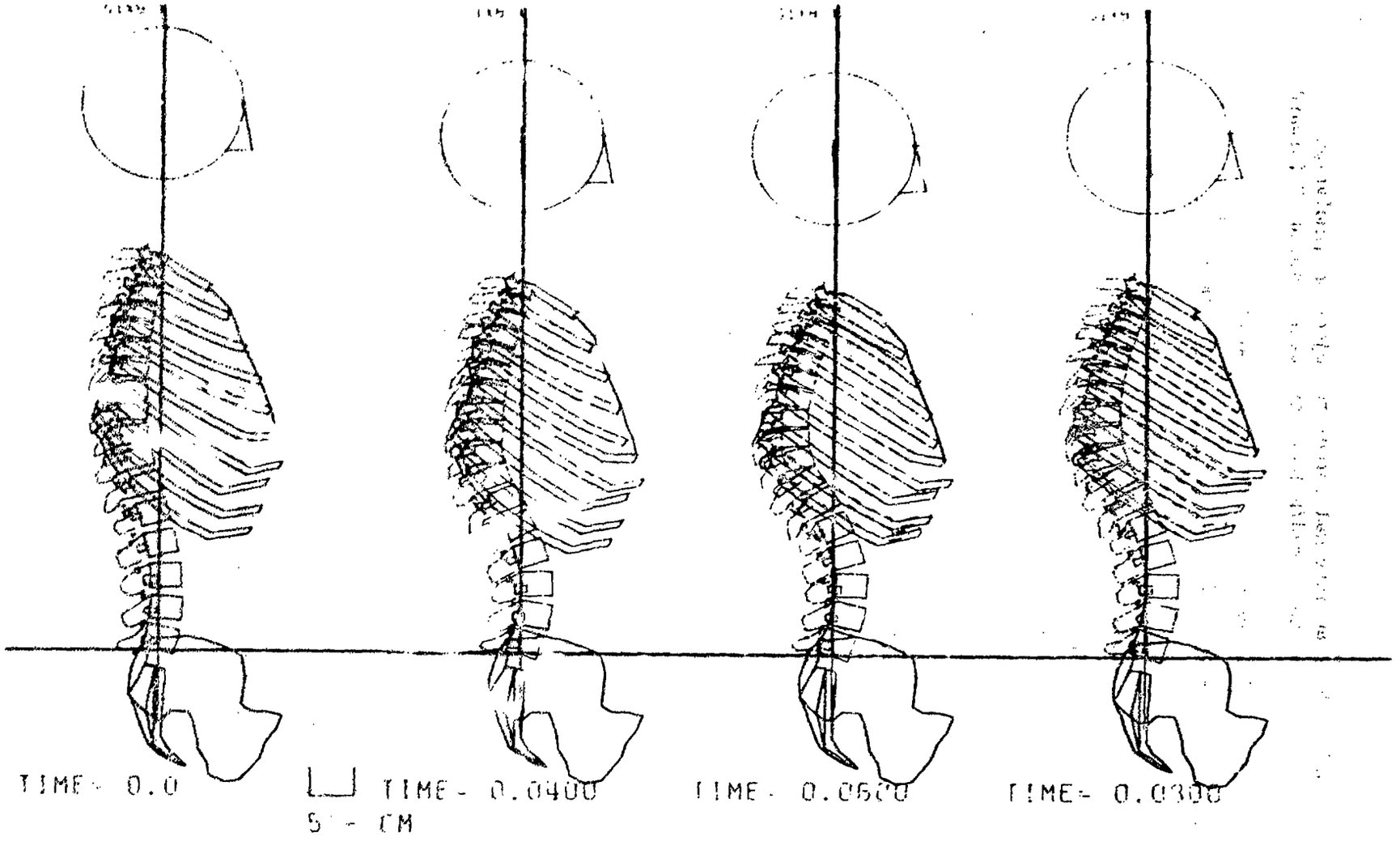

Figure 7.6. Initial, 40, 60 and 80 msec pilot configurations from ejection simulation of CSM with initial reel height at undeformed level of T4.

Table 7.5 Peak internal forces for ejection simulation of CSM, head/helmet mass center moved 4" forward

Level[1]	Axial force dynes x 10^8	Moment dyne-cm x 10^8
L5	-3.25	4.09
L4	-2.99	7.98
L3	-3.00	10.56
L2	-2.88	9.63
L1	-2.62	8.22
T12	-2.46	-7.42
T11	-2.47	-8.51
T10	-2.41	-10.10
T9	-2.18	-8.67
T8	-2.33	-11.73
T7	-1.88	-8.18
T6	-1.67	-8.89
T5	-1.33	-6.80
T4	-1.36	-6.41
T3	-1.14	-5.69
T2	-1.06	-9.11
T1	-0.88	-10.00
Neck	-0.80	-39.72

Level	Viscoral Pressure (dyne/cm^2 x 10^5)
Lower (Pelvis - L5)	-5.02
Middle (L5-L3)	-4.56
Upper (L3-bottom of rib pair 10)	-2.67

[1] Refers to disc below designated vertebral level

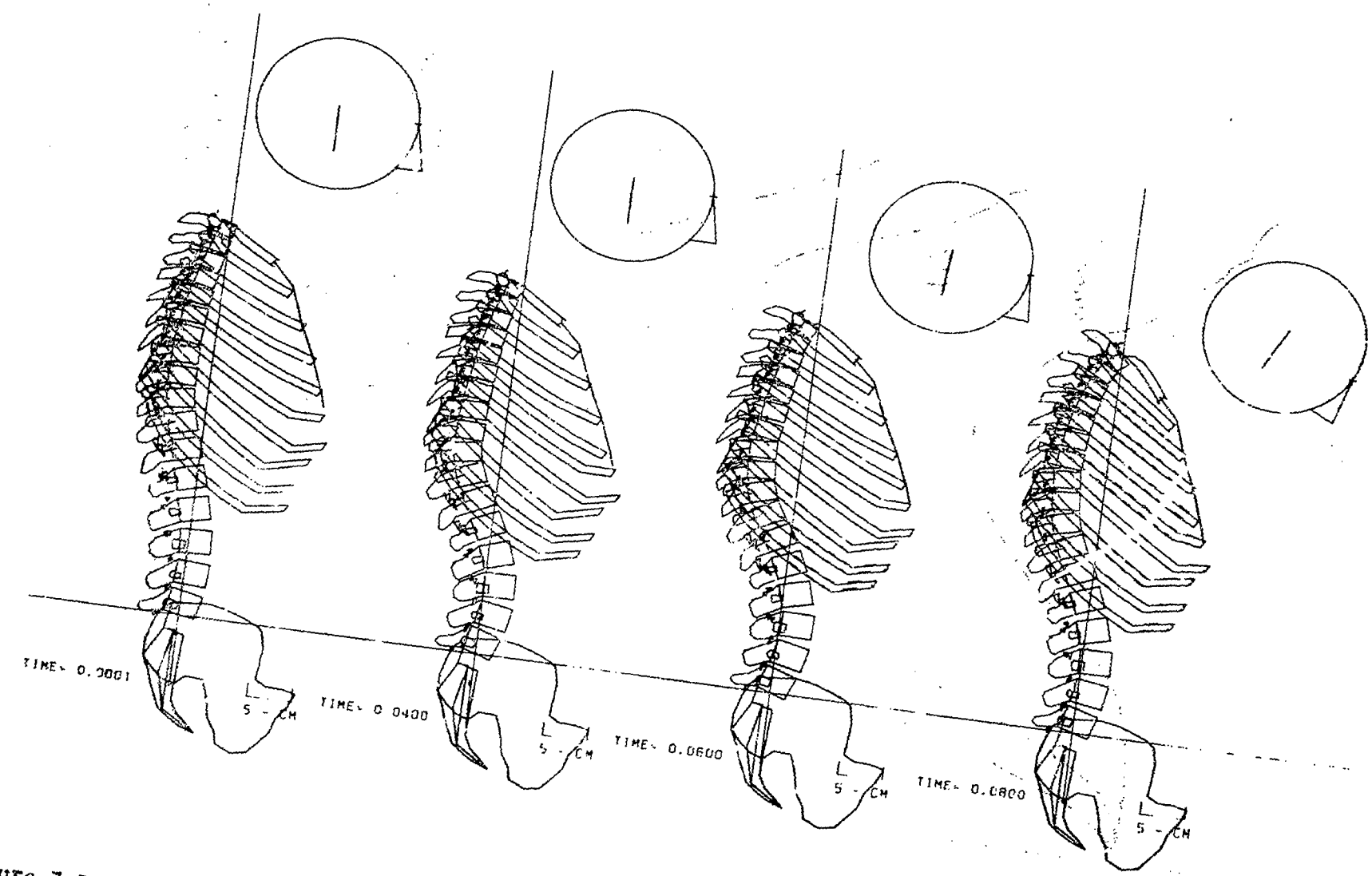

Figure 7.7. Configurations at 0, 40, 60 and 80 msec for ejection of CSM with head/helemt mass center moved 4" forward.

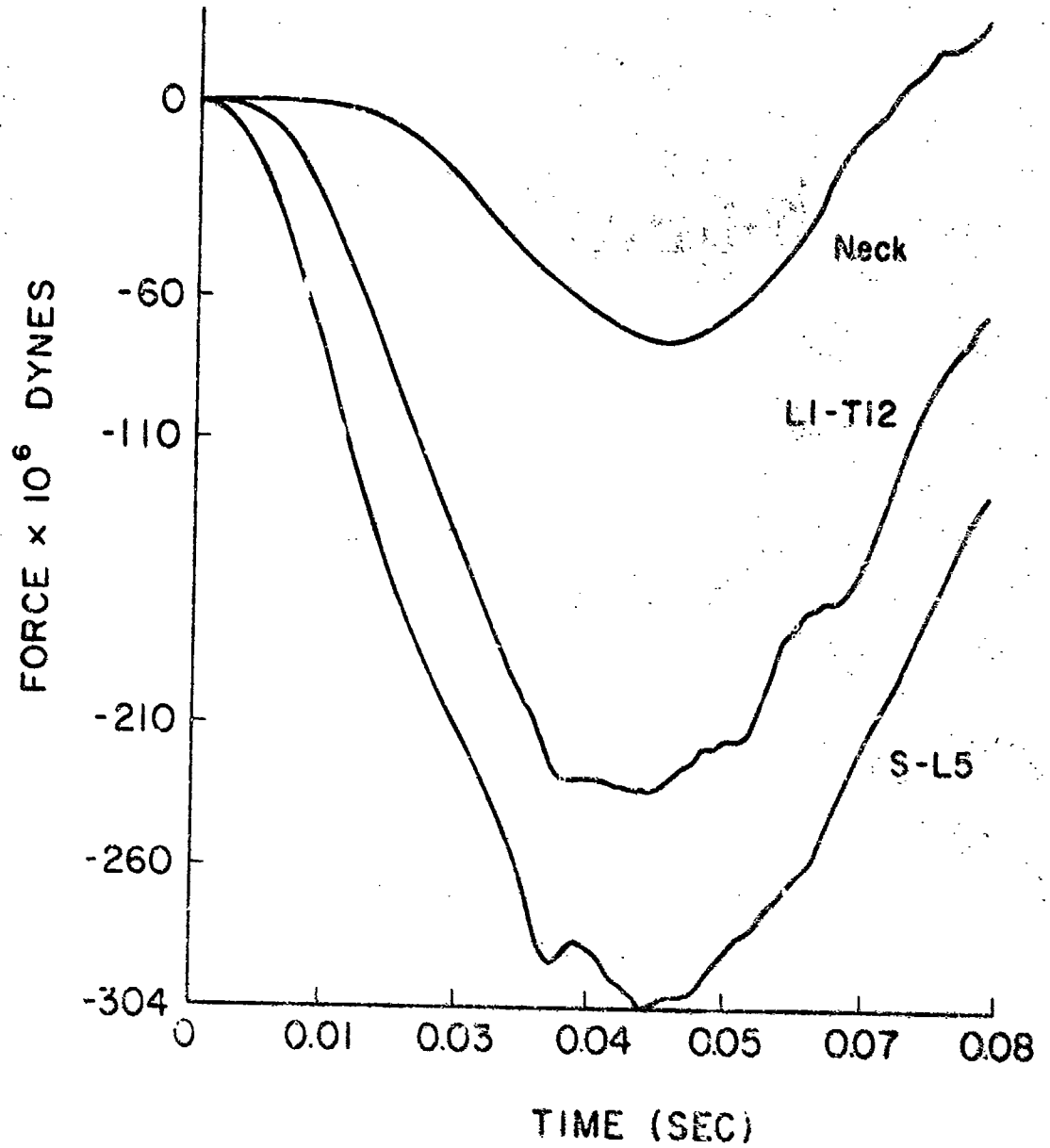

Figure 7.8. Axial force response in the S-L5 and L1-T12 discs and the neck for ejection of the CSM with head/helmet mass center moved 4" forward.

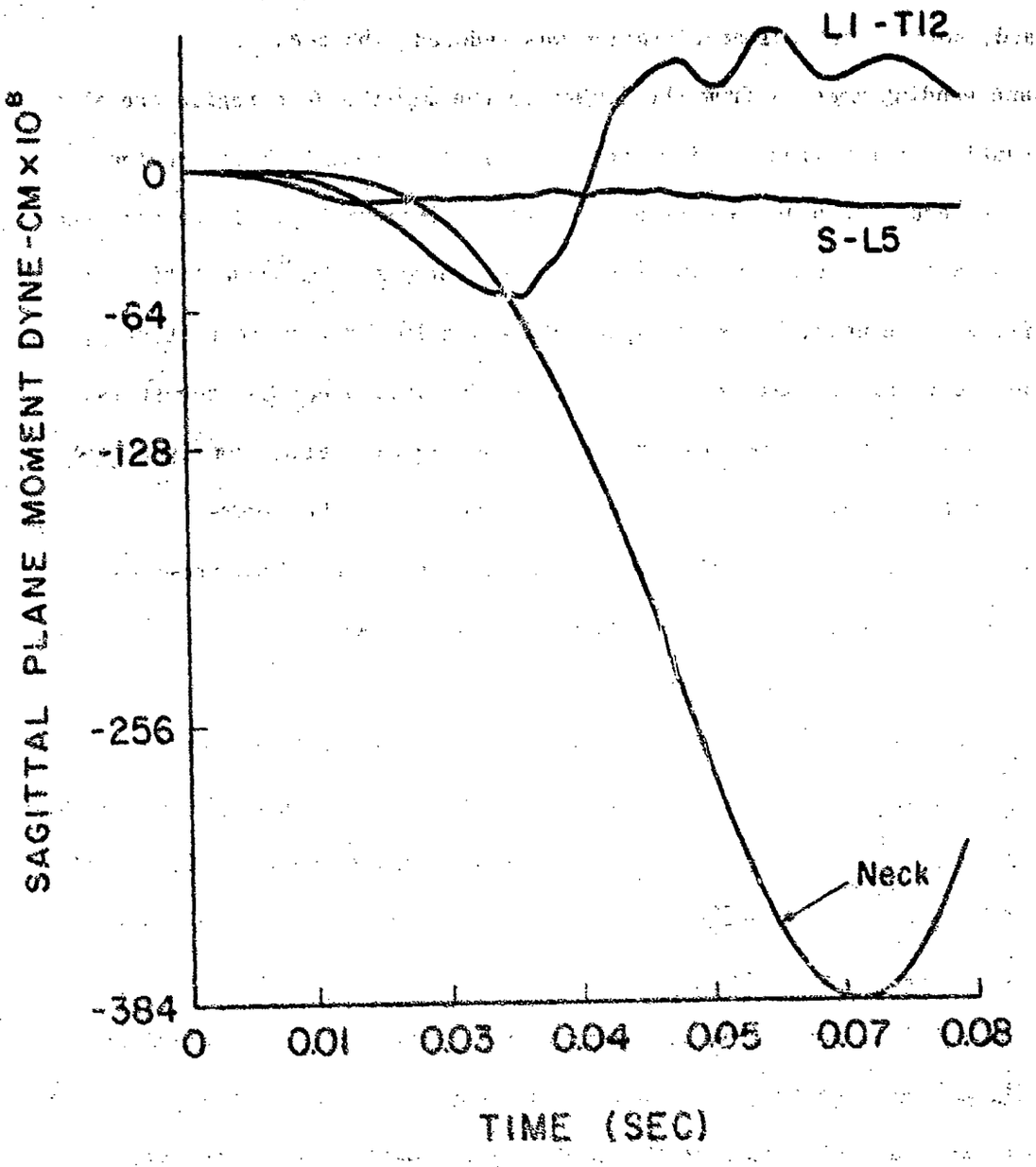

Figure 7.9. Moment response in the S-L5 and L1-T12 discs and the neck for ejection of the GAM with head/helmet mass center moved 4" forward.

selected axial force and sagittal plane bending moment time histories. The peak axial compressive forces were very similar to those observed in the previous simulation with this model. There was some decrease at T1 because the head moved forward, so its vertical acceleration was reduced. The peak sagittal plane bending moments from the lumbar to the mid-thoracic region are also not significantly altered from previous results. In the upper thoracic region (T4-T1) and the neck, the peak moments are increased considerably. If we take the axial compressive force and moment in T1 to be the averages of the quantities in the T1-T2 disc and the neck, 8.4×10^7 dynes and 2.5×10^8 dyne-cm respectively, then the injury criteria of Belytschko, et al., (1976) indicates that the stress level in T1 is well above the failure criterion. The 80 msec pilot configuration, Fig. 7.7, demonstrates that the deformation of the neck is quite severe.

The peak visceral pressures in Table 7.5 are little changed from previous simulations. This is expected since the axial forces and moments in the lumbar and lower thoracic region also showed little change.

From the ejection simulation presented in this and the previous section, we may conclude that (1) the increase of the curvature of the spine is reduced considerably by the introduction of a restraint system (i.e. harness and seatbelt), (2) including a detailed representation of the rib cage and viscera also increases the stability of the spine; (3) the internal forces, particularly the sagittal plane bending moments, are effected by variations in inertial reel height; (4) a variation in initial head/helmet mass location can lead to substantial increases in sagittal plane bending moments and forward motion of the head; (5) the axial forces predicted by the model seem quite independent of these parameters.

VII.4 Comparison of Ejection Response of SSM, ILSV and CSM

The SSM was developed to reduce the computational effort of various simulations by replacing various groups of elements from the more complex models by single elements. We have already shown the similarity of the SSM and ILSV impedance curves. In this Section, we will compare the SSM response in ejection to the ILSV and CSM models.

An ejection simulation was run with the SSM using the standard $+10G_z$ acceleration profile described in Section VII.1. A restraint system was included consisting of a seatbelt, modeled as a tension only spring between the seatback and the pelvis, and a harness, modeled as a tension only spring between the seatback and T1. The reel height was the initial height of T1. The ejection environment of the SSM was therefore identical to the CSM ejection simulation discussed in Section VII.3.1. A similar ejection simulation was run with the ILSV. The initial SSM and ILSV configurations are the normal configurations shown in Figures 2.7 and 2.4 respectively.

The damping parameters of the SSM and ILSV were adjusted so that the lowest spine axial and bending modes and the lowest visceral mode are damped by 10%. This is consistent with the CSM for which the lowest spine axial mode and lowest visceral mode are also damped by 10%. These damping levels are lower than those determined in the impedance study. Justification for lowering the SSM and ILSV damping values is based on the work of Vykukal (1968). Vykukal exposed four subjects in a semi-supine position to a vertical acceleration of ± 0.4G in a frequency range from 2½ to 20 Hz combined with linear accelerations of 1, 2½ and 4G. He reported that the impedances of the subjects indicated a decrease in damping with an increase in sustained acceleration.

Tables 7.6 and 7.7 compare the peak internal force responses and visceral pressures of the SSM, ILSV and CSM during the standard ejection environment. The peak axial force in an SSM element is compared with the average of the peak axial

forces in the corresponding discs of the ILSV and CSM. The peak SSM moments are taken from the upper end of the element. For example, the peak moment for element L3-T10 is taken from the T10 end. This is compared to the peak moment at the superior end of the specified disc of the ILSV and CSM. The peak visceral pressures of the SSM visceral elements is computed by dividing the peak internal force of the element by the average cross-sectional area of the element. Hence, this is actually the peak visceral element stress. The corresponding value for the ILSV is the average of the individual peak stresses in the noted ILSV visceral elements.

The peak axial forces, moments and visceral pressures show good overall agreement both in magnitude and distribution. Some discrepancy results from the lumping of the masses in the SSM. Although not tabulated, the peak harness forces show reasonable agreement for the three models.

The peak vertical accelerations at T1 are 17.1G, 20.2G and 18.8G for the SSM, ILSV and CSM respectively (G = acceleration due to gravity). The peak vertical accelerations at the head are 20.0G, 24.0G and 19.7G for the SSM, ILSV and CSM respectively. The agreement is quite good.

Although not shown, the 40, 60 and 80 msec pilot configurations for the three models are very similar.

The results presented in this section demonstrate that the SSM, ILSV and CSM overall ejection simulation responses are in good agreement. Hence, the SSM may replace either the ILSV or the CSM for ejection studies in which the general aspects of the response are of interest rather than the detailed response at each vertebral level. The SSM would be very useful for design studies where short running time is a premium, such as in an interactive mode.

Table 7.6. Comparison of Peak Internal Force Response for Similar Ejection Simulations of SSM, ILSV and CSM.

SSM Element	ILSV,CSM Discs	Peak Axial Force dynes x 10^8			Peak Sagittal Moment dyne-cm x 10^7		
		SSM	ILSV[1]	CSM[1]	SSM	ILSV	CSM
S1-L3	L5-L3	-3.02	-2.57	-3.08	10.92	9.22[2]	10.69[2]
L3-T10	L2-T10	-2.73	-2.60	-2.60	-8.49	-8.72[3]	-9.93[3]
T10-T1	T9-T1	-1.97	-1.39	-1.65	-3.12	-3.69[4]	1.21[4]
Neck	Neck	-1.11	-1.33	-1.12	7.56	6.63	4.89

[1] ILSV and CSM peak axial forces are averages for the given intervertebral discs

[2],[3], [4] Peak moments in the L3-L4, T10-T11 and T1-T2 discs respectively

Table 7.7 Comparison of Peak Visceral Pressures for Similar Ejection Simulations of SSM, ILSV and CSM.

SSM Visceral Element	ILSV Visceral Element	CSM Hydrodynamic Element	Peak Visceral Pressure dyne/cm^2 x 10^5 SSM(1)	ILSV(1)	CSM
Pelvis-L5	Pelvis-S1, S1-L5		8.21	7.25	
		Lower			4.96
L5-L3	L5-L4, L4-L3		3.95	3.21	
		Middle			4.06
L3-L1	L3-L2, L2-L1		2.96	1.57	
		Upper			2.51
L1-T10	L1-T12, T12-T11, T11-T10		0.91	0.65	
	Average		4.01	3.17	3.84

(1) The SSM and ILSV pressures are actually the average peak stresses in the given elements

APPENDIX A

IMPEDANCE PROGRAM OPTION

This Appendix briefly describes the programming procedures for obtaining the impedance curves of the spine models.

AI.1. Description of Procedure

The impedance curves of the spine models are of interest in the frequency range of approximately the 0-30 Hz. This is well below the numerical stability limit for explicit time integration of the spine models. For this reason and the fact that impedance is obtained from a linearized analysis (thus requiring only one assembly of the stiffness matrix), the implicit code is used. The procedure for obtaining an impedance curve is outlined as follows:

(1) in subroutine FREEFD, a unit step velocity is prescribed at either the pelvic or seat primary node global z translation;

(2) in subroutine SOLVI, this degree of freedom, called NSEAT, must be identified. A double precision array, FSEAT(1025) is included to provide storage for the reaction force time history. At the end of each solution step, the statement

```
FSEAT (NSTEP) = -FINT (NSEAT)
```

stores the negative of the internal axial force acting on the pelvis or buttocks in FSEAT. The acceleration of the driven mass is zero except at time zero (the velocity is a step function), so FSEAT represents the reaction force;

(3) after the last solution step in SOLVI, the FFT (Fast Fourier Transform) subroutine is called by the statement

```
CALL FFT(FSEAT,DELT,MXSTEP)
```

where DELT is the solution time step, and MXSTEP is the number of solution steps;

(4) subroutine FFT computes the DFT (Discrete Fourier Transform) of FSEAT. The modulus of impedance, which is defined as $Z(\omega) = \left|\frac{F(\omega)}{v(\omega)}\right|$, is then determined by

dividing the magnitude of the DFT of FSEAT by the magnitude of the DFT of the unit step velocity at each frequency step. If the unit step velocity is applied directly to a mass, (e.g. at the pelvis) the scalar PMASS must be set equal to the translational mass. The impedance of the mass is then also computed. If the unit step velocity is not applied directly to a mass (e.g. at the seat), PMASS must be set equal to zero. The FFT impedance output is in the form of F(K), Z(K), ZTOT and ZMASS at frequency step K, where

F(K) = circular frequency at frequency step K,

Z(K) = modulus of impedance (not including the impedance of the driven mass) at frequency step K,

ZTOT = total modulus of impedance at frequency step K = Z(K) + ZMASS,

ZMASS = modulus of impedance of the driven mass at frequency step K.

AI.2. Data Notes

A method for computing the approximate duration time, ΔT, required for the transient response to approach zero is described in Chapter IV. Once ΔT is determined, the accuracy of the FFT depends on the number of solution steps, MXSTEP. It was found that MXSTEP = 256 is a satisfactory number of solution steps for obtaining impedances of the spine models in the 0-30 Hz region. Hence, the solution time step, DELT, is given by $\Delta T/256$. The upper bound to MXSTEP is 1025 since all arrays are dimensioned at this value. If MXSTEP $\neq 2^N$, $N \leq 10$, a cubic interpolation routine, subroutine INTRP, realigns the discrete points in the time history so that it is defined by 2^N points, $N \leq 10$. If possible, however, it is recommended that MXSTEP = 2^N since this will eliminate the interpolations.

For the impedance runs as well as for other runs in which damping greater than approximately 10% of critical is employed, it is recommended that the stiffness proportional damping is used rather than the fraction of critical damping because this damping behaves better for larger damping values.

REFERENCES

Andriacchi, T., Schultz, A., Belytschko, T. and Galante, J. O., (1974), "A Model for Studies of Mechanical Interactions Between the Human Spine and Rib Cage," J. Biomechanics 7, 497-507.

Belytschko, T., Kulak, R. F., Schultz, A. B., and Galante, J. O., (1974), "Finite Element Stress Analysis of an Intervertebral Disc," J. Biomechanics 7, 277-285.

Belytschko, T., Schwer, L. and Schultz, A. B., (1976), "A Model for Analytic Investigation of Three-Dimensional Head-Spine Dynamics," University of Illinois at Chicago, Report to Aerospace Medical Research Laboratory, Wright-Patterson Air Force Base, AMRL-TR-76-10.

Bosee, R. A. and Payne, C. F., (1961), "Theory on the Mechanisms of Vertebral Injuries Sustained on Ejections from Aircraft", presented at the Meeting of the Aerospace Medical Panel of the Advisory Group for Aeronautical Research and Development, NATO.

Brigham, E. O., (1974), "The Fast Fourier Transform," Prentice-Hall.

Brown, T., Hanson, R. J. and Yorra, A. J., (1957), "Some Mechanical Tests on the Lumbosacral Spine with Particular Reference to the Intervertebral Discs," J. of Bone and Joint Surgery, 39 A, No. 5.

Coermann, R. R., (1959), "The Mechanical Impedance of the Human Body in the Sitting and Standing Position and its Significance for the Subjective Tolerance to Vibrations", presented at the Third Biophysical Society Meeting, Pittsburgh, Pennsylvania.

Coermann, R. R., Ziegenruecker, G. H., A. L. and von Gierka, H. E., (1960), "The Passive Dynamic Mechanical Properties of the Human Thorax-Abdomen System and of the Whole Body System". Aerospace Magazine.

Crocker, J. F. and Higgins, L. S., (1966), "Phase IV - Investigation of Strength of Isolated Vertebrae," Final Technical Report TI 1313-66-4, Technology, Incorporated, Life Sciences Division.

Evans, F. G., (1970), "Mechanical Properties and Histological Structure of Human Cortical Bone," A.S.M.E. Publication 70 - WA/BHF-7.

Eycleshymer, A. C. and Schoemaker, D. M., (1970), "A Cross-Section Anatomy", Meredith Corporation.

Gaertz, A., (1946), "Limits and Special Problems in the Use of Seat Catapults," AAF Aero Medical Center ATI No. 56946.

Holmes, N. A., (1976), "Characteristics of Transient Finite Element Solution".

Kazarian, L., (1976), "Data for Nonhuman Primates", Personal communication.

Kulak, R. F., (1974), "A Study of Intervertebral Disc Mechanics by the Finite Element Method," Ph.D. Thesis, University of Illinois at Chicago Circle.

Lanier, R., (1939), "The Presacral Vertebrae of American White and Negro Males," Amer. J. Physical Anthro. XXV, 341-420.

Latham, F., (1957), "A Study in Body Ballistics: Seat Ejection", Proceedings of the Royal Soceity 147, Series B, 121.

Lathi, B. P., (1974), "Signals, Systems, and Controls", Intext.

Li, T. F., Advani, S. H. and Lee, Y. C., (1970), "The Effect of Initial Curvature on the Dynamic Response of the Spine to Axial Accelerations", Symposium on Biomechanical Models and Their Applications, Aerospace Medical Research Lab., Wright-Patterson Air Force Base.

Liu, Y. K. and Wickstrom, J. K., (1973), "Estimation of the Inertial Property Distribution of the Human Torso from Segmented Cadaveric Data," Perspectives in Biomedical Eng.

Lucas, D. and Bresler, B., (1961), "Stability of the Ligamentous Spine", Biomechanics Laboratory Report 40, University of California at San Francisco.

McElhaney, J. H., (1966), "Dynamic Response of Bone and Muscle Tissue," J. Appl. Physiol., 21, 1231-1236.

Mohr, G. C., Brinkley, J. W., Kazarian, L. E. and Millard, W. W., (1969), "Variations of Spinal Alignment in Egress Systems and Their Effect", Aerospace Medicine, 40, 9.

Orne, D. and Liu, Y. K. (1970), "A Mathematical Model of Spinal Response to Impact", J. of Biomechanics, 4, 49-71.

Pansky, B. and House, E. L. (1964), "Review of Gross Anatomy: A Dynamic Approach," Macmillan.

Payne, P. R. and Band, E. G. U., (1969), "A Four Degree-of-Freedom Lumped Parameter Model of the Seated Human Body", Wyle Laboratories, Payne Division Working Paper No. 59101-6.

Payne, P. R., (1972), "Some Aspects of Biodynamic Modeling for Aircraft Escape Systems," Proc. Symposium on Biodynamic Models and App., Wright-Patterson Air Force Base, Ohio.

Perey, O., "Fracture of the Vertebral End-Plate in the Lumbar Spine: An Experimental Biomechanical Investigation," ACTA Orthopaedica Scand., Supp. 25 (1957).

Prasad, P. and King, A. I., (1974), "An Experimentally Validated Dynamic Model of the Spine," J. Appl. Mech., 546-550.

Reynolds, H. M., (1974), "Measurement of the Inertial Properties of the Segmented Savannah Baboon", Ph.D., Thesis, Southern Methodist University.

Rockoff, S. D., Sweet, E., and Bleustein, J., (1969), "The Relative Contribution of Trabecular and Cortical Bone to the Strength of Human Lumbar Vertebrae", Calc. Tiss., Res 3, 163-175.

Rohles, Jr., F. H., and Finch, J., (1961), "Gross-Body Measurements of the Young Chimpanzee," AMRL Technical Report MDC-TDR-61-36, Holloman Air Force Base, New Mexico.

Schultz, A., Benson, D., and Hirsch, C., (1974), "Force-Deformation Properties of Human Ribs," J. of Biomechanics 7, 303-309.

Schultz, A., Belytschko, T. B., Andriacchi, T. P. and Galante, J. O., (1973), "Analog Studies of Forces in the Human Spine: Mechanical Properties and Motion Segment Behavior," J. Biomechanics 6, 373-383.

Schwer, L. E., (1976), "A Three-Dimensional Large Displacement Transient Analysis of the Human Spine and Torso", Ph.D. Thesis, University of Illinois at Chicago Circle.

Torvik, P. J., (1970), "An Analysis of Pressure Waves Generated in Seated Spinal Impact," Symposium on Biodynamic Models and Their Application, Dayton, Ohio.

Vernon, J. B., (1967), "Linear Vibration Theory", John Wiley and Sons.

Vierck, R. K., (1967), "Vibration Analysis", International Textbook Company.

Vogt, H. L., (1968), Coermann, R. R., and Fust, H. D., (1968), "Mechanical Impedance of the Sitting Human under Sustained Acceleration", Aerospace Medicine, Vol. 39.

Vykukal, H. C., (1968), "Dynamic Response of the Human Body when Combined with Various Magnitudes of Linear Acceleration", Aerospace Medicine, 39.

Weis, E. B., and Mohr, G. C., "Cineradiographic Analysis of Human Visceral Response to Short Duraction Impact", Aerospace Medicine 38, 10

Woods, A. G., (1967), "Human Response to Low Frequency Sinusoidal and Random Vibration," Aircraft Engineering, 39.

Yamada, H., (1970), "Strength of Biological Materials," Baltimore: The Williams and Wilkins Co.

*U.S. Government Printing Office: 1978 — 657-002/221